学位論文

Formation of Phthalocyanine Ultrathin Layers on Inorganic Solids via Wet Processes

（湿式プロセスによる無機固体上へのフタロシアニン超薄層の形成）

平成２７年１２月博士（理学）申請

東京大学大学院理学系研究科

化学専攻

小島 峻吾

Formation of Phthalocyanine Ultrathin Layers on Inorganic Solids via Wet Processes

by

Shungo Kojima

Department of Chemistry

Graduate School of Science

The University of Tokyo

December, 2015

Abstract

Organic-inorganic interface has attracted much attention because the interface plays important roles in recent functional organic semiconductor devices. So far, simple oxides such as ZnO and TiO_2 have often been adopted to investigate the nature of the interface. On the other hand, multiple oxides such as perovskite type ones possess various fascinating functionalities such as high temperature superconductivity and half metallicity, which are expected to be utilized in future organic semiconductor devices.

A simple method for fabricating organic semiconductor/perovskite oxide junctions is deposition of organic molecules onto the oxide surface. Here, how the initial molecular layer is formed on the oxide as a consequence of molecule-oxide interaction is of significant importance, because it often determine the structure and orientation of the organic layer as a whole which finally governs the performance of devices. Vapor deposition techniques such as vacuum deposition and molecular beam epitaxy have been used to study the organic ultrathin layers deposited on oxide substrates, however, they have difficulty in observing weak interaction at the interface due to the kinetic deposition process.

In my research, ultrathin organic layers were formed by two types of wet processes: Langmuir-Blodgett (LB) method and so-called immersion method. In the former method, two octaoctyloxy metallophthalocyanines *M*OOPcs with flexible substituents and different central metals (*M* = Cu, Zn) were compared in order to understand the

molecular orientation and Langmuir monolayer formation on hydrophilic substrates. In the latter method, ultrathin layers of the phthalocyanine FePcCl were prepared on single crystals of perovskite oxides, $LaAlO_3(100)$ (LAO) and $SrTiO_3(100)$ (STO) that have different surface termination, LaO and TiO_2 layers, respectively.

Surface pressure-area isotherms (π-*A* curves) of *M*OOPcs in the LB method showed that the surface pressure gradually increased reflecting their flexible octyloxy chains. The limiting areas were 1.04 nm^2 and 1.33 nm^2 for CuOOPc and ZnOOPc, respectively. These molecules indicated different isotherms at lower surface pressure due to different orientation of the monolayers, in spite of almost the same molecular structure. Such difference in isotherms resulted in different surface morphology observed by AFM, as follows. The ZnOOPc film showed an assembly of islands with partial coverage. The height of the ZnOOPc islands was about 1.6 nm, which is much smaller than the lateral size of ZnOOPc molecule with long octyloxy chains. Hence, the islands were the assembly of the monolayers whose molecular plane was inclined towards the surface, due to hydrophilic nature of the central metal Zn. CuOOPc monolayer showed a flat and homogeneous surface, and its molecular plane was expected to be less inclined. The effect of different central metal was also observed for films deposited at a higher surface pressure.

From the time evolution measurements of water trough area after the application of surface pressure, it was found that ZnOOPc only showed rapid decrease in trough area at 20 mN/m. This result indicated that the high surface pressure induced further compression to maintain the surface pressure. Accordingly, ZnOOPc became densely packed at the high surface pressure probably because of intermolecular attractive interaction dominating over the hydrophilic interaction as described above. The UV-vis absorption spectra observed this compression and suggested more effective transfer of

ZnOOPc Langmuir monolayers than those of CuOOPc. X-ray reflection (XRR) measurements revealed a smaller thickness of ZnOOPc monolayer transferred at 3 mN/m, supporting the molecular orientation in LB monolayers proposed above.

In immersion method, AFM images of FePcCl ultrathin layers on LAO and STO substrates after immersion in 0.3 mM pyridine solutions of FePcCl and drying showed significantly different surface coverage between LAO and STO, indicating the preferential molecular adsorption on LAO. Such difference in adsorption amount was also confirmed by X-ray photoemission spectroscopy (XPS). The surface termination of each substrate is known to be TiO_2 for STO(100) and LaO for LAO(100). Thus, it is possible that the surface termination affected the molecular adsorption. Density functional theory (DFT) calculation was performed to evaluate and compute adsorption energy of the molecule on each surface. As a result, the adsorption energy on LaO of LAO(100) was found to be larger than that on TiO_2 of STO(100) by about 3 eV, being consistent with the experimental observations. These results indicate that surface termination layer of perovskite oxide influences the adsorption behavior of the phthalocyanine molecules. For estimation of molecular orientation, linear dichroic (LD) ratio, which reflects the orientation of transition dipole moment, was measured to deduce the average angle of phthalocyanine plane normal with respect to substrate normal. From visible absorption spectroscopy for FePcCl on STO(100) using polarized light, the LD ratio as a function of incident light angle was evaluated. By comparing the experimental spectra with the theoretical curves at different orientation angles, the orientation angle was deduced to be 39°. This indicates that the molecular plane was not in perfectly horizontal geometry, but was inclined towards the surface. Moreover, crystal truncation rod (CTR) measurements, being a surface analysis method to observe scattered X-ray, was also conducted. By analyzing the experimental scattering intensity spectra assuming surface models, the orientation of adsorbed molecules on LAO substrate was estimated, suggesting close

planar geometry with respect to the substrate surface.

Acknowledgement

First of all, I would like to express my deepest gratitude to my supervisor Prof. Tetsuya Hasegawa for giving me a great opportunity to challenge a doctoral corse research in this laboratory. I have been pleased to be a member of the laboratory and to attack this project. I sincerely appreciate his precise advice, strickt discussion, and heartful encouragement. They have been always helpful and essential for me to overcome problems in my work.

I am also deeply grateful to Prof. Tomoteru Fukumura for his generous supports and fruitful advice to my whole research. His broad and deep knowledge have been always impressing me and quite useful at any stage of my research such as startup the theme, exploration of experimental details and preparation of manuscripts. Without his guidance and help, writing this dissertation would not have been possible.

I owe a very important debt of gratitude to Dr. Hideyuki Kamisaka for computational study. His beneficial training allowed me to access to computation, and he offered me a great help to discuss and understand calculation results which are vital parts in my research.

I am indebted to Prof. Yasushi Hirose, Dr. Akira Chikamatsu, and Mr. Shoichiro Nakao for their quite instructive suggestions in meetings and in daily research life. They always assist me to work on issues.

I would like to express my special appreciation to Prof. Yusuke Wakabayashi and Mr. Masato Anada in Osaka University for X-ray CTR scattering measurements and analyses. They provided me a generous introduction of CTR scattering and impressive discussion with them has been pretty helpful for my doctoral corse research.

I woud like to show my gratitude to Dr. Daisuke Ogawa. He taught me LB experiments politely and helped me with various things at startup of the theme.

I would like to appreciate my colleagues spending years in Ph. D course together, Dr. Daichi Oka, Dr. Kei Shigematsu, Dr. Tsuyoshi Suzuki (from Matsuo Laboratory), Dr. Jie Wei, Thantip S. Krasienapibal, Il Jeon, Tsukasa Katayama, and Atsushi Suzuki. Their hard works have been always stimulating me to challenge.

I would also like to appreciate members of Fukumura group and Kamisaka group, Shun Inoue, Ryosuke Sei, Mayuko Oka, Ken'ichi Kaminaga, Kyouhei Yamatake, Yuji Kurauchi, Yutaka Uchida, Dai Kutsuzawa, Takuma Takeda, Shunsuke Shibata, and Naoki Hashimoto for daily work and discusion.

I would like to offer my thanks to all the previous and present Hasegawa Lab. members, Dr. Sohei Okazaki, Dr. Chang Yang, Dr. Youngok Park, Dr. Anri Watanabe, Xi Shen, Kazuki Aizawa, Kenta Shimamoto, Ryosuke Takagi, Kaori Kurita, Tomoya Onozuka, Jumpei Takahashi, Masahito Sano, Vitchaphol Motaneeyachart, Takanori Yamazaki, Keisuke Kawahara, Fahd S. Khan, Ryota Kantake, Keisuke Yamada, Naoki Kashiwa, Toru Koizumi, Michitaka Hukumoto, Satoshi Hujiwara, and Takahiro Maruyama for their cordial supports.

I would like to provide special thanks to secretaries, Ms. Mie Umino, Ms. Miki Komazawa, and Ms. Aya Imoji. I received generous supports for daily life in Hasegawa Laboratory.

Finally, I would like to express sincere gratitude to my family for their over all support (financial support, mental support, and so on) in my whole life.

Contents

Abstract **i**

Acknowledgement **v**

1 General introduction **1**

1.1 Organic-inorganic junctions 1

1.2 Ultrathin layers of organic materials 2

1.2.1 Effects of ultrathin layers 2

1.2.2 Ultrathin layers of macrocyclic molecules 3

1.3 Oxides as inorganic materials 5

1.4 Organic ultrathin layer formation on inorganics 7

1.4.1 Vapor process 7

1.4.2 Wet process 9

1.5 Purpose of this study 17

2 Experimental techniques **19**

2.1 Langmuir-Blodgett (LB) method 19

2.2 Atomic force microscopy (AFM) 22

2.3 Ultraviolet-visible absorption spectroscopy 27

2.4 X-ray reflectivity (XRR) measurement 29

2.5 X-ray photoemission spectroscopy (XPS) 30

2.6 Crystal truncation rod (CTR) analysis 31

2.7 Calculation method 34

3 Langmuir-Blodgett method **37**

3.1 Introduction 37

3.2 Experimental details 38

3.3 Results and discussion 39

3.3.1 π-A isotherms and estimation of orientation 39

3.3.2 Langmuir monolayer transfer onto the substrate 41

3.3.3 AFM and UV-vis absorption measurement 42

3.3.4 X-ray reflectivity measurement 49

3.4 Summary 52

4 Immersion method **55**

4.1 Introduction 55

4.2 Experimental details 57

4.3 Results and discussion 58

4.3.1 Preparation for oxide substrates with atomically flat step-terrace structure 58

4.3.2 Survey of immersion and surface observation 59

4.3.3 Further investigation on immersion method 62

4.3.4 Linear dichroic ratio 67

4.3.5 Crystal truncation rod analysis 73

4.3.6 Calculation of adsorption energy 80

4.4 Summary 85

5 General conclusion **87**

Reference 89

Chapter 1

General introduction

1.1 Organic-inorganic junctions

In past several decades, electronic multilayer devices with laminated structure, such as MOSFET transistors [1], solar cells [2] and LED [3], have given a great impact on our daily lives. In main-stream electronics, they are composed of inorganic materials such as silicon, silicon oxide, and gallium nitride. In addition to the inorganic materials, recently organic materials have attracted much attention as components in electronic devices. For example, organic field-effect transistors (OFET) [4, 5], organic LED (OLED) [6, 7], and organic photovoltaics (OPV) [8–10] are representative devices to which researchers and companies have devoted their resources recently. Such organic devices are considered to be superior in several points such as low cost, flexibility, light weight and easy manufacturing. These features are derived from natures of the organic materials used as the active layers. However,while they are called as "organic" devices, inorganics are also still used as insulating layers, electrodes and so on in those devices; silicon oxide insulator/organic semiconductor channel in OFET, titanium oxide electron collecting layer/organic bulk heterojunction in OPV [11], and, ZnO/conducting polymer for ultraviolet photodetector [12], etc. Thus, it can be said that organic-inorganic junctions or interfaces are playing main rolls and should be paid attention.

At the interfaces, molecular orientation is one of the most important parameters which affect device performances because generally molecules have anisotropic chemical structures, compared with inorganic materials whose components are isotropic particles like atoms and ions. For example, the single crystal of pentacene, which is a basic material to be used in OFET, exhibits highly anisotropic hole mobility. Figure 1.1 shows a photograph of pentacene single crystal used for OFET and a polar plot of hole mobility depending on the hole transport direction, showing high anisotropy [13].

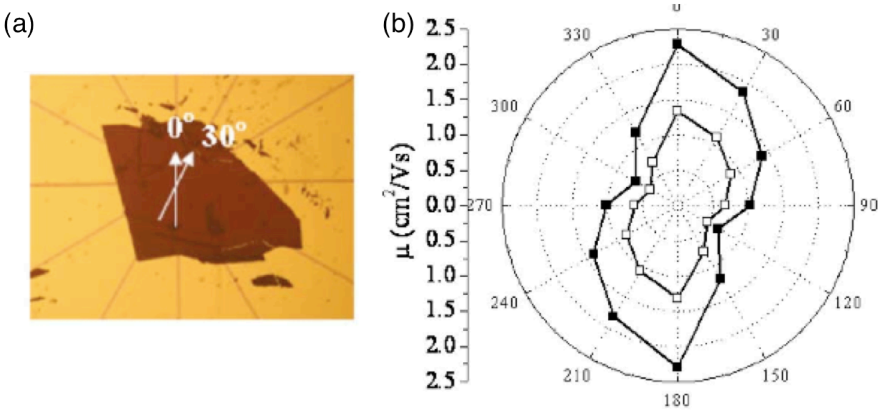

Figure 1.1 (a) Top view of the single crystal pentacene used for FET. The arrows indicate channel directions. (b) Polar plot of the maximum mobility (filled square) and the mobility at gate voltage $V_G = -10$ V (open square) [13]. Reprinted with permission from *Applied Physics Letters* **88**, 252106 (2006). Copyright 2006, AIP Publishing LLC.

In this example, orientation of the pentacene molecules is related to mobility anisotropy within in-plane direction. As in such an in-plane case, we also have to pay attention to out-of-plane molecular orientation with respect to the interfaces, although appropriate orientation depends on the purpose of applications.

1.2 Ultrathin layers of organic materials

1.2.1 Effects of ultrathin layers

Among organic-inorganic collaborations/interfaces, one of the extreme forms is an organic ultrathin layer on the inorganics. Herein, “ultrathin” layer means a few, one, or

less than one monolayer of organic materials. Ultrathin layers have been utilized not only for influence on structural quality of organic-inorganic junctions, but also for interesting functions originating from interactions between ultrathin organics and inorganics.

The former applications are frequently reported in researches aiming at multilayer electronic devices. K. Itaka *et al*. have shown improvement in morphology and crystallinity of C_{60} thin film grown on pentacene monolayer [14]. A change in crystallographic direction of thin films was observed with and without insertion of graphen, which is a nanocarbon material, by S. S. Roy *et al*.(Figure 1.2) [15].

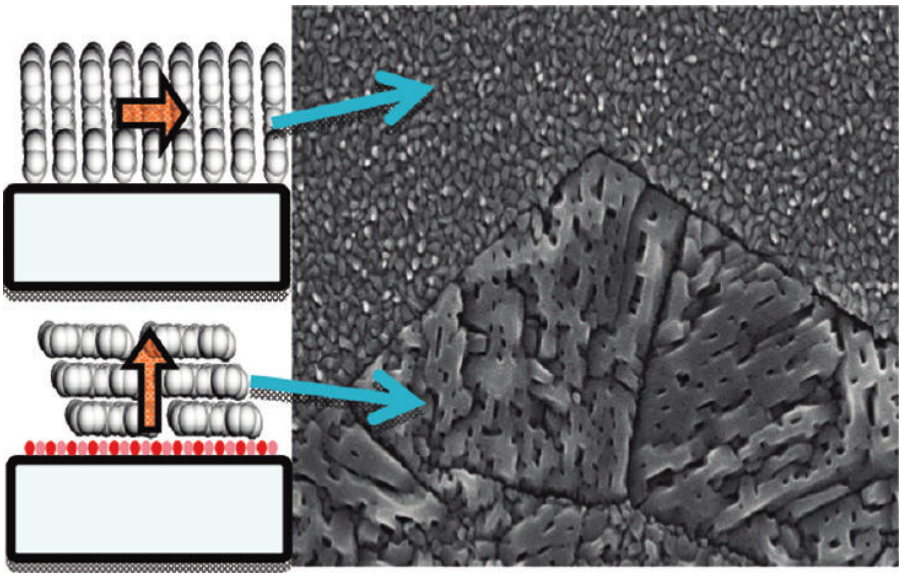

Figure 1.2 Scanning electron micrograph of copper phthalocyanine thin film thermally evaporated on bare glass (upper area) and on graphene modified glass(lower area). Left schematic images indicate orientation of copper phthalocyanine in the film [15]. Reprinted with permission from *The Journal of Physical Chemistry Letters* **3**, 873 (2012). Copyright 2012 American Chemical Society.

1.2.2 Ultrathin layers of macrocyclic molecules

For the latter application mentioned in the previous subsection, macrocyclic molecules such as porphyrins and phthalocyanines (Figure 1.3), which can contain central metal ions, are the representative ones. Porphyrins and phthalocyanines are significant organic functional material classes, well known as organic dyes. They have large π-conjugated

systems, so that they have been researched as representative organic semiconductors, especially for phthalocyanines. The macrocycles have been traditionally used as dye sensitizers [16–18], catalysts in electrochemical reactions [19, 20], and so on.

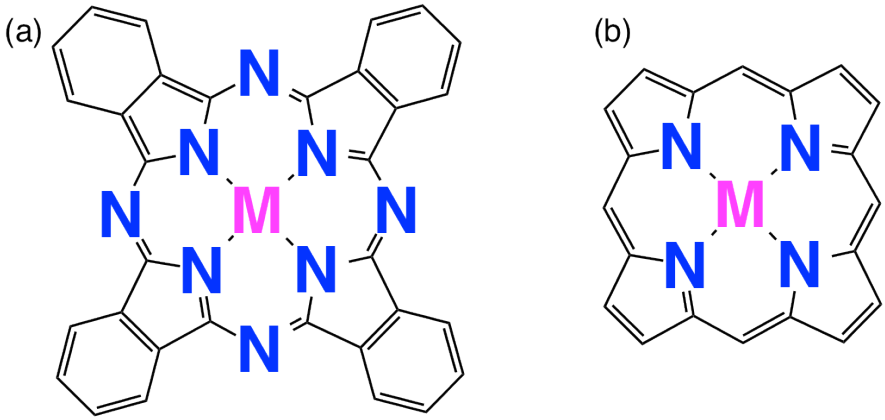

Figure 1.3 Structural formulae of (a) metallophthalocyanine and (b) metalloporphyrin. M in the formulae represent metal ions in the center of the molecules.

Moreover, recently those in a flat geometry with respect to the metal substrates are receiving a lot of attention in terms of a kind of magnetic interaction [21–23]. N. Ballav and co-workers summarized metalloporphyrins and metallophthalocyanines bearing spins on magnetic metals [24]. In such systems, due to the surface-molecule interaction involving spin-polarized electrons in the macrocyclic molecule and surfaces, a kind of hybrid state is generated and ferromagnetic or antiferromagnetic coupling can be induced (Figure 1.4). Furthermore, external chemical stimuli, which are small molecules such as NO and NH_3 being able to coordinate molecular central metals, can engineer the magnetic coupling. In such researches, X-ray magnetic circular dichroism (XMCD) spectroscopy is often utilized to describe the magnetic properties of molecules and substrates because the measurement is suitable to detect the properties elementally specifically. Figure 1.4 (b) shows Mn-specific XMCD spectra of Mn porphyrin on cobalt substrate before and after exposure to NO gas. The sign inversion indicates change of magnetic coupling between Co and Mn in porphyrin from ferromagnetic to antiferro-

magnetic.

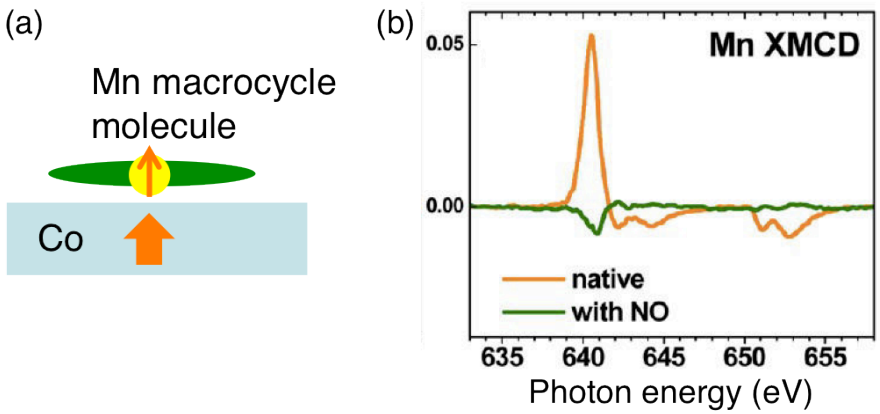

Figure 1.4 (a) Schematic image of a macrocyclic molecule with central Mn ion on a ferromagnetic Co substrate. A thick arrow in Co indicates magnetization direction, which couples with Mn ferromagnetically.(b) Mn specified XMCD spectra of Mn porphyrin on cobalt substrate before and after exposure to NO gas [24]. Reproduced in part from Ref. [25] with permission of The Royal Society of Chemistry.

As mentioned here, the macrocyclic molecules are important materials because they are expected to exhibit interesting properties, collaborating with inorganics at the surfaces. Thus they, in ultrathin layer forms, should be paid more attention and studied furthermore on various inorganics.

1.3 Oxides as inorganic materials

As inorganic materials mentioned in the above sections, metals and oxides are main materials, which collaborated with organic materials.

Metal-organics junctions have been well researched so far, where metals are used as electrodes, magnetic materials, and even magnetic electrodes, because the junctions are basic components in electronics including organic materials. Since injection of electrons or holes from metal electrodes to organic layers, relationship between work function of metals and the energy levels of organics have gained attention [26]. In addition, organic molecules often become targets of scanning tunneling microscope (STM) observation in

atomic or molecular resolution [27–30].

As oxides, simple oxides such as zinc oxide, titanium dioxide and tin dioxide have attracted attention, which have been used with organics, making the best use of their relatively small band gap. For example, the oxides are utilized in dye sensitized solar cells (DSSC) for collecting electrons from excited adsorbed molecules [9,16–18,31] due to their semiconducting nature and suitable energy levels. As seen in this example, generally porous or polycrystalline forms of oxides are mainly adopted for catalysts, multilayer electronic devices, and etc. to exhibit traditional functions such as electron/hole transport layers and insulation as seen in MgO with large band gap. In contrast, single crystalline oxides with defined high-quality surface for junction with organics have not been researched well [12, 32].

In addition to the famous simple oxides, there are of course a variety of other oxides expected for applications such as electronic devices. Doped simple oxides are well known for such applications. Representative materials are indium doped tin oxide (ITO) and niobium doped titanium dioxide (TNO) [33], which are applied to indispensable transparent conductive electrodes for OPVs [8, 10, 11].

Furthermore, multiple oxides, which are containing two or more kinds of metals in their chemical formulae, have been attracting much attention recently. Especially, the perovskite type oxide is one of the most intriguing classes among multiple oxides. Basic perovskite oxides are represented as ABO_3, where B cation is surrounded octahedra of oxide anions (Figure 1.5). As a famous and practical one, $BaTiO_3$ is known as a ferroelectric material having high permittivity [34, 35]. $La_{1-x}Sr_xMnO_3$ (LSMO) is being paid more and more attention to be applied for spintronic devices due to its ferromagnetic half-metal property meaning $\sim$100% spin polarization at the Fermi level [36, 37]. Half metallicity is favorable for efficient spin injection, for example, in organic spin valve

devices, so that LSMO can replace ferromagnetic metals as electrodes [38–40].

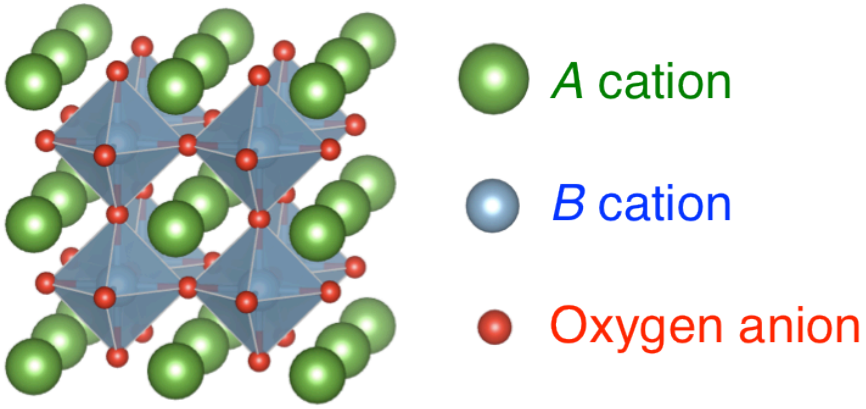

Figure 1.5 Crystal structure of cubic perovskite oxide ABO_3.

Like these perovskite oxides, multiple oxides with exotic properties have become more and more fascinating as new candidates for electronics materials, where they are expected to be used not only with inorganics but also with organics [38–41].

1.4 Organic ultrathin layer formation on inorganics

Methods of organic layer formation are classified into the following two types; vapor process and wet process.

1.4.1 Vapor process

Vapor processes such as thermal vapor deposition and molecular beam epitaxy are basically prevailing methods to prepare organic layers of extended π-conjugated systems like phthalocyanine. By utilizing (ultrahigh) vacuum condition, one can control growth of organics even within monolayer or less level. Additionally, such condition can also provide clean environment and substrate surface as well as high chemical purity [42].

On formation of thin layers, various interactions are concerned. To express such interactions when vapor process is used for deposition onto the solid substrates, sur-

face and interface energies are raised. Generally, the surface energies and/or adsorbate-adsorbate and adsorbate-surface interactions are linked to the several growth modes such as layer plus islands (Stranski-Krastanov), layer-by-layer (Frank-van-der-Merwe), and island growth (Volmer-Weber) [42, 43]. To be strict, some dynamic parameters, which are the flux of adsorbates, the adsorption and desorption probabilities, and diffusion process, should be considered because the growth is actually a non-equilibrium process [43]. Moreover, in addition to the situation of inorganics, there are some important points special to the formation of organic layers, which is derived from individual shape of the molecules regarded as an anisotropic particle. One of the most representative points to think about is *internal degrees of freedom*, in other words, orientation of the adsorbed molecules, as mentioned in Section 1.1. In that context, "edge-on" and "face-on" orientations are typical geometry for π-conjugated molecules. Another example specific to organics is epitaxy, which is frequently used to obtain single crystalline thin films of inorganic materials with particular orientation on oriented substrates. In the molecular case, strain, which is stored in epitaxial growth, can be accommodated more highly despite of great difference in lattice constant between the inorganic substrate and molecules, because softer van der Waals interaction is more important in the system. Thus, so-called "van der Waals epitaxy" and "quasi epitaxy" can be observed [42].

Turning to molecular orientation on inorganic solids, adsorbate-adsorbate and adsorbate-surface interactions are greatly related to the orientation as well as growth modes mentioned above. So, deposition on different types of substrates can influence the coming molecules, resulting in different types of orientation. Deposition of aromatic molecules like phthalocyanines on metal or metal oxide substrates is one of the most typical cases. In the case of metals, the substrates generally show wettability to the molecules, where the molecule-substrate interaction is significantly stronger than the molecule-molecule one. That has been explained by covalent or π-bonding between adsorbate and sub-

strate in literatures [44, 45] about unsaturated hydrocarbons. As a result, π-conjugated molecules are adsorbed in planar geometry. On the other hand, interactions between adsorbates and substrate generally play a less important role on metal oxide substrates. Consequently, the molecules will show an orientation with aromatic plane nearly perpendicular to the substrate surface, where the intermolecular interactions should be maximized. Actually, H. Ohta *et al.* have reported (highly controlled) phthalocyanine deposition on atomically flat ITO surface, where the molecular orientation has taken "edge-on" type (Figure 1.6) [32, 46].

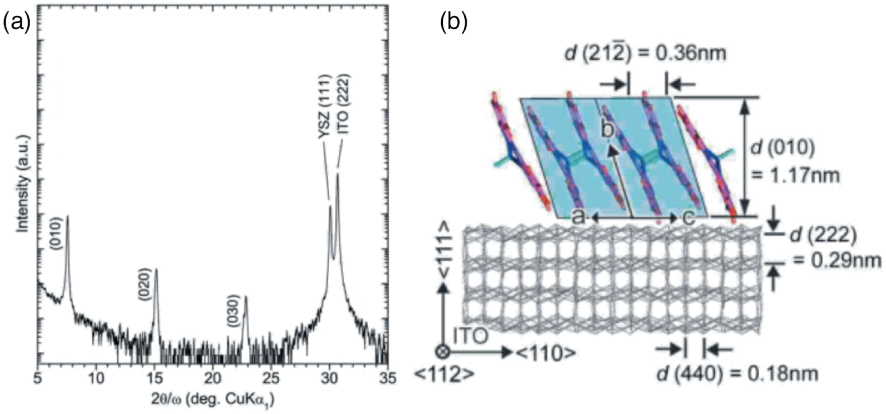

Figure 1.6 (a) An out-of-plane X-ray diffraction pattern of vanadyl phthalocyanine thin film grown on epitaxial ITO thin film. (010), (020), and (030) peaks belong to the phthalocyanine film. (b) A schematic cross-sectional view of vanadyl phthalocyanine grown on ITO(111) surface. Reproduced in part from Ref. [46]. Copyright 2003 John Wiley and Sons.

1.4.2 Wet process

Wet process is another practical method to obtain ultrathin layers. Although vapor process is superior in terms of the cleanness, controllability, and homogeneity, wet process is more feasible and can provide unique structure characterized by molecular orientation, properties and etc. Wet process can deal with molecules which cannot be used in vapor process, such as soluble and large molecular-weight molecules and even polymers.

Langmuir-Blodgett method

Langmuir-Blodgett (LB) method is one of the most famous and examined techniques for making organic layer-by-layer films. Briefly speaking, monolayers of organics are formed by utilizing air-water interface and then transfered onto solid supports repeatedly, resulting in layer-by-layer films. The detailed fabrication process will be introduced in Chapter2.

Generally the condition of spread molecular monolayer on water subphase, named Langmuir monolayer, is checked by surface pressure depending on occupied area per molecule [47]. The surface pressure, π, can be monitored by Wilhelmy plate surface tension device [48]. It is defined as the difference between surface tension of pure water (γ_0) and the molecular monolayer (γ); $\pi = \gamma_0 - \gamma$.

An ideal surface pressure-area (π-A) isotherm is shown in Figure 1.7 [47, 48]. As the area per molecule decreases, the surface pressure π gradually increases, accompanied by phase transitions of the spread two dimensional monolayer, which has some analogy with the three-dimensional matters. When the area is large, floating layer can be seen as two dimensional gaseous phase. As the monolayer is compressed, the phase will show a change to liquid-expanded one which is linked to three dimensional liquid, followed by transition to liquid-condensed one, where structural coherence should exist within short range. Besides, for some materials like stearic acid, the compressed monolayer can reach to the solid phase with a steep increase in the pressure. When the surface pressure increases to a much higher level, the monolayer will collapse. Figure 1.7 is a typical schematic illustration, and an actual experimental π-A curve highly depends on the spread organic materials.

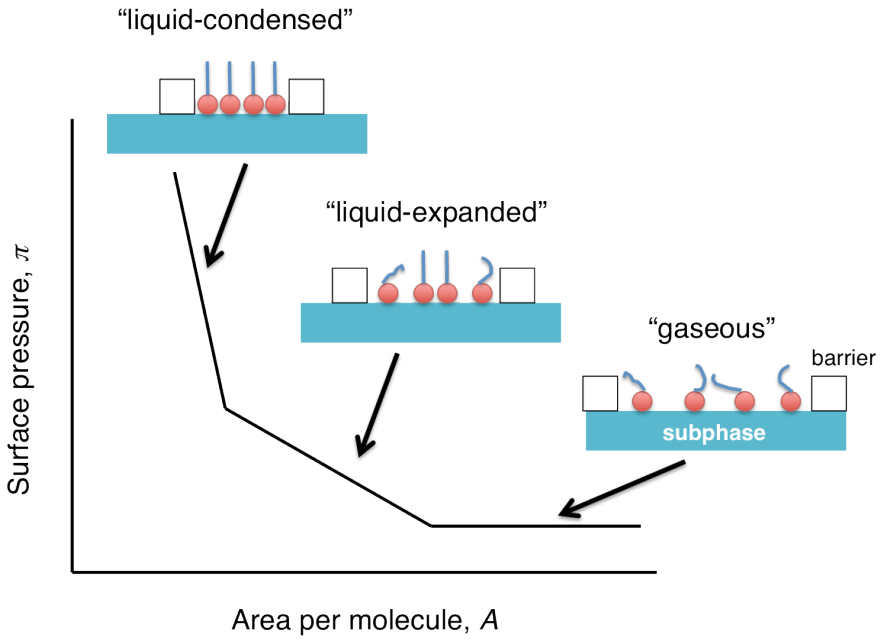

Figure 1.7 An ideal surface pressure-area (π-A) isotherm with phase transitions. Schematic view of molecular state on the subphase for each phase is also shown.

Langmuir monolayer should be transferred onto the solid substrate for a promising application: layer-by-layer multilayer formation can be realized by transfer onto the substrate one by one in LB method. When transfer is carried out only once, organic monolayer, that is, ultrathin layer can be obtained.

In addition to traditional amphiphiles like fatty acids, aromatic molecules, including phthalocyanines, have also been studied for fabrication of LB films, being expected to be used in electronics applications. Thanks to organic synthesis techniques, we can synthesize a variety of aromatic molecules tethering various substituents which influence film structure and properties, where the molecular structure can be even asymmetric [49].

For example, conducting LB films have been reported, where tetrathiafulvalene (TTF) and/or tetracyanoquinodimethane (TCNQ) derivatives, which are electron-donor and electron-acceptor aromatic molecules, respectively, have often been adopted [47]. TTF and TCNQ frameworks are known as components of charge-transfer salts [50],

showing mixed valence which is needed for generating electron or hole carriers in organic conductors. For use in LB method, they are derivatized by some hydrophobic (and hydrophilic) substituents to be amphiphiles so that they can be soluble in spreading volatile solvent and be monolayer on water subphase. To have mixed valence to be conductive, their LB films are oxidized (or reduced) by vapor oxidants such as I_2 or electrochemical reactions [51].

As for phthalocyanines' LB method, it is expected that their substituted macrocyclic structures exhibit cofacial stacking leading to columnar assemblies horizontal to subphase and discotic mesophases(Figure 1.8) [47], so that anisotropic nature in electronic properties should be observed [52]. Anisotropy of phthalocyanine LB films can be confirmed by some optical measurements using polarized light source [53].

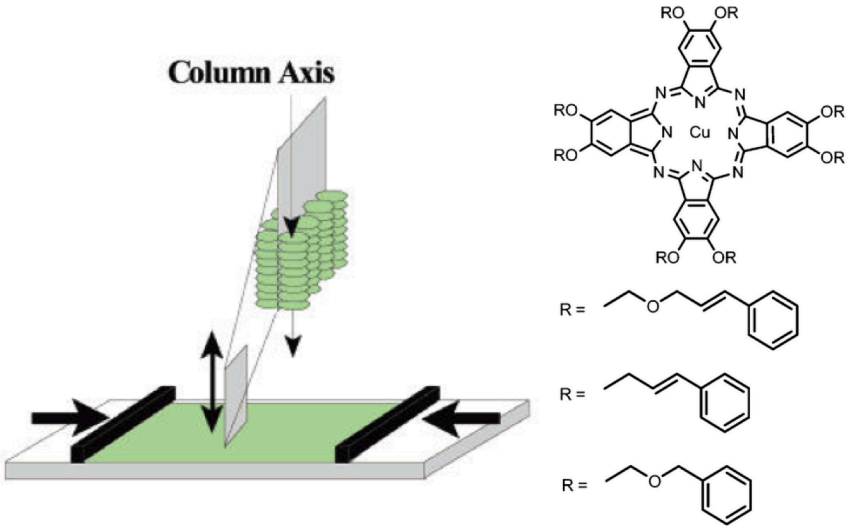

Figure 1.8 Schematic view of columnar assemblies on a solid support by vertical transfer. Phthalocyanine derivatives listed on the right side are some candidates to form columnar assemblies. Adapted with permission from *Langmuir* **13**, 6568 (1997) [54]. Copyright 1997 American Chemical Society. Reprinted with permission from *Chem. Rev.* **104**, 5479 (2004) [47]. Copyright 2004 American Chemical Society.

In addition to the columnar phthalocyanine LB film structure, where the molecular plane is standing to the substrate, achieving other inclined orientation, in an extreme case

it is flat geometry of the plane, is also of great interest. For such a purpose, constructing suitable amphiphilic phthalocyanine by polar (hydrophilic) and/or non-polar (hydrophobic) substituents is needed. Basically, hydrophilic substituents serve as a "weight" which is prone to sink into water subphase, and in contrast hydrophobic substituents such as alkyl chains serve as a "float" on the water surface [55]. For example, macrocyclic molecules with the strong polar substituents either at the center or at the peripheral sites of the ring have been reported. A silanol group at the center of phthalocyanine was used in the former case and tetrapyridinium porphyrazine, which has similar structure to phthalocyanine, with four cation pyridinium moieties was adopted in the latter case, where aliphatic chains are also tethered in both cases [56]. Even if the much less polar substituents such as ether groups at the periphery are incorporated, tilted or flat lying orientation is possible when highly hydrophobic groups, that is, long alkyl chains enough to incline the phthalocyanine ring are adopted (Figure 1.9) [57].

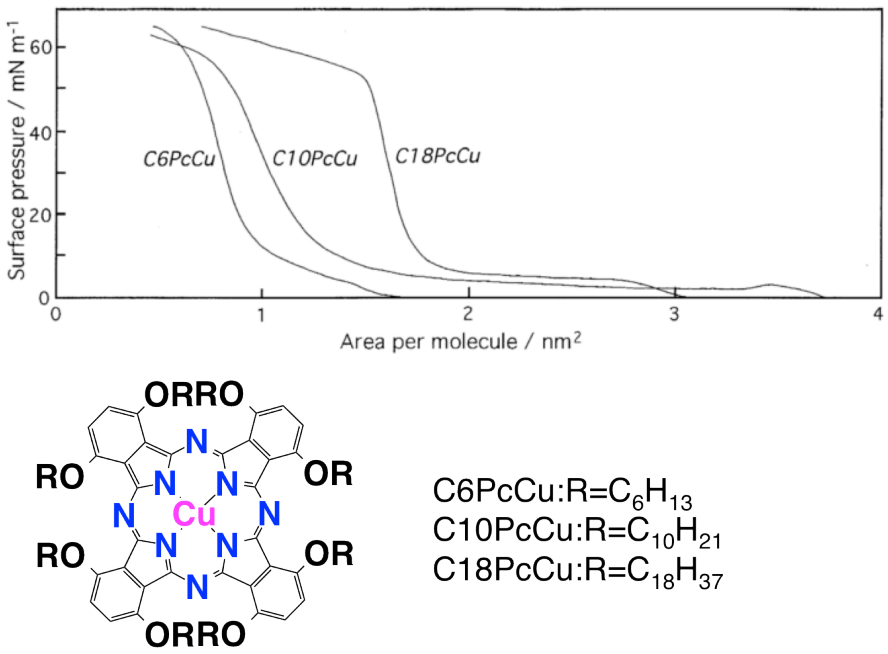

Figure 1.9 π-*A* isotherms of copper phthalocyanines listed on the bottom part. C18PcCu shows a rapid increase in surface pressure at the most larger area. It corresponds to a face-on type orientation of the phthalocyanine ring plane [57]. Reprinted from *Thin Solid Films*, **301**, Y. Matsuzawa, T. Seki, K. Ichimura, "Spontaneous aggregation of octaalkoxyphthalocyanine metal complexes at an airwater interface", 162-168, Copyright 1997, with permission from Elsevier.

In addition to the effect of polar/non-polar substituents on the molecular orientation, central metal dependence of the orientation was also reported in tetraamido phthalocyanines. In the report, authors mentioned that difference in coordination of water molecules lead to the result [58].

Liquid phase adsorption

Other than LB method, adsorption of the molecules on inorganic solids in solution is another candidate to form organic ultrathin layers. Adsorption, either in gas phase or in liquid phase, is typically classified into two types; physisorption and chemisorption [48] [59]. Physisorption is induced by van der Waals interaction consisting of dipole-dipole force, dipole-induced dipole force, and London dispersion force, while chemisorption is based on chemical bond interactions such as covalent bond and electrostatic force.

Comparing adsorption in liquid phase (solid/liquid interphase) with that in vapor phase (solid/gas interface), effects of temperature and pressure on adsorption is smaller in liquid phase, although the adsorption phenomenon is analyzed in the basis of adsorption isotherms (see [48]) used in vapor phase case, which means liquid case can be recognized as analogous phenomena with vapor case. For example, the ratio of solution concentration to the saturated solubility (C/C_0) corresponds to the ratio of adsorbate partial pressure to the total pressure (P/P_0) in vapor phase. However, in contrast to the vapor phase adsorption, competitive adsorption of solvent molecules against adsorbates (solute molecules) should be considered. Besides, solubility depending on solvent is a significant factor having a great effect on adsorption behavior, since C/C_0 changes according to solvent.

One of the most famous organic ultrathin layers by adsorption in liquid phase on inorganic solids is self-assembled monolayers (SAMs) consisting of amphiphilic molecules, which can be mainly classified to chemisorption layers. Formation mechanism of SAMs is derived from active moiety like a thiol group of the SAM molecule anchored to solid surface and intermolecular interaction between aliphatic chain moieties depending on the length. Representative examples are followings; alkanethiols on gold [60, 61], alkyl carboxylic acids or alkyl phosphonic acids on metal oxides such as sapphire [39, 62, 63], and alkyl silanes on SiO_2 surfaces. Such SAMs have been expected for potential applications [64, 65] such as corrosion inhibition and surface patterning. Besides, by adding and varying tail groups, which are the other-side moieties of the aliphatic chains against active groups, it is possible to tailor properties of SAMs surface.Recently, tail groups of SAMs have also been utilized for advanced applications, including organic FETs of organic semiconductors [66, 67] and construction of surface metal-organic-frame (MOF) [68].

Other types of SAMs or SAM like ultrathin layers, where long aliphatic chains are not necessarily included, have also been reported and applied. For example, the report by H. Yip *et al*. noted benzoic acid-based SAMs with several substituents to engineer energy level at interface for an electronics application [69]. Moreover, macrocyclic aromatic molecules like porphyrins and phthalocyanines have been reported to be adhered to inorganic solid surface through peripheral substituents [70, 71]. As for axial anchors through macrocyclic center, thiol groups to the gold substrate [60, 72], central metal-oxygen bond to simple metal oxides [16, 17], and etc. have been used, although porous metal oxides were targets in the latter case.

Adsorption of macrocyclic aromatics on conductive metal surface without chemisorbed anchoring groups by wet process has been a subject of scanning tunneling microscopy (STM). S. Yoshimoto *et al*. have observed self-organization of the molecules in planer geometry at molecular resolution by *in-situ* STM in solution [28, 73].

1.5 Purpose of this study

As mentioned in the previous sections, usage of organic ultrathin layers on the inorganic solids is receiving great attention in the context of recent electronics applications. Among the inorganic materials I mentioned, multiple oxides have been researched and have been expected as candidates of materials used in electronics with interesting functionalities [38, 40, 74–76]. However, utilization of ultrathin organic layers with such oxides has not been focused well so far [39]. Thus, I took an interest in formation of organic ultrathin layers on oxide surface. As organics used in my study, phthalocyanines were paid attention since they are representative as conjugated aromatic molecules, which can exhibit appealing properties such as redox and/or photophysical functions and even chemical stability. In addition, they can store a (transition) metal ion in their center of the molecular structure, so that they sometimes carry magnetic properties utilizing unpaired spins of metals, which would serve in some applications mentioned in the above sections [24].

Looking at formation methods, one may think about vapor processes in vacuum condition at first. Nevertheless, although they are superior in clean environment and substrate surface as well as high chemical purity [42], the orientation of deposited phthalocyanine will take “edge-on” type, which may limit or reduce their inherent ability and applicability to some interesting functions [24, 77]. Accordingly, I took note of wet process, not vapor process, to form phthalocyanine ultrathin layers having orientation other than“edge-on”.

I tried two methods as wet process in my study of Ph.D corse; Langmuir-Blodgett (LB) method and, so called, immersion method. Aiming at ultrathin phthalocyanine layers on multiple oxide substrates in the future, I paid attention especially to the effects

of interactions involved with formation of the layers and tried to estimate molecular orientation on solid supports.

Chapter 2

Experimental techniques

In this chapter, some of the experimental techniques are described, which were used for LB method (Chapter3) and "immersion method" (Chapter4) to obtain ultrathin layers of phthalocyanines and to investigate their structure.

2.1 Langmuir-Blodgett (LB) method [47, 48]

This technique was contrived and developed in an early stage by Irving Langmuir and Katharine Blodgett [78].

As I mentioned in the previous chapter, the layer of molecules spread on water surface is called as a Langmuir monolayer. After it is transfered to a solid substrate, it turns to be called as a Langmuir-Blodgett film.

LB method generally starts with preparing an aqueous subphase in a LB trough. The trough is essentially treated with superhydrophobic coating, which is also applied for movable barrieres to skim the subphase surface.

To obtain a Langmuir monolayer on a water subphase, the target molecule is dissolved in a organic solvent that will normally not react with and dissolve to the subphase. Then the droplets of the solution are placed on the aqueous subphase by a suitable im-

plement such as a microsyringe. The solvent used here has to spread over the surface of the subphase to transport the solute spreading over together, otherwise the droplets remains like "lens" shape on the subphase without spreading. To judge whether the placed solvent droplet will spread over or not, a spread coefficient S has been defined as;

$$\begin{aligned} S &= \gamma_a - \gamma_b - \gamma_{a/b} \\ &= W_a - 2\gamma_a \ , \end{aligned} \tag{2.1}$$

where γ_a and γ_b are surface tentions of the subphase (aqueous phase) and the solvent, respectively, and $\gamma_{a/b}$ is interfacial tension. W_a is work of adheasion, which is defined as;

$$W_a = \gamma_a + \gamma_b - \gamma_{a/b} \ . \tag{2.2}$$

When $S > 0$, the solvent will spread, which is suitable for the molecule of Langmuir layer. In contrast, when $S < 0$, the solvent remains a "lens"-shape droplet. Considering volatility together, chloroform or hexane is frequently used as solvent because the spread solvent has to evaporate to form Langmuir monolayer of the solute. We have to pay attention for the droplets of the solution not to sink into the subphase when they are placed on, especially for chloroform due to its relatively large density.

After solvent evaporation, the molecular monolayer is gradually compressed by the barrier(s) as skimming the surface of the subphase. During the compression, the condition of the Langmuir monolayer is monitored by recording surface pressure (defined as $\pi = \gamma_0 - \gamma$, see Chapter 1.) against area per molecule (surface-pressure (π-A) isotherm). The surface pressure data were collected by Wilhelmy-plate method. In this method, surface tension was estimated from a drawing force mg into the subphase added to a thin plate by meniscus, a filter paper herein, when it touches the surface of the subphase

(Figure 2.1). Surface tension γ is expressed by;

$$\gamma = \frac{mg}{2(L+L_0)} \quad , \tag{2.3}$$

where L and L_0 are noted in Figure 2.1. In my study, a piece of filter paper was hung and tied to a pressure sensor of an equipment.

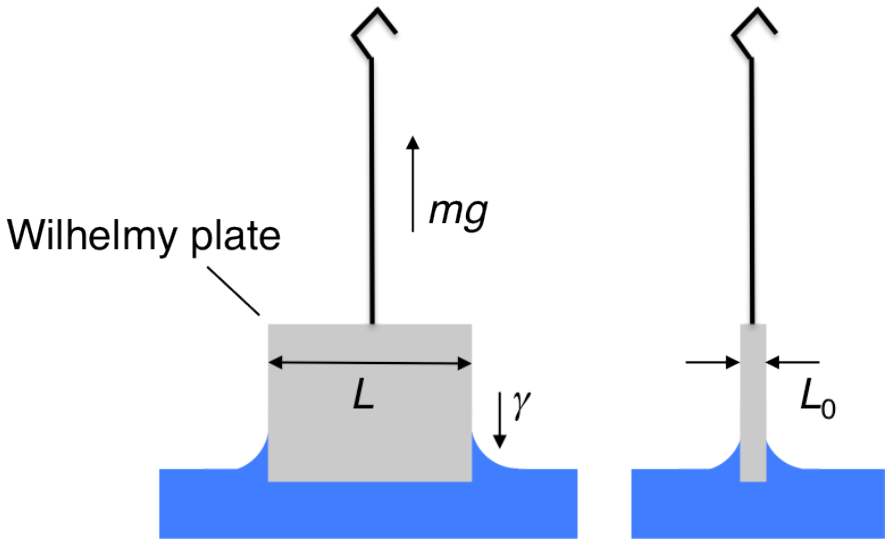

Figure 2.1 Schematic illustration of the surface tension measurement using the Wilhelmy plate.

The evolution of the Langmuir monolayer state according to rising surface pressure is explained in Chapter1. By extrapolating the π-A curve to $\pi = 0$, a limiting area can be found, which represents an actual occupied area per molecule on the subphase.

Then, to fabricate a Langmuir-Blodgett film, it is needed for the Langmuir monolayer to be transferred onto a solid substrate at a certain surface pressure. The transfer is traditionally carried out by vertical lifting of the substrate, meaning that the substrate is withdrawn from or dipped into the subphase with its surface plane perpendicular to the surface of the subphase. The substrate should be made sufficiently hydrophilic or hydrophobic for the better transfer. Actually, the orientation of the molecules such as amphiphiles in the film is changed according to hydrophilicity/hydrophobicity and moving direction of the substrate during transfer.

In contrast to the vertical lifting method (Figure 1.8), horizontal lifting is possible for transfer of the Langmuir monolayer (Figure 2.2). In this case, the hydrophobidized surface of the substrate is suitable because amphiphile molecules at the subphase surface, for example, are turning their hydrophobic groups out to the air phase.

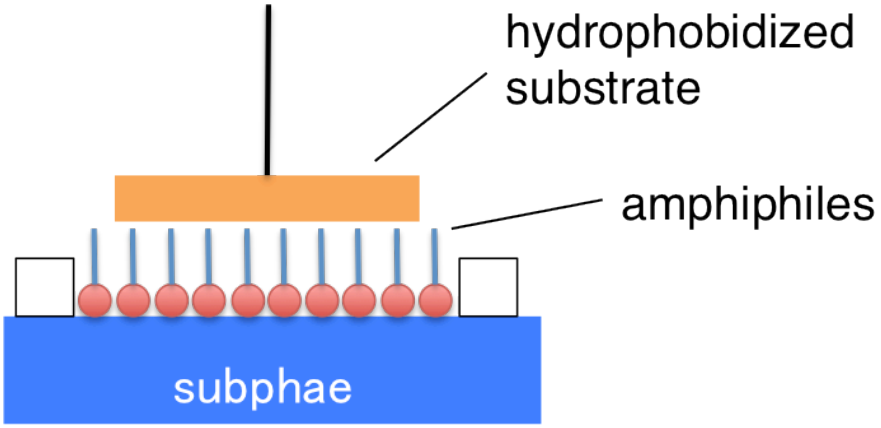

Figure 2.2 Schematic image of the horizontal lifting method for transfer of Langmuir monolayer.

For an indication to evaluate the transfer process, transfer ratio (TR) is often used, which is noted in the following Chapter 3 in detail. When TR is close to 1, the transfer can be regarded as good one.

In this study, LB method was performed using an equipment to fabricate LB films purchased from USI Co. Ltd. with two barriers for compression.

2.2 Atomic force microscopy (AFM) [79–81]

Atomic force microscopy (AFM) has enabled us to observe topography of a sample surface microscopically, even in nanometer resolution. AFM is a member of scanning probe microscopy (SPM) family. Scanning of a probe, which detects atomic force interaction between the probe and the surface, over a certain area of a sample can provide us information about surface topography.

Assuming van der Waals force as attractive force, an interaction between two atoms involving repulsive force can be described as Lennard-Jones type potential;

$$V_{LJ}(r) = U_0 \left[\left(\frac{r_0}{r} \right)^{12} - 2 \left(\frac{r_0}{r} \right)^{6} \right] \quad , \tag{2.4}$$

where the potential takes the minimum $-U_0$ when the interatomic distance becomes $r = r_0$. Then, assuming that the interaction can be integrated linearly, an interaction between an atom and flat surface can be expressed by the sum of the potentials to be;

$$V_{\text{atom-surface}}(z) = \pi \rho_s U_0 \left(\frac{r_0^{12}}{45 z^9} - \frac{r_0^6}{3 z^3} \right) \quad , \tag{2.5}$$

where ρ_s is the number density of the surface atoms and z is the distance from the surface to the atom. A force operating on the atom is described by differential of the potential with respect to z;

$$F_{\text{atom-surface}}(z) = \pi \rho_s U_0 \left(\frac{r_0^{12}}{5 z^{10}} - \frac{r_0^6}{z^4} \right) \quad . \tag{2.6}$$

Eventually, the atomic force is detected with a probe supported by a cantilever with a certain spring constant k. The probe apex consists of not an atom of course, but of several atoms showing small curvature ($\sim$ nm). Considering these things, an actual relationship between the distance and the force is represented like curves in [82], which is called as force curve obtained from AFM experiments.

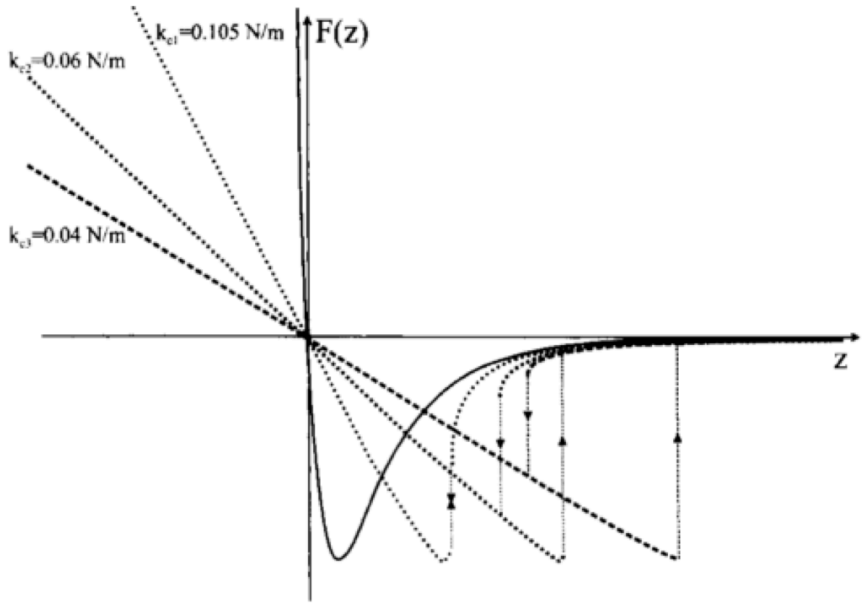

Figure 2.3 (Broken lines) Force curves using cantilevers with different spring constant. (Solid line) Lennard-Jones potential curve [82]. Reprinted from *Surface Science Reports*, **34**, B. Cappella, G. Dietler, "Force-distance curves by atomic force microscopy", 1-104, Copyright 1999, with permission from Elsevier.

When we measure surface of hard solids such as oxides, usually the cantilever with the probe is scanned in the region where repulsive force is dominant ($F(z) > 0$). During the scanning, the atomic force detected by the probe is kept constant by a feedback system. The force is related to the displacement of the probe, which is detected by an optical system using laser light reflected at a backside of the cantilever. In the system, reflected laser proceeds to a position sensitive detector (PSD, Figure 2.4), where the position of received laser depends on bending of the cantilever derived from the displacement (optical-lever type system). That signal is utilized for feedback of piezoelectric sample stage to keep the displacement, resulting in constant force. The feedback values are mapped to depict topography of the sample.

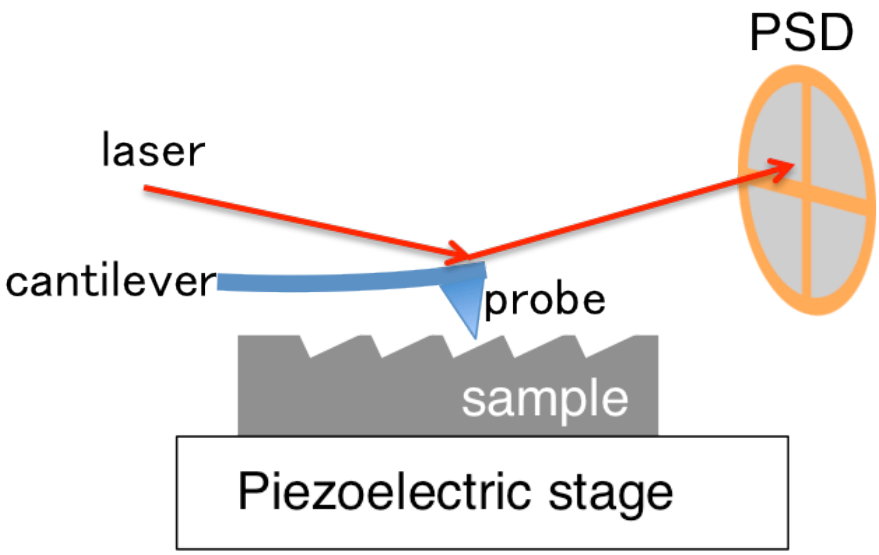

Figure 2.4 Schematic image of optical-lever system in AFM to detect displacement of the probe.

Such measuring mode which keeps the force constant mainly in the repulsive region is called as contact mode AFM. Moreover, tapping mode AFM, which is also called as dynamic force microscopy (DFM), is also used for surface observation.

In DFM, an oscillated cantilever by a piezoelectric excitation component is made approach close to a sample and contact cyclically (cyclic contact field, Figure 2.5). Then, a change in the oscillation amplitude of the cantilever, which depends on the force between the probe and the surface, is utilized for feedback as in the case of the contact mode.

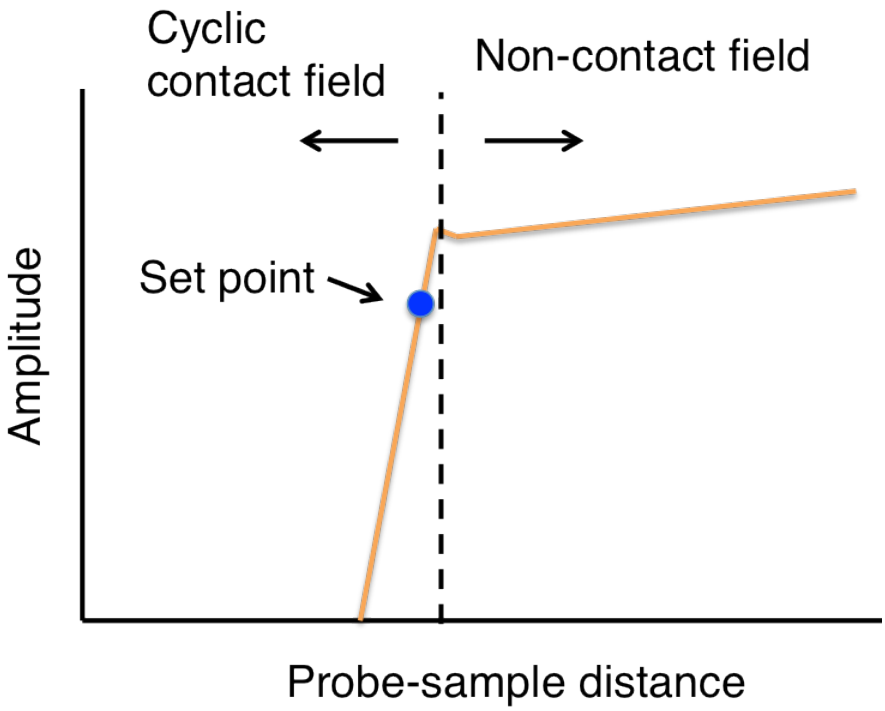

Figure 2.5 Relationship between oscillation amplitude and probe-sample distance. The amplitude is determined at a set point in cyclic contact field for scanning a sample.

In terms of a resonance frequency property of the oscillated cantilever, resonance curve is shifted according to the force between the probe and the sample, resulting in amplitude modulation (Figure 2.6, called as Q curve).

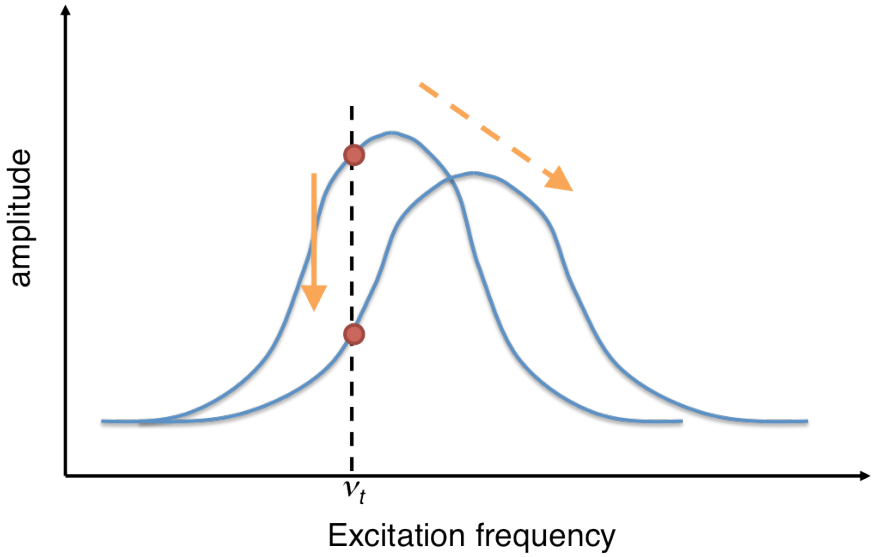

Figure 2.6 Oscillation amplitude plots against frequency (Q curve). A set point frequency is near the resonance frequency. If the probe receives interaction, resonance frequency will shift and then amplitude at the set point will also change.

Q-value of the Q curve is an indication of the oscillation property, which is defined as an inverse of full width at half maximum (FWHM). The higher the Q-value is, the better sensitivity the measurement shows.

In contrast to contact mode AFM, DFM can reduce damage on a sample during scanning due to only periodic contact to the sample. For further decrease in damage, use of cantilevers with small spring constant k and small oscillation amplitude are effective. In chapter4, I utilized a cantilever with small k, even 3.5 N/m, to record clear images.

In this study, a commercial SPM system (E-sweep, Hitachi High-Tech Science Corporation) was used for AFM measurements.

2.3 Ultraviolet-visible absorption spectroscopy [83]

In absorption spectroscopy, absorbance A is determined as;

$$A = -\log \frac{I}{I_0} \ , \tag{2.7}$$

where I and I_0 are the intensity of transmitted and incident light. In a measurement for a molecular solution sample (Chapter4), absorbance is also described by Lambert-Beer law as follows;

$$A = -\log \frac{I}{I_0} = \varepsilon l c \ , \tag{2.8}$$

where ε is the absorption coefficient, l is the optical path length (cell size, in this study $l = 1$ cm), and c is the concentration of the solution.

However, supporting substances such as optical cells (for solution) and substrates (for thin film) are practically measured together. Thus the absorbance is estimated by;

$$A = -\log \frac{T}{T_0} \ , \tag{2.9}$$

where T and T_0 are the transmittance of a sample (including a support) and a blank.

Moreover, in polarized absorption spectroscopy measurements at various incident angles in my study (Chapter4), effects of reflection were corrected. Reflectance is significantly different between s- and p-polarized light according to Fresnel equations [84];

$$R_s = \left| \frac{\cos\alpha - \sqrt{n_{21}^2 - \sin^2\alpha}}{\cos\alpha + \sqrt{n_{21}^2 - \sin^2\alpha}} \right|^2 \tag{2.10}$$

$$R_p = \left| \frac{n_{21}^2\cos\alpha - \sqrt{n_{21}^2 - \sin^2\alpha}}{n_{21}^2\cos\alpha + \sqrt{n_{21}^2 - \sin^2\alpha}} \right|^2 \ , \tag{2.11}$$

where R_s and R_p are the reflectance for s- and p-polarized light, α is the incident angle and n_{21} is the refractive index of medium 2 against medium 1. Reflectance of s- and p-polarized light for a $n_{21} = 2.42$ system is plotted against incident angle in Figure 2.7. The angle at which reflectance of p-polarized light becomes 0 is called as Brewster's angle.

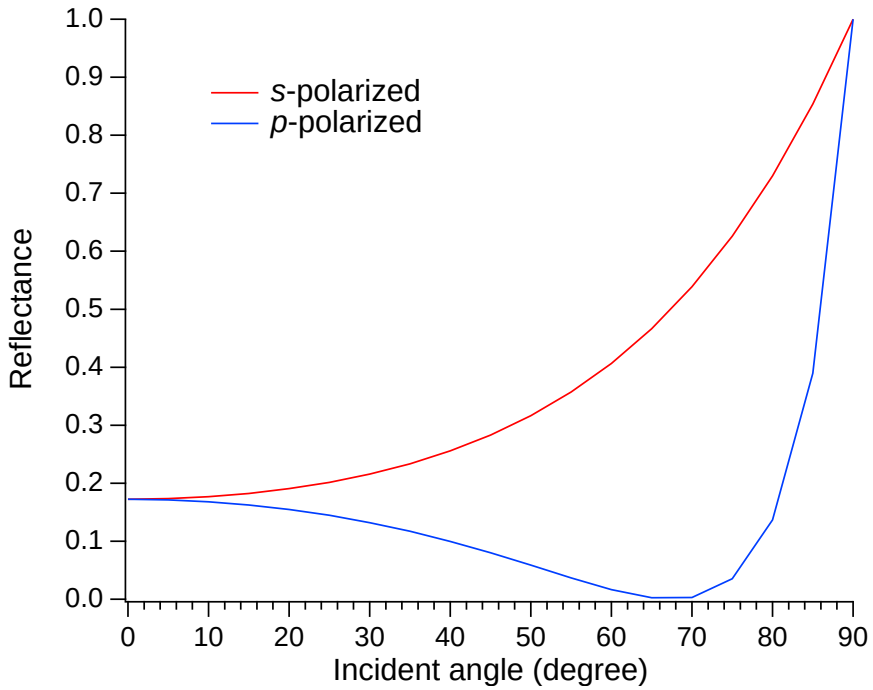

Figure 2.7 Reflectance for (red line) *s*- and (blue line) *p*-polarized light at an interface of medium 1 (incident side) and medium 2. The refractive index n_{21} is 2.42, which equals to that of $SrTiO_3$ at 660 nm [85].

In this study, ultraviolet-visible absorption measurements were performed by a spectrophotometer system from JASCO.

2.4 X-ray reflectivity (XRR) measurement [86]

In XRR measurements, X-ray incident light is irradiated to a flat sample at a grazing incident angle. It is a non-destructive method to evaluate properties of thin film samples such as thickness, even if a multilayer sample is measured.

X-ray generally shows total reflection due to smaller refractive index of the sample than that of the air. Once incident angle exceeds the total reflection angle, the X-ray intrudes into the sample and reflection intensity decreases in proportion to the fourth power of the incident angle. This attenuation of reflection intensity is analyzed. In (multilayer) thin film samples, there is interference of X-ray with X-ray reflected at each

interface, which provides characteristic reflection spectrum with oscillation structure. An oscillation period of the reflection spectrum is related to the thickness; thicker films exhibit shorter oscillation periods.

In practical, XRR spectra can be analyzed by fitting experimental curves with simulation ones like Figure 2.8, using a suitable software.

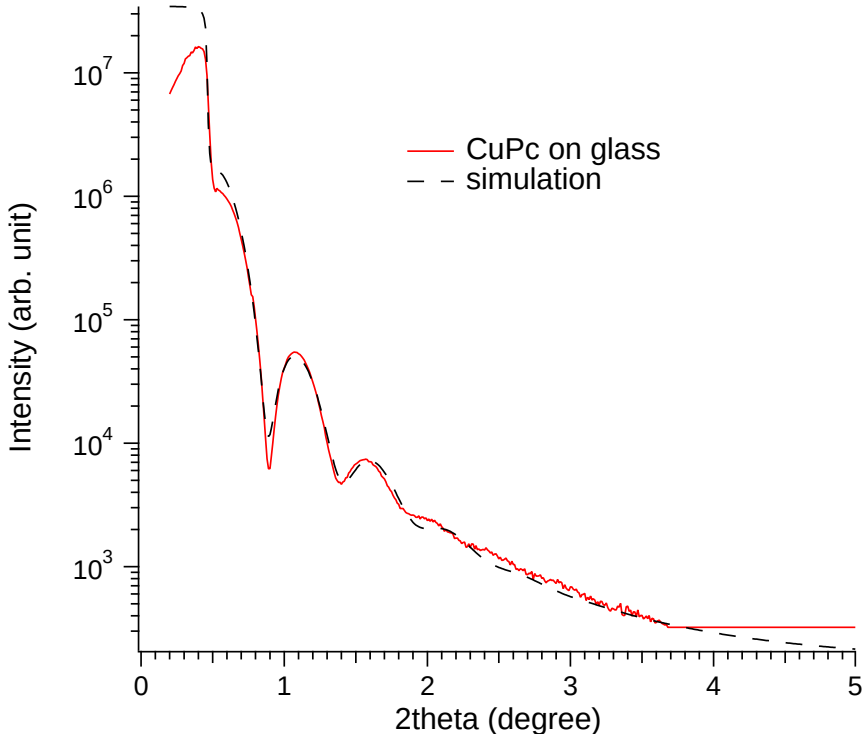

Figure 2.8 XRR profile of a thermally deposited copper phthalocyanine thin film on a glass substrate with a simulation curve. The estimated thickness is about 16 Å.

In this study, XRR spectra were measured and recorded by D8 Discover system from Bruker AXS. Leptos software package was used for simulation.

2.5 X-ray photoemission spectroscopy (XPS) [48, 87]

In XPS, photoelectrons excited by X-ray irradiation are analyzed to investigate electronic structures of target samples. This technique is surface sensitive due to very short

mean free path length of electrons. Photoelectrons within only several tens Å from surface can escape from the sample without energy loss, resulting in the surface-sensitive measurement.

In a XPS equipment, kinetic energies of photoelectrons are detected to know their binding energies in the sample. The binding energies are obtained by following an equation that;

$$E_b = h\nu - E_k - \phi \quad , \tag{2.12}$$

where E_b is the binding energy, $h\nu$ is the energy of irradiated X-ray, E_k is the detected kinetic energy, and ϕ is the work function of the equipment. Thus, the detected kinetic energy provides information about binding energy.

Because the binding energy of an electron in an inner shell is at a characteristic energy region, element-specific analysis is possible. Intensity of photoelectrons is plotted against binding energy to be called as energy distribution curve. Peak shift in that plot is correlated to the valence of the element, from which chemical states of the element can be estimated.

In this study, a commercial XPS system (PHI5000 VersaProbe, ULVAC-PHI) was used for XPS measurements.

2.6 Crystal truncation rod (CTR) analysis [88–91]

X-ray crystal truncation rod (CTR) analysis enables us to obtain information about a crystalline solid surface to estimate its structure. X-ray CTR represents X-ray scattering from a crystal truncated in any direction, in other words, by surface.

The diffraction pattern of a perfectly infinite crystal is known to consist of narrow δ functions at the reciprocal space lattice points, where the Laue conditions are fulfilled

three dimensionally. However, in the case of finite-size effect concerned, the diffraction peaks are changed from δ functions to broadened ones depending inversely on the dimension of the crystal. Thus, diffuse streaks can be observed connecting the Bragg points for the finite size crystal. In case of a substrate type crystal which can be regarded to be infinite in surface plane direction and finite in surface normal direction, the diffraction intensity diffuses especially to the direction perpendicular to the surface in reciprocal space. So, crystal truncation "rod" scattering with large intensity nodes at Bragg points can be observed.

To estimate the structure from the experimental scattering profile, a structural model and its structural factor F_{hkl} are needed;

$$F_{hkl} = \sum_j f_j e^{-B_j Q^2/(16\pi^2)} e^{2\pi i(hx_j+ky_j+lz_j)} \quad , \tag{2.13}$$

where f is the atomic scattering factor, B is the Debye-Waller parameter, Q is the momentum transfer, h,k,l are the diffraction indices, and x_j, y_j, z_j are the position in fractional coordinates.

In this study, the structural factor was calculated based on cubic bulk perovskite oxide lattice. Thus, a simple surface coordinate system was defined that the lattice vector $\boldsymbol{a}_1$ and $\boldsymbol{a}_2$ are in the surface plane and $\boldsymbol{a}_3$ is perpendicular to the surface plane, where negative direction of z axis corresponds to the outward side of the surface. The total structural factor of the surface scattering is provided by the sum of surface and bulk contributions like;

$$F_{sum} = F_{surf} + F_{bulk} \quad , \tag{2.14}$$

where the boundary separating the surface region and the bulk region is set to be $z = 0$ as shown in Figure 2.8.

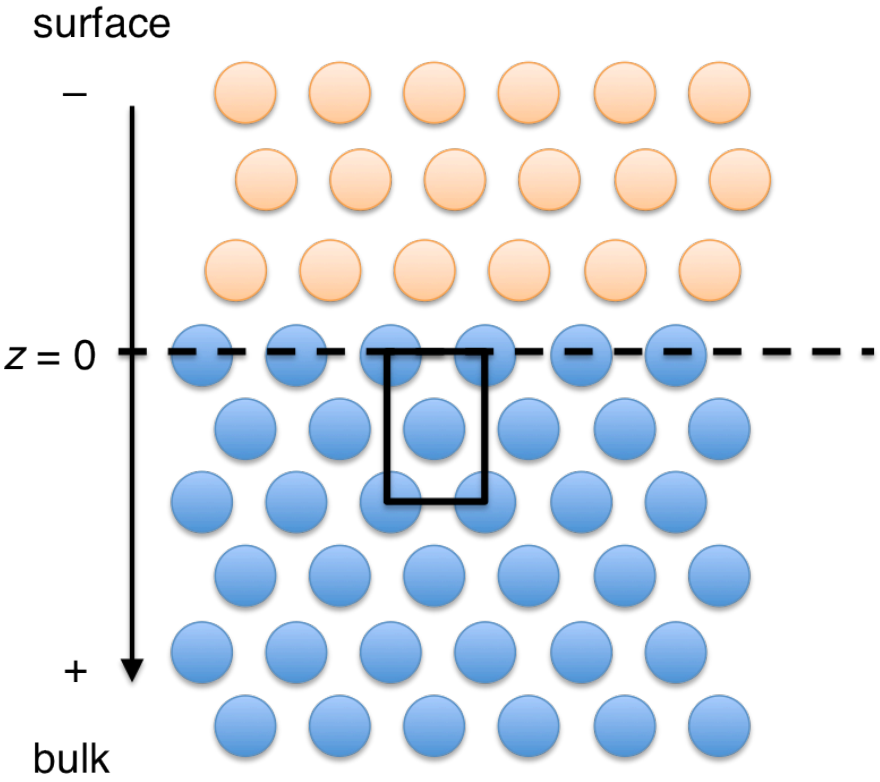

Figure 2.9 Schematic image of the surface structure model with a z coordination axis for calculation of the structural factor. $z \geq 0$ region consist of the bulk crystal. $z < 0$ region represents surface layer. However, its coordinate has to be considered on a basis of bulk crystal lattice. A rectangle in bulk region represents a bulk unit cell.

F_{surf} and F_{bulk} are represented as;

$$F_{surf} = \sum_{j}^{\substack{surface \\ unit\ cell}} f_j \theta_j e^{-B_j Q^2/(16\pi^2)} e^{2\pi i(hx_j+ky_j+lz_j)} \tag{2.15}$$

$$F_{bulk} = \sum_{j=\infty}^{0} F_u e^{2\pi i l j} e^{j\alpha} \quad , \tag{2.16}$$

where F_u is the bulk unit cell structural factor;

$$F_u = \sum_{j}^{\substack{bulk \\ unit\ cell}} f_j e^{-B_j Q^2/(16\pi^2)} e^{2\pi i(hx_j+ky_j+lz_j)} \quad . \tag{2.17}$$

θ is the occupancy parameter and α is the attenuation factor, which results in that just a finite amount of unit cells is summed to be F_{bulk}. It is then described as;

$$F_{bulk} = F_u \frac{1}{1 - e^{-2\pi i l} e^{-\alpha}} \quad . \tag{2.18}$$

In this study, only (00L) line profiles were used, so that x and y coordinates of the atoms in the models had not to be considered ($h = 0$ and $k = 0$). Only z coordinates were significant.

The CTR scattering measurements (Chapter4) was performed using BL-4C at the Photon Factory, KEK, Japan by collaborators. The intensity of X-ray was 12.4 keV.

2.7 Calculation method [92, 93]

In my study, density functional theory (DFT) calculation was performed to estimate adsorption energy of phthalocyanine on perovskite oxides.

In DFT method, properties of a system is expressed by functionals of electron density. DFT is based on the two Hohenberg-Kohn theorems [94] that (1) an external potential can be determined by a non-degenerated ground state electron density uniquely (2) trial electron density provides lager energy functional than minimum energy for the system, otherwise provides the minimum energy when the trial electron density is equal to the ground state.

Actually, DFT calculation is performed with Kohn-Sham equations [95];

$$\left(-\frac{\hbar^2}{2m}\nabla^2 + V_{eff}\right)\psi_i = \varepsilon_i \psi_i \quad . \tag{2.19}$$

Within this fictitious Kohn-Sham system, where we think about non-interacting particles under the Kohn-Sham potential V_{eff}, the equation is solved self-consistently as the trial electron density will be equal to the density obtained from Kohn-Sham orbitals, which is provided by;

$$n(\boldsymbol{r}) = \sum_{i}^{N} |\psi_i(\boldsymbol{r})|^2 \ . \tag{2.20}$$

The Kohn-Sham potential can be expressed as;

$$V_{eff}(\boldsymbol{r}) = V_{ext}(\boldsymbol{r}) + e^2 \int \frac{n(\boldsymbol{r}')}{|\boldsymbol{r}-\boldsymbol{r}'|} d\boldsymbol{r}' + \frac{\delta E_{\mathrm{XC}}[n]}{\delta n(\boldsymbol{r})} \ , \tag{2.21}$$

where the last term is the exchange-correlation potential functional $V_{\mathrm{XC}}[(n)]$.

Approximation of the exchange-correlation functionals is one of the most important factors for solutions of the equation with better precision. Representative approximations are local density approximation (LDA) level and generalized gradient approximation (GGA) level, which depends on the gradient of the density as well as the density itself [96].

In this study, I used two calculation packages. Gaussian09* was used for optimizing the structure of the phthalocyanine molecules. Unrestricted B3LYP (Becke 3-Lee-Yang-Parr) level functional was adopted with 6-31+G(d) basis set. VASP (Vienna *ab initio* Simulation Package) [97] was used for calculation of surface adsorption models. GGA-PBE (Perdew-Burke-Ernzerhof) level functional was adopted, using a plane-wave basis set whose cutoff energy was 400 eV with PAW (Projector Augmented Wave) pseudopotential. The Brillouin zone was sampled only at the gamma point (*k*-point sampling). The contribution of van der Waals (dispersion) interaction to calculated total energies was

*Gaussian 09, Revision B.01, M. J. Frisch, G. W. Trucks, H. B. Schlegel, G. E. Scuseria, M. A. Robb, J. R. Cheeseman, G. Scalmani, V. Barone, B. Mennucci, G. A. Petersson, H. Nakatsuji, M. Caricato, X. Li, H. P. Hratchian, A. F. Izmaylov, J. Bloino, G. Zheng, J. L. Sonnenberg, M. Hada, M. Ehara, K. Toyota, R. Fukuda, J. Hasegawa, M. Ishida, T. Nakajima, Y. Honda, O. Kitao, H. Nakai, T. Vreven, J. A. Montgomery, Jr., J. E. Peralta, F. Ogliaro, M. Bearpark, J. J. Heyd, E. Brothers, K. N. Kudin, V. N. Staroverov, T. Keith, R. Kobayashi, J. Normand, K. Raghavachari, A. Rendell, J. C. Burant, S. S. Iyengar, J. Tomasi, M. Cossi, N. Rega, J. M. Millam, M. Klene, J. E. Knox, J. B. Cross, V. Bakken, C. Adamo, J. Jaramillo, R. Gomperts, R. E. Stratmann, O. Yazyev, A. J. Austin, R. Cammi, C. Pomelli, J. W. Ochterski, R. L. Martin, K. Morokuma, V. G. Zakrzewski, G. A. Voth, P. Salvador, J. J. Dannenberg, S. Dapprich, A. D. Daniels, O. Farkas, J. B. Foresman, J. V. Ortiz, J. Cioslowski, and D. J. Fox, Gaussian, Inc., Wallingford CT, 2010.

simulated by using the semiempirical correction method DFT-D2 [98]. In this method, the total energy is expressed as

$$E_{DFT-D2} = E_{KS-DFT} + E_{disp} \quad , \tag{2.22}$$

where E_{KS-DFT} is an usual Kohn-Sham energy and E_{disp} is a dispersion correction term. The correction is calculated as follows;

$$E_{disp} = -s_6 \sum_{i=1}^{N_{at}-1} \sum_{j=i+1}^{N_{at}} \frac{C_6^{ij}}{r_{ij}^6} f_{damp}(r_{ij}) \quad , \tag{2.23}$$

where s_6 is a global scaling factor (herein 0.75 for PBE), N_{at} is the number of atoms in the system, C_6^{ij} is a dispersion coefficient for atom pair ij, r_{ij} is an interatomic distance, and f_{damp} is a damping function, which is described as;

$$f_{damp}(r_{ij}) = \frac{1}{1 + e^{-d(r_{ij}/R_0^{ij} - 1)}} \quad , \tag{2.24}$$

where d is a damping parameter and R_0^{ij} is a sum of van der Waals radii. C_6^{ij} and R_0^{ij} can be obtained by;

$$C_6^{ij} = \sqrt{C_6^i C_6^j} \tag{2.25}$$

$$R_0^{ij} = R_0^i + R_0^j \tag{2.26}$$

Parameters C_6 and R_0 needed for the correction are implemented in VASP for elements from H to Xe, however, not for La. Those for La were determined by myself according to [99, 100].

Chapter 3

Langmuir-Blodgett method

3.1 Introduction

LB method is one of the wet processes used to fabricate multilayers with well-defined molecular orientation and controllable thickness. For LB films of phthalocyanines, peripheral substituents such as bulky tert-butyl group and long alkyl chains are required to be dissolved in hydrophobic organic solvent, so that the solution can be spread at air-water interface. In order to control the molecular orientation in Langmuir monolayer on water subphase, it would be effective to select proper peripheral substituents because characters of substituents such as length and hydrophilicity have crucial effects on molecular orientation at air-water interface, resulting in peculiar surface pressure-area isotherms (π-A curves), as mentioned in Chapter1. In some cases, central metals of phthalocyanines also influence the orientation because of difference in metallomacrocycle-water interactions, *i.e.* the hydrophilicity [58].

In this chapter, we fabricated LB monolayers of octaoctyloxy metallophthalocyanine (MOOPc, central metal M = Cu and Zn) and copper tetra(tert-butyl) phthalocyanine

Parts of this chapter have been published in *e-Journal of Surface Science and Nanotechnology*. Reprinted from *e-J. Surf. Sci. Nanotech.*, **13**, "Effect of Central Metals on Langmuir-Blodgett Monolayers of Phthalocyanines with Flexible Substituents", S. Kojima, T. Fukumura, T. Hasegawa, 155-158, Copyright 2015, with permission from The Surface Science Society of Japan.

(CuTTBPc) as a reference. The former is representative phthalocyanine molecule containing flexible long hydrophobic substituents, whereas the latter is one of the phthalocyanines with rigid structure.

*M*OOPcs are expected to be inclined to some extent due to the alkyl chains on water subphase. I compared effects of central metals not only on the orientations but also on transfer of the Langmuir monolayers onto solid supports, of which process should be important for the use of the phthalocyanine monolayer with interesting multiple oxides. Although I used glass substrates here, withdrawing vertical transfer onto the hydrophilic surface was adopted in anticipation of collaboration with multiple oxide substrate instead because clean oxide surface is inherently hydrophilic.

AFM measurements, absorption spectroscopy and XRR measurements were performed to discuss the LB monolayers.

3.2 Experimental details

CuTTBPc, CuOOPc and ZnOOPc (Sigma-Aldrich) were used without further purification. CuTTBPc, CuOOPc, and ZnOOPc were dissolved in chloroform (Wako Chemical), where each concentration was 2.2×10^{-4} M, 9.0×10^{-5} M, and 9.0×10^{-5} M, respectively. Glass plates were used as substrates. The surface of substrates were made hydrophilic by immersion in CH_3OH:HCl aq followed by conc. H_2SO_4 aq, and were rinsed by ultrapure water. The LB equipment of USI Co. Ltd. was used. The substrate was dipped into ultrapure water in advance. Each solution of the phthalocyanine was spread onto ultrapure water in the trough at $15-20$ °C. After the evaporation of the solvent, the floating layer was compressed by two barriers at a rate of $2-3$ mm/min. Surface pressure was kept at 3 or 20 mN/m for 15 min before deposition. LB monolayer was deposited by withdrawing the glass substrate at a rate of 0.4 and 2 mm/min for CuT-

TBPc and *M*OOPc, respectively. The surface morphology of the films were measured by atomic force microscope in tapping mode using cantilevers with nominal spring constant of 28 N/m. Absorption spectra of the films in ultraviolet-visible region were measured in air by JASCO V-670. X-ray reflectivity measurements were performed by D8 Discover system from Bruker AXS.

3.3 Results and discussion

3.3.1 π-A isotherms and estimation of orientation

Figure 3.1 shows π-A curves for monolayers of CuTTBPc (Figure 3.1(a)) and *M*OOPc (*M* = Cu, Zn) (Figure 3.1(b)). The limiting areas were 0.44 nm^2 , 1.04 nm^2 , and 1.33 nm^2 for CuTTBPc, CuOOPc, and ZnOOPc, respectively. The π-A curve of CuTTBPc increased abruptly around the limiting area, being consistent with the previous study [101]. This small limiting area indicates a perpendicular orientation to the subphase with dense molecular packing [102]. In contrast, CuOOPc and ZnOOPc showed gradual increase in the π-A curves with significantly larger limiting area than that of CuTTBPc. They were slightly smaller than the size of phthalocyanine framework 1.7 nm^2 [58]. This result represents relatively in-plane alignment of the molecules with small molecular packing density, originated from the eight long and flexible alkoxy chains of *M*OOPcs. More quantitatively, the surface pressure of ZnOOPc started increasing at a larger area than that of CuOOPc. Assuming that the area per Pc framework is 1.7 nm^2 as mentioned in above, orientation angle of CuOOPc is estimated to be 52°, and that of ZnOOPc to be 39° with respect to the surface. It is noted that in actual case, the angles should be a bit larger because the molecules are tethering substituents.

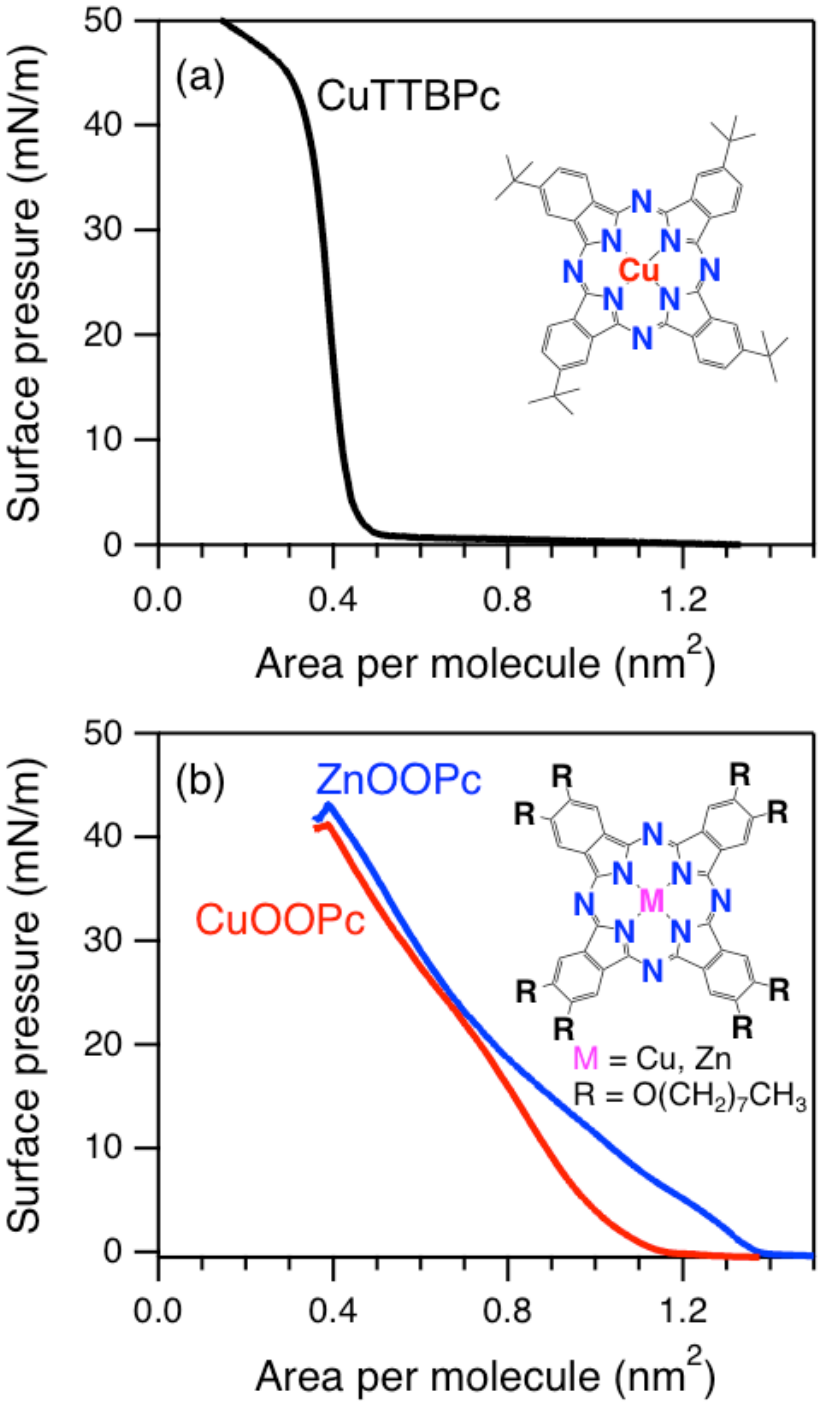

Figure 3.1 Surface pressure-area isotherms for (a) CuTTBPc (a) and (b) *M*OOPc (*M* = Cu and Zn) monolayers. In inset each molecular structure is shown.

CuOOPc and ZnOOPc formed different assembly at lower surface pressure. Hence, not only peripheral substituents but also central metals influenced the orientation and

the molecular assembly in the Langmuir monolayers. This result is probably due to the hydrophilicity of metallomacrocycle, *i.e.* the difference in coordination of water molecule to central metal [58]. On the other hand, both molecules showed similar π-A curves above the surface pressure of 20 mN/m. This result suggests similar assembly of both molecules due to dominant intermolecular interaction between phthalocyanines over the coordination of water molecule especially for ZnOOPc, however, the detailed orientations were different as described below.

3.3.2 Langmuir monolayer transfer onto the substrate

Langmuir layers on water trough of each *M*OOPc phthalocyanine were transferred onto glass substrates at lower and higher surface pressure. Area per molecule is clearly different at lower pressure part but similar at higher pressure part as mentioned above (Figure 3.1). Representatively, 3 mN/m for lower surface pressure and 20 mN/m for higher surface pressure were adopted. On transfer, I evaluated Transfer Ratio (TR), which is defined by,

$$\mathrm{TR} = \frac{\text{Reduced trough area during transfer}}{\text{Area of the substrate}} \tag{3.1}$$

TR indicates efficiency of transfer from water subphase to a substrate. The reduced area during transfer can be estimate from Figure 3.2 showing time evolution of the trough area after reaching a set point of surface pressure, 3 or 20 mN/m for each *M*OOPc monolayer. The surface pressure was kept for 900 sec, and then the vertically immersed glass substrate was withdrawn. Deposition was finished at 1410 sec. Accordingly, I estimated TRs to be 0.47 (CuOOPc 3 mN/m), 0.56 (CuOOPc 20 mN/m), 0.82 (ZnOOPc 3 mN/m), and 1.1 (ZnOOPc 20 mN/m), respectively. TR less than 1 suggests imperfect transfer of Langmuir layer. Herein, CuOOPc, at both low and high surface pressure, showed obviously less values. This suggests that the Langmuir layer of CuOOPc has some difficulty

in transferring to the vertically withdrawn substrate.

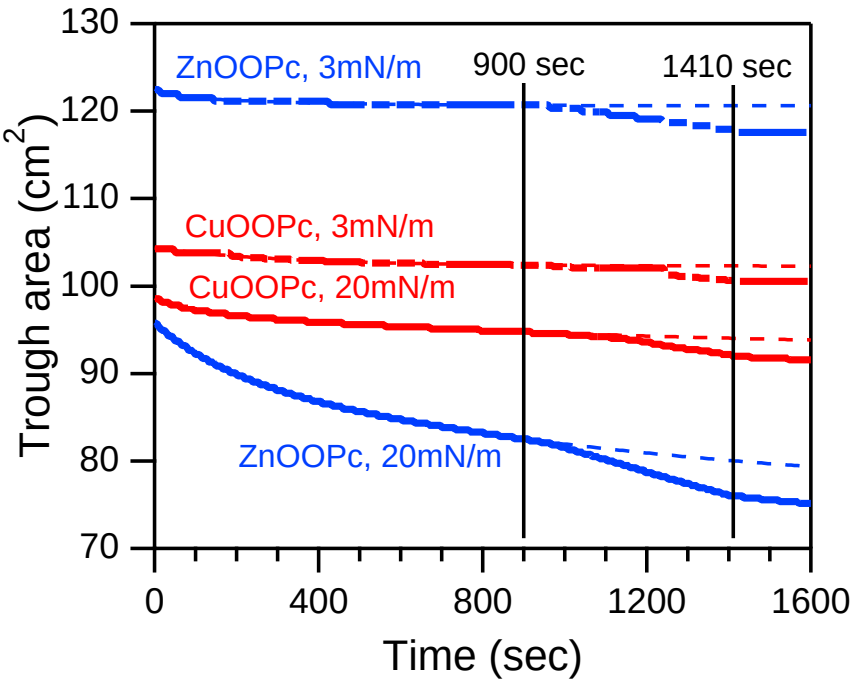

Figure 3.2 Time evolution of the trough area after reaching prescribed surface pressure for CuOOPc and ZnOOPc monolayers. Dotted lines are fitting curves until withdrawing substrates.

For further discussion, absorption measurement for UV-visible region and atomic force microscope (AFM) measurement should be considered.

3.3.3 AFM and UV-vis absorption measurement

Figure 3.3 shows atomic force microscope images for the monolayers of CuTTBPc, CuOOPc and ZnOOPc. Surface morphology of CuTTBPc monolayer transferred at 20 mN/m showed small circular aggregates (Figure 3.3(a)) probably due to the high surface pressure [103]. *M*OOPc monolayers showed variable morphology depending on surface pressure and central metals. For the surface pressure of 3 mN/m, CuOOPc monolayer showed flat and homogeneous surface representing uniform distribution of molecules as shown in Figure 3.3(b). On the other hand, the ZnOOPc film for the same surface pres-

sure showed the assembly of islands with partial coverage as shown in Figure 3.3(d). The observed difference in the surface morphology should be attributed to different molecular orientation, because each area at surface pressure of 3 mN/m was significantly different as seen in Figure 3.1(b). The height of ZnOOPc islands was about 1.6 nm, which is much smaller than the lateral size of ZnOOPc molecule containing long octyloxy chains.

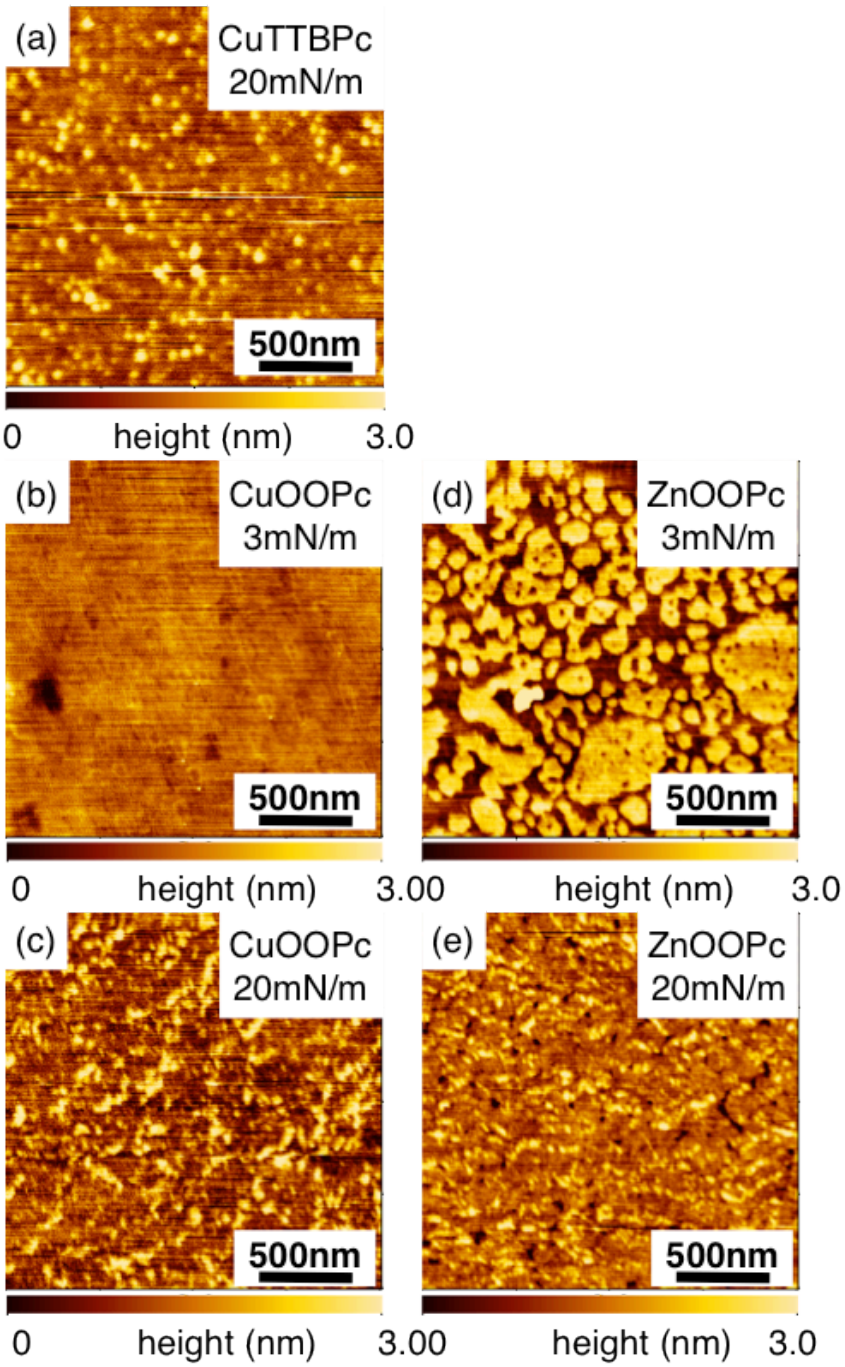

Figure 3.3 AFM images of LB monolayers deposited at different surface pressures. (a) CuTTBPc at 20 mN/m. CuOOPc (b) at 3 mN/m and (c) at 20 mN/m. ZnOOPc (d) at 3 mN/m and (e) at 20 mN/m.

Considering TRs and morphology from AFM, TR of ZnOOPc 0.82 at 3 mN/m, which is slightly less than 1, should be reasonable. On the other hand, CuOOPc at 3 mN/m showed homogeneous morphology although its TR is much worse. As for the

monolayers at 20 mN/m, ZnOOPc showed the values close to unity and CuOOPc showed a smaller value as in the case of 3 mN/m, while their surface does not have island-like morphology.

To explain this situation, I measured absorption spectra at 3 different points for each sample (Figure 3.4). The recorded spectra of CuOOPc samples showed large variation in absorbance from one to another. On the other hand, the spectra of ZnOOPcs were almost identical. These facts indicate that some parts of the substrate were not covered by CuOOPc monolayer. In other words, CuOOPc LB monolayer is inhomogeneous in a macroscopic sense. In the case of ZnOOPc, Langmuir layers are homogeneously transferred to the substrates.

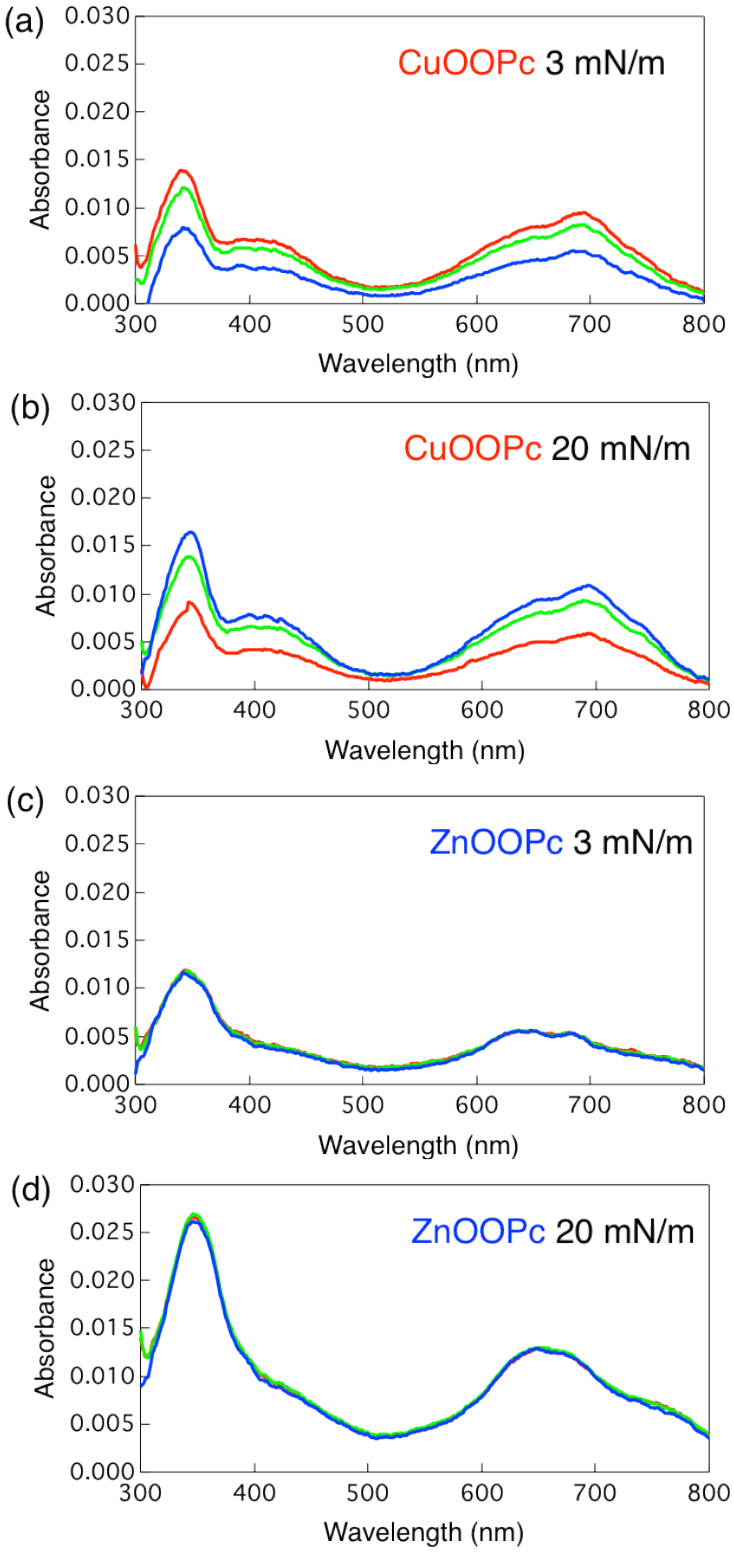

Figure 3.4 Absorption spectra at different 3 points within each sample. CuOOPc (a) at 3 mN/m and (b) at 20 mN/m. ZnOOPc (c) at 3 mN/m and (d) at 20 mN/m.

This difference in homogeneity of LB monolayer is surely attributed to the central metals. Actually, the detailed mechanism of deposition from water subphase to the substrate is unclear. However, hydrophilicity may play a main role because transfer to the hydrophilic substrate should occur at the tip of meniscus. On withdrawing the substrate, the Zn phthalocyanine molecules move onto the substrate with residual water due to its familiarity with water.

Moreover, I compared UV-vis absorption spectra of the 4 samples with that of CuTTBPc in Figure 3.5, where, for CuOOPcs, I employed the spectra recorded at the center region of each sample in Figure 3.4. In comparison with CuTTBPc monolayer, the absorbance of CuOOPc and ZnOOPc monolayers was smaller because of the lower packing density of the molecules. For CuOOPc monolayers, the absorbance was slightly increased with increasing surface pressure, suggesting slight increase in the packing density. On the other hand, ZnOOPc showed different tendency. For the surface pressure of 3 mN/m, the absorbance was smaller reflecting much inclined molecular orientation of ZnOOPc molecules with partial coverage (Figure 3.3(d)), as was supported by the significantly larger limiting area at the onset of surface pressure (Figure 3.1(b)). For the surface pressure of 20 mN/m, however, the absorbance was nearly doubled, probably due to the significantly compressed assembly by further compression during keeping the surface pressure (Figure 3.2).

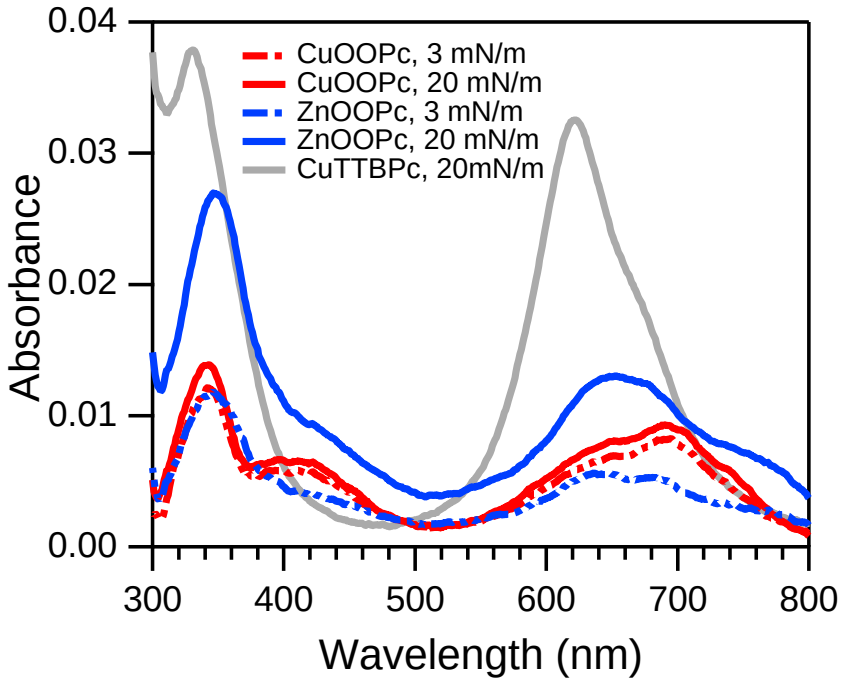

Figure 3.5 Absorption spectra of LB monolayers deposited at different surface pressures.

Figure 3.2 shows time evolution of the trough area after reaching a set point of surface pressure, 3 or 20 mN/m for each monolayer. Among them, trough area of ZnOOPc at 20 mN/m decreased rapidly, indicating that the high surface pressure induced further compression to maintain the surface pressure. On the other hand, CuOOPc at 20 mN/m did not show such decrease in surface pressure. Accordingly, ZnOOPc monolayer became denser under further compression probably due to intermolecular π-ring attractive interaction. Some literatures about single crystal structure analyses of phthalocyanines have reported that intermolecular distance between molecular planes depends on central metals [104, 105]. Although these *M*OOPc LB monolayers are not the case of single crystals, molecular planes of ZnOOPc molecules might be able to get closer at higher surface pressure. Thus, π-π interaction of ZnOOPc might be more effective by releasing coordinated water molecules, leading to the supported dense packing. However, some of ZnOOPc molecules should still keep the coordination because LB monolayers are

regarded as assemblies of many aggregates composed of several molecules [106], not a single domain composed of the whole molecules. Then, since hydrophilicity of the Langmuir monolayer was kept as a whole, the homogeneous transfer onto the substrate was achieved.

Turning to UV-vis absorption spectra again (Figure 3.5), ZnOOPc monolayer at 3 mN/m has two absorbance peaks at 647 nm and 682 nm, while the monolayer at 20 mN/m has only one peak at 654 nm. The high surface pressure induced dense packing of ZnOOPc molecules. Consequently, Q-band, which represents absorption band of phthalocyanine around 600 - 700 nm, of ZnOOPc at 20 mN/m showed blue-shift possibly due to the intermolecular interaction [107]. On the other hand, both absorption spectra for 3 mN/m and 20 mN/m show almost the same shapes for CuOOPc representing the similar molecular orientations irrespective of the surface pressure.

3.3.4 X-ray reflectivity measurement

X-ray reflectivity (XRR) measurement can provide information of thickness, which is useful for estimating structures of the ultrathin layers. The thickness of the reference CuTTBPc monolayer was evaluated as 2.1 nm from XRR, which was close to the in-plane diagonal size of CuTTBPc, 1.95 nm [108]. This result supports the “edge-on” like orientation of CuTTBPc monolayer.

I also performed XRR measurements for the *M*OOPc samples. Figure 3.6 shows the obtained XRR curves and results of curve fitting for *M*OOPc LB monolayers. The estimated thickness is labeled on each panel. Among them, ZnOOPc monolayer deposited at 3 mN/m showed especially small thickness.

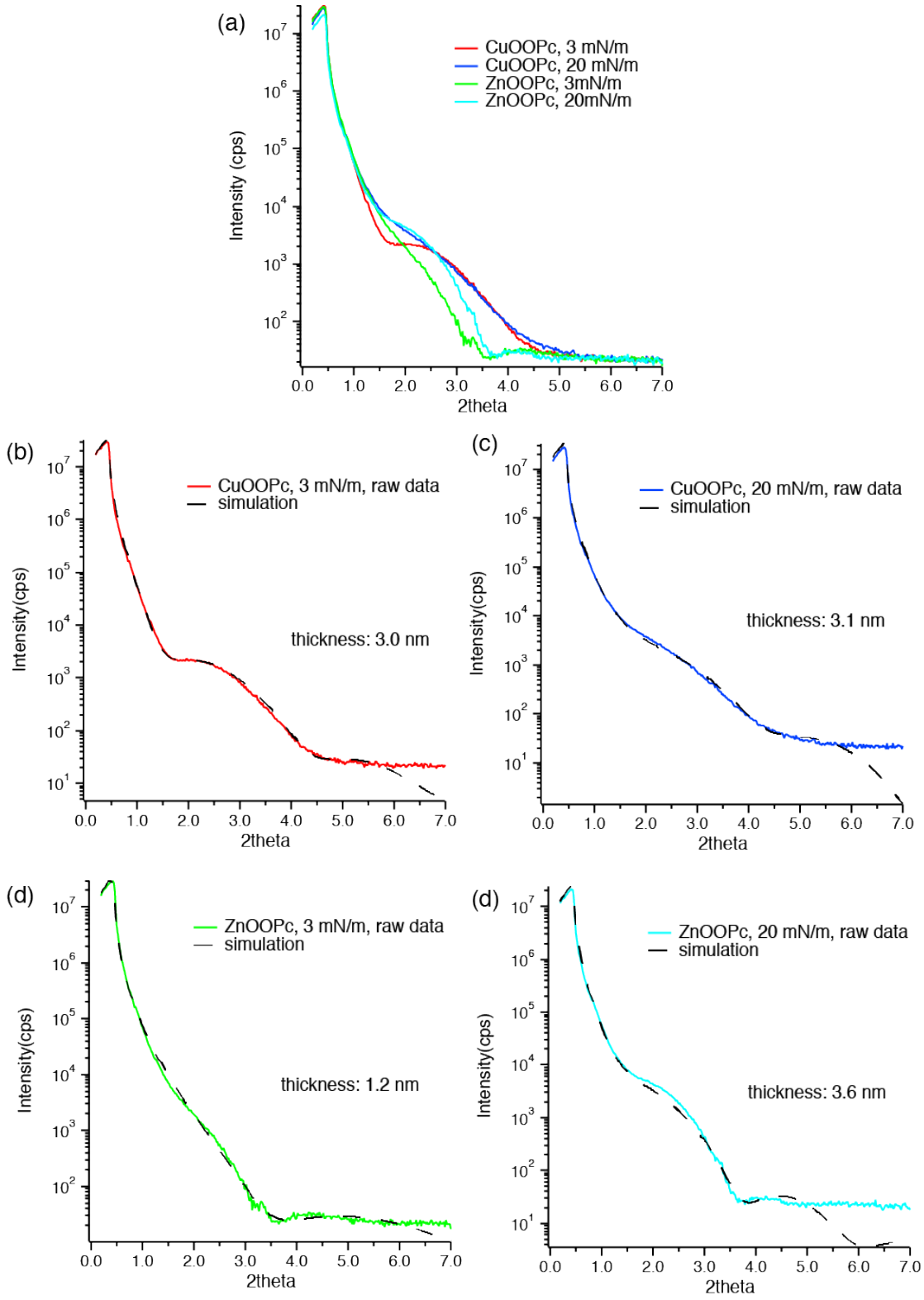

Figure 3.6 XRR curves of *M*OOPc LB monolayers. 4 experimental curves are plotted together in (a). Each curve is shown separately with its simulated curve and estimated thickness in (b)-(e).

Now, I assume the sizes of octyloxy group and phthalocyanine framework to be 1 nm and 1.5 nm, respectively, to depict rough schematic models of the monolayer structures.

Considering these sizes and the thicknesses of monolayers, I proposed the monolayer structural models as shown in Figure 3.7. To be consistent with the relatively higher thickness of CuOOPcs and ZnOOPc at 20 mN/m, the molecules should be "standing", turning their octyloxy groups to the side of the substrates. Among them, ZnOOPc at 20 mN/m is the most dense monolayer as mentioned above. On the other hand, ZnOOPc at 3 mN/m should be different from such cases, considering from the smaller thickness. The phthalocyanine framework of ZnOOPc at 3 mN/m may not be in a perfectly flat geometry as discussed earlier. However, Pc framework is surely closer to the substrate, compared with other *M*OOPc monolayers.

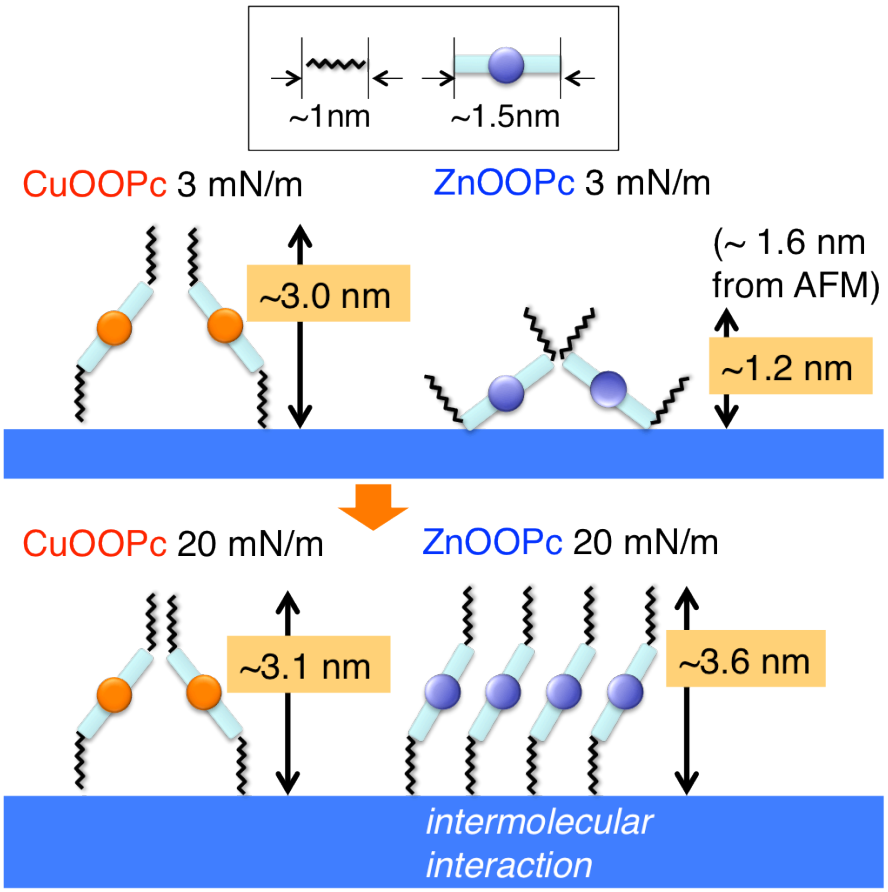

Figure 3.7 Schematic images of the LB monolayer structural models estimated from experimental results. Octyloxy group and phthalocyanine framework models are listed on top of the figure with their assumed sizes.

3.4 Summary

In this chapter, effects of different central metals on the orientation and transfer to the substrate were discussed using *M*OOPc molecules. At the low surface pressure (3 mN/m), larger area per molecule of ZnOOPc implied its inclined orientation more close to the subphase surface than CuOOPc. At the higher surface pressure (20 mN/m), ZnOOPc showed greater compression in contrast to the case of the low surface pressure, when the surface pressure was kept constant. CuOOPc and ZnOOPc also showed different behavior when their Langmuir monolayers were transferred onto substrates. Transfer ratio and UV-vis absorption spectroscopy suggested inhomogeneous transfer onto

the hydrophilic substrates, while ZnOOPc monolayers were transferred homogeneously. The UV-vis absorption spectra also supported the formation of more compressed assembly of ZnOOPc at higher surface pressure. XRR measurements served for estimation of the structures of the deposited films. ZnOOPc deposited at the lower surface pressure showed significantly smaller thickness than others, indicating that its molecular plane orientation should be closer to the substrate surface. These results represent that not only peripheral substituent but also central metal significantly affect LB assembly of phthalocyanine derivatives with flexible substituents by withdrawing vertical transfer.

Chapter 4

Immersion method

4.1 Introduction

In this chapter, I tried to prepare phthalocyanine ultrathin layers by utilizing adsorption in liquid phase. Herein, I used oxide substrates unlike the previous chapter. Briefly speaking, I immersed substrates into phthalocyanine solution to prepare samples. Thus, I call this process as "immersion method" in this thesis. Among oxide substrates, perovskite type oxides, which is one class of the multiple oxides, were deeply examined and discussed for this immersion method because they have attracted attention and have been expected as candidates of materials used in electronics with interesting functionalities as mentioned previously in Chapter 1. Actually, no researches on adsorption on perovskite oxide substrate in liquid phase have been reported except for SAMs formation of fatty acids like stearic acid [39, 109], which makes this immersion method of the macrocyclic molecule intriguing.

As perovskite oxides, I used $LaAlO_3$ (LAO) and $SrTiO_3$ (STO) single crystalline substrates with (100) facet surfaces. LAO and STO are representative substrates used for epitaxial growth of high quality inorganic thin films by vapor process in ultra high vacuum condition. In addition, recently interface between LAO and STO(100) is attracting great attention due to its interesting interface conductivity despite insulating properties

of themselves [110]. Thus, their surface seems worth researching.

As a phthalocyanine molecule, I adopted iron phthalocyanine chloride (FePcCl) in the adsorption experiment. Generally phthalocyanines without substituents showed poor solubility into organic solvents due to large π-π interaction. However, pyridine provides phthalocyanine solubility, and FePcCl especially dissolves even to 10 mg/ml in catalog specifications (Sigma-Aldrich). Because I also tried mixed solvent which has lower solubility than pure pyridine to investigate solvent effects as mentioned later, high solubility of pyridine is quite suitable for adsorption experiments in which the molecules remaining undissolved are unfavorable.

I expected that the molecules would be adsorbed with their plane parallel to the substrate surface. Because FePcCl does not have an active group such as carboxyl group used in fatty acid SAMs, molecule-substrae interaction is dominated by van der Waals force which is generally weak. However, large planar molecular structure tends to exhibit accumulated larger van der Waals force, where the energy/molecule can exceed even 1 eV [42], and then planer geometry with respect to the surface should be dominant to maximize van der Waals interaction [44]. In addition, molecule-molecule interaction, which is generally a problem in vapor phase deposition of phthalocyanines on oxide substrates, should be diminished in the liquid phase due to surrounding solvent molecules.

Subsequently to the preparation, I tried to estimate the orientation of adsorbed molecules in some of the samples by two measurements/analyses; polarized absorption spectroscopy and crystal truncation rod (CTR) analysis (the latter with collaborators).

In addition to the experiments, density functional theory (DFT) calculation was carried out to evaluate adsorption behavior from the view point of adsorption energies.

4.2 Experimental details

FePcCl (Sigma-Aldrich) was used without further purification. It was dissolved in pyridine (Wako Chemical) to certain concentration. In a part of the following experiments, pyridine was mixed with chloroform, tetrahyrofuran (THF), *N*-methylpyrrolidone (NMP), and *N,N*-dimethylformamide (DMF) (all from Wako Chemical), respectively, to be used as mixed solvents. Single crystalline perovskite oxide $SrTiO_3$(100) (Shinkosha Co., Ltd.) and $LaAlO_3$(100) (K-and-R Creation Co., Ltd.) were used as substrates. STO substrates had been treated by buffered hydrofluoric acid in advance by the supplier. Both one-side and both-side polished substrates were purchased, the latter of which was used for optical measurements. These substrates were immersed into solutions of iron phthalocyanine chloride (FePcCl). After immersion, the residual solution was removed by nitrogen gas blow and the substrates were dried in vacuum. The surface morphology of the annealed substrates was measured by AFM in contact mode using a cantilever with spring constant of 0.08 N/m. As for the immersed samples, AFM measurements were performed in tapping mode using cantilevers with spring constant of 28 or 3.5 N/m. The oscillation amplitude was restrained to prevent the molecular layer from the mechanical damage. Polarized absorption spectra in visible region were measured in air by a spectrophotometer system from JASCO with a polarizer for incident light and an attachment for reflection measurements. A homemade sample holder was used for transmission measurements.

4.3 Results and discussion

4.3.1 Preparation for oxide substrates with atomically flat step-terrace structure

To observe fine images of adsorbed phthalocyanine layer, it is important to obtain atomically flat surface of the oxide substrates. For satisfying the demand, annealing at high temperature is one of the most effective ways. As mentioned in the above experimental section, one-side or both-side polished substrates purchased from several suppliers were used. LAO and STO substrates were annealed in air at 1200 °C and 1050 °C, respectively, in an electric furnace, where the time for rising temperature was 2 h and that for keeping set-point temperature was also 2 h in both cases. AFM images of the oxide surface after annealing are shown in Figure 4.1.

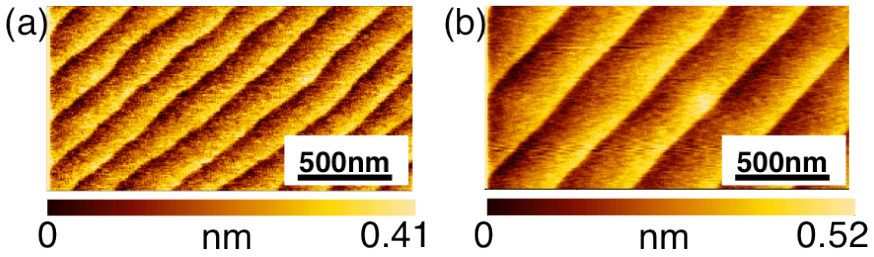

Figure 4.1 AFM images of (a) LAO and (b) STO substrates after annealing in air at high temperature.

It is noted that annealing at higher temperature may cause contamination of impurities on the oxide surface. Actually, XPS Fe 2*p* spectrum of LAO surface annealed at 1200 °C showed a peak attributed to oxidized iron (Figure 4.2). To prevent this problem, facing each surface of two substrates during annealing is effective (Figure 4.3). Moreover, as for LAO, this annealing procedure has tended to make step lines more straight, compared with the annealing of individual substrates.

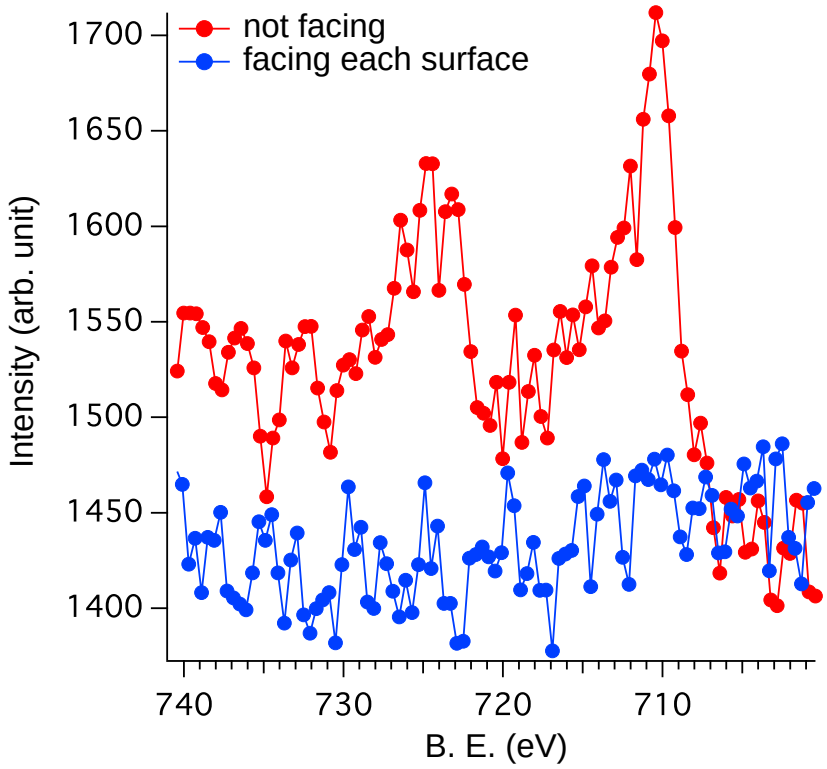

Figure 4.2 Fe 2*p* XPS spectra of LAO substrates. During annealing, (red) surface is not covered (blue) surfaces of the 2 substrates are faced each other.

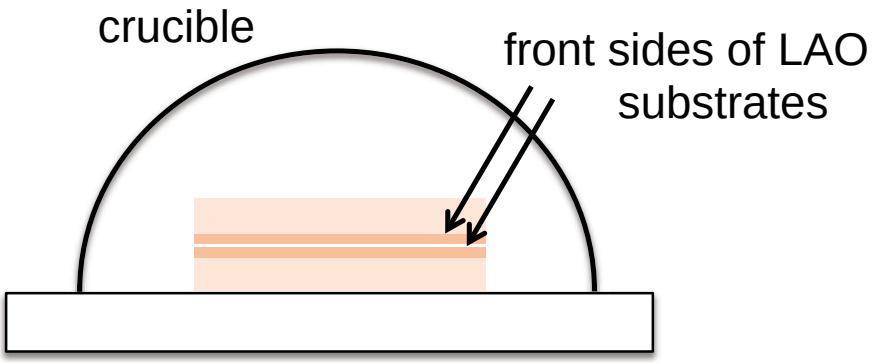

Figure 4.3 A schematic image of the substrates with their front-side surfaces faced during annealing.

4.3.2 Survey of immersion and surface observation

The obtained atomically flat substrates were exposed to UV-O_3 treatment, followed by immersion into FePcCl pyridine solution. Figure 4.4 shows visible light absorption

spectra of FePcCl pyridine solution. I measured several times to examine the stability of FePcCl in solution, several hours later after the first measurement. The observed absorption spectrum was almost unchanged regardless of waiting time. Thus the pyridine solution is durable for longer immersion time.

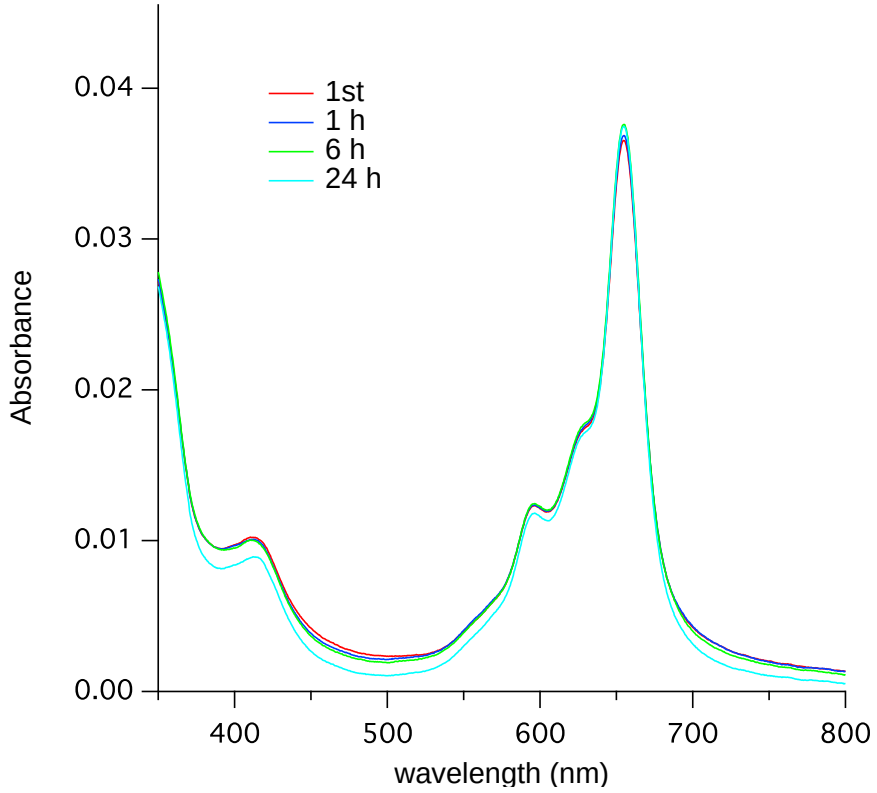

Figure 4.4 Visible light absorption spectra of FePcCl dissolved in pyridine with concentration of 6.31×10^{-7} M. After the first measurement (red line), the solution was measured again 1 h (blue), 6 h (green), and 24 h (sky blue) later.

LAO and STO substrates were investigated in several conditions. They were immersed into 0.2 mM solution for several hours. Figure 4.5 shows AFM images observed on the immersed substrates indicating small dots as adsorbates. LAO and STO substrates are also immersed in solution with series of different concentrations (Figure 4.6). Each series of AFM images on LAO or STO showed that apparent adsorption amounts increased along with solution concentration, although samples immersed into higher concentration solution may look very similar. (At least in the context of comparison

between the lowest concentration and highest concentration solutions.)

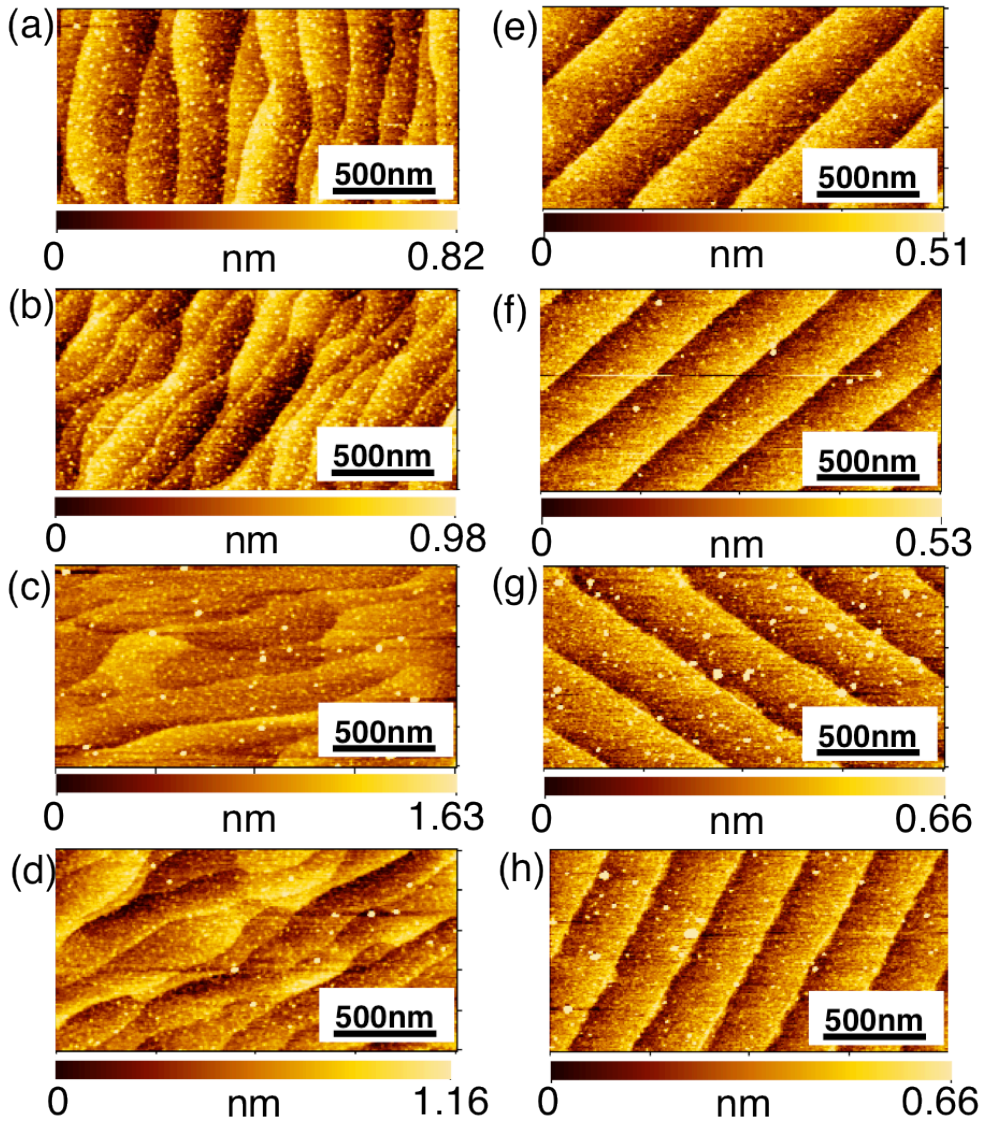

Figure 4.5 AFM images of (a)(b)(c)(d) LAO and (e)(f)(g)(h) STO substrates after immersion in 0.2 mM FePcCl pyridine solution for (a)(e) 1 h, (b)(f) 6 h, (c)(g) 12 h, and (d)(h) 24 h.

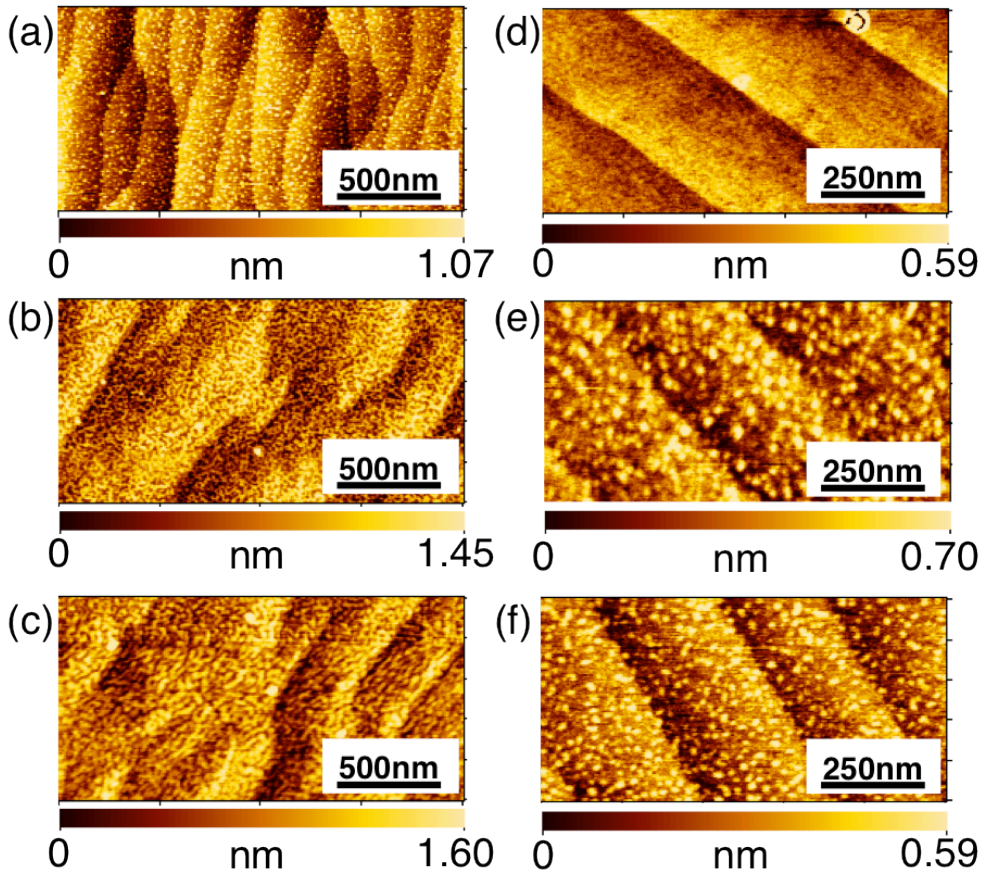

Figure 4.6 AFM images of (a)(b)(c) LAO and (d)(e)(f) STO substrates after immersion in FePcCl pyridine solution for 5 min. (a) 0.4 mM (b) 0.8 mM, (c) 1 mM, (d) 0.2 mM, (e) 0.4 mM, (f) 1 mM.

4.3.3 Further investigation on immersion method

According to the previous section, although it is subtle, appearances of the AFM images implied that STO surface was relatively tidy even after immersion especially when the concentration is low (see Figure 4.5, for example). For confirmation of this thing and further investigation, I prepared samples on LAO and STO substrates again by immersion in 0.3 mM solution (immersion time is 6 hours.). Herein, LAO substrates were superposed during annealing as mentioned above. Figure 4.7 shows representative surface morphology on LAO and STO. The figures indicate higher surface coverage on LAO. I estimated coverage of the two figures by binarization of color information and

counting pixels, resulting in 29% and 5%, respectively. This result implies difference in adsorption behavior between LAO and STO.

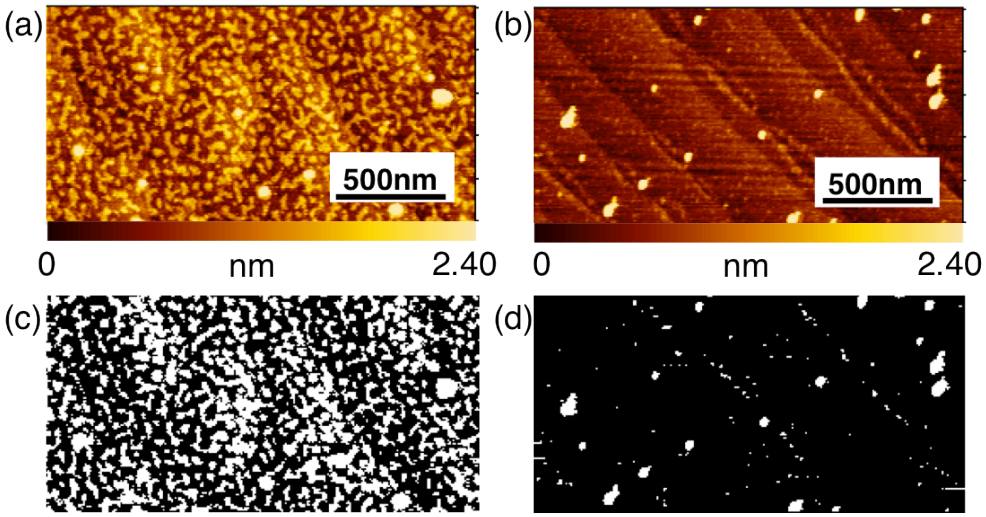

Figure 4.7 AFM images of (a) LAO and (b) STO substrates after immersion in 0.3 mM FePcCl pyridine solution for 6 h. (c) and (d) shows binarized images of (a) and (b), respectively.

Nevertheless, because the coverage values themselves were low, the appearance would vary depending on measured points and samples. As another method to compare surface of the two substrates, I measured XPS spectra. N 1*s* peak intensity at several points for several samples was investigated. Because phthalocyanine contains 8 nitrogen atoms per molecule, the adsorption amounts could be compared by XPS peak intensity. Representative XPS N 1*s* spectra and averaged peak intensity are shown in Figure 4.8, indicating that the adsorption amount is different from each other. Considering the result of AFM observation and XPS measurements, there is a possibility that FePcCl molecules have a tendency to be adsorbed on LAO substrate preferentially, compared with STO substrate.

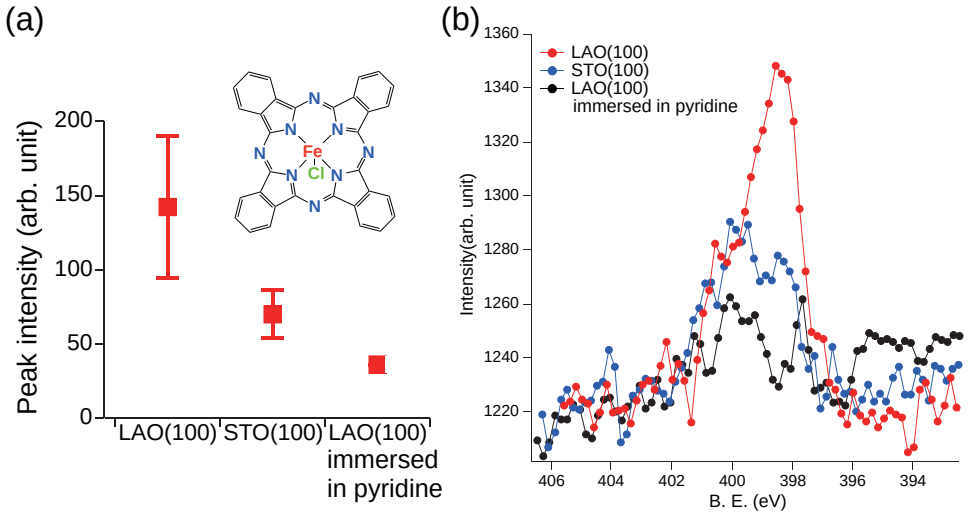

Figure 4.8 (a) Averaged XPS N 1*s* peak intensities of LAO and STO substrates immersed in 0.3 mM FePcCl pyridine solution, and LAO substrate immersed in pure pyridine. FePcCl structural formula is on together. (b) Representative XPS spectra for (a).

Such difference in molecular adsorption behavior on perovskite substrates was also reported in the literature mentioned in the introduction section, where stearic acid molecules were preferentially adsorbed on specific regions of STO(100) surface [109]. Although adsorption on different surface termination in a sample has not been discussed in detail in my study, ABO_3(100) substrates like LAO(100) and STO(100) should show different kinds of termination layer, AO and BO_2 layer, respectively, as mentioned later in the section about calculation. Figure 4.9 is a typical AFM image taken on a LAO sample. Several parts of the surface in the figure seems to show less amounts of adsorbate than the other parts. This subtle difference might originate from the difference in termination, as in the case of stearic acid example in the reference [109].

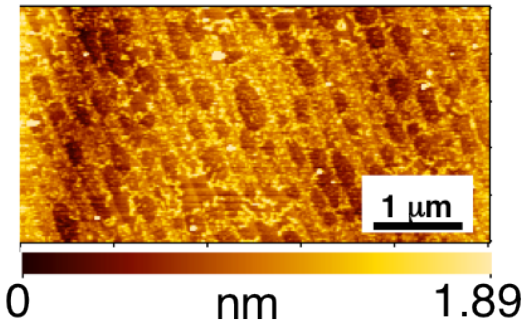

Figure 4.9 A representative AFM image of LAO substrate after immersion in 0.8 mM FePcCl pyridine solution for 6 h.

When the solution concentration was higher, the difference in adsorption behavior became unclear. Figure 4.10 shows AFM images of representative LAO and STO surface immersed in 0.8 mM solution. I measured XPS spectra at several points of the two samples, respectively, and Figure 4.11 represents their averaged N 1*s* peak intensity. It revealed that intensity on LAO is larger, but difference is much smaller, compared with the case of Figure 4.8.

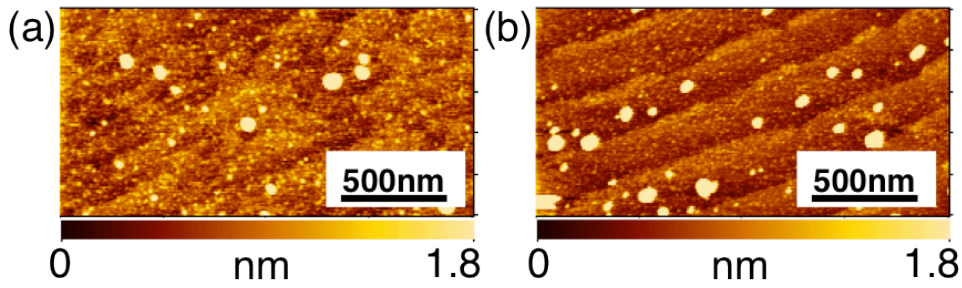

Figure 4.10 AFM images of (a) LAO and (b) STO substrates after immersion in 0.8 mM FePcCl pyridine solution for 6 h.

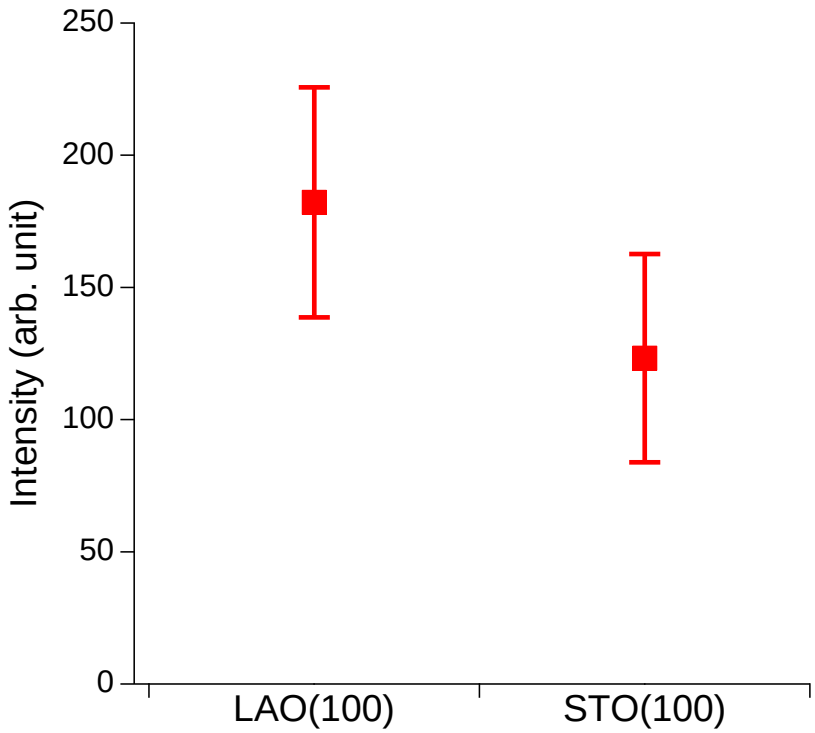

Figure 4.11 Averaged XPS N 1*s* peak intensities taken at several points of LAO and STO substrates shown in Figure 4.10.

Then I also investigate solvent effect on adsorption behavior. Some mixed solvents with pyridine were tried; chloroform, tetrahyrofuran (THF), *N*-methylpyrrolidone (NMP), and *N,N*-dimethylformamide (DMF). I focused on solvent polarity in this experiment. Looking at dipole moment of solvent molecules, those of chloroform and THF are smaller, and those of NMP and DMF are larger than those of pyridine, respectively. Generally, it is known that solvent polarity affects the formation of surfactant molecular SAMs [59]. Figure 4.12 shows AFM images of LAO substrates immersed in the 0.8 mM solutions with mixed solvents. Accordingly, the mixed solvents with low polarity and those with high polarity exhibited clearly different adsorption behavior; chloroform/pyridine and THF/pyridine mixed solvents showed greatly rough surface, while NMP/pyridine and DMF/pyridine mixed solvents showed less adsorption. Such difference in adsorption tendency depending on solvent polarity can be explained by the

affinity of solvent molecules to the oxide substrates and FePcCl solubility in the mixed solvents. I mean that solvents with higher polarity such as NMP and DMF may have better affinity to the oxide surface due to inherent polarity of oxides derived from ionic solid character, so that the solvent molecules prevent adsorption of the phthalocyanine because adsorption in liquid phase is a competitive phenomenon. On the other hand, solvents with lower polarity such as chloroform and THF may have worse affinity. Not only this tendency about affinity but also poorer solubility of the phthalocyanine in the mixed solvents than that in pure pyridine should contribute to larger adsorption amount.

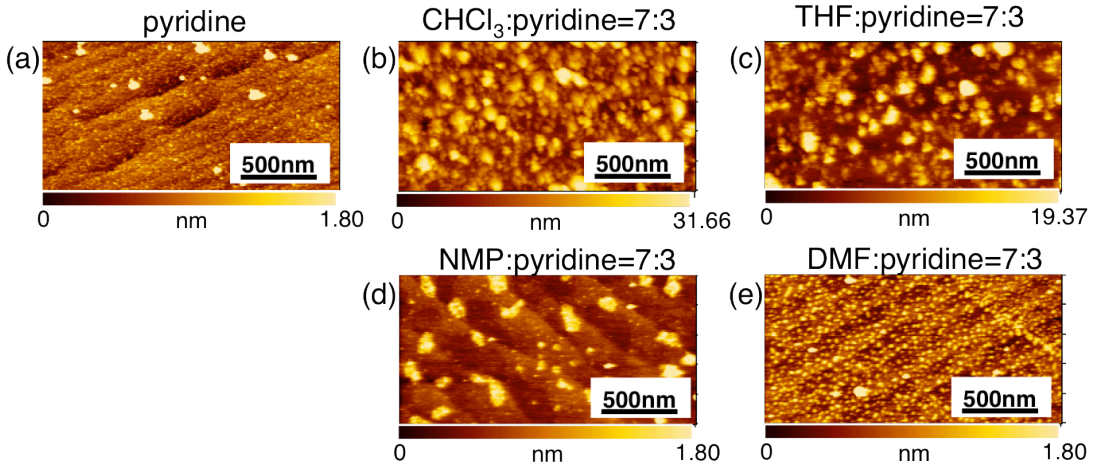

Figure 4.12 AFM images of LAO substrates after immersion in 0.8 mM FePcCl solutions dissolved in different solvents for 6 h. (a) pure pyridine and mixed solvents consisting of 30% pyridine and 70% (b) chloroform (c) THF (d) NMP (e) DMF.

From these experiments, it was shown that mixed solvents greatly influenced adsorption behavior. However, considering the balance of roughness, homogeneity, and adsorption amount, simple pyridine solution has been a choice so far. Thus, I continued to use pyridine solution in subsequent experiments.

4.3.4 Linear dichroic ratio

The molecular orientation of adsorbed ultrathin layer, particularly, whether the molecular plane is parallel to the substrate surface, is important information in my study.

To estimate the orientation, I measured polarized visible light absorption spectra at several incident angles for linear dichroic (LD) ratio. LD ratio is defined as the following equation [84];

$$\rho = \frac{\Delta T_{ms}}{\Delta T_{mp}} \ , \tag{4.1}$$

where ρ is LD ratio, $\Delta T_{ms,mp}$ is the fractional s- or p-polarized light power absorbed by a monolayer. Herein, to compensate reflected light effect, I measured reflectance as well as transmittance, and referred to an equation;

$$\Delta T_m = \Delta T T_0 + \Delta R R_0 \ , \tag{4.2}$$

where T_0 (R_0) is the transmittance (the reflectance) of a blank substrate, and ΔT (ΔR) is the ratio of the difference in the transmittance (the reflectance) between the blank and the sample with the monolayer against the blank transmittance (reflectance) [84]. Figure 4.13 illustrates the geometry absorption measurements.

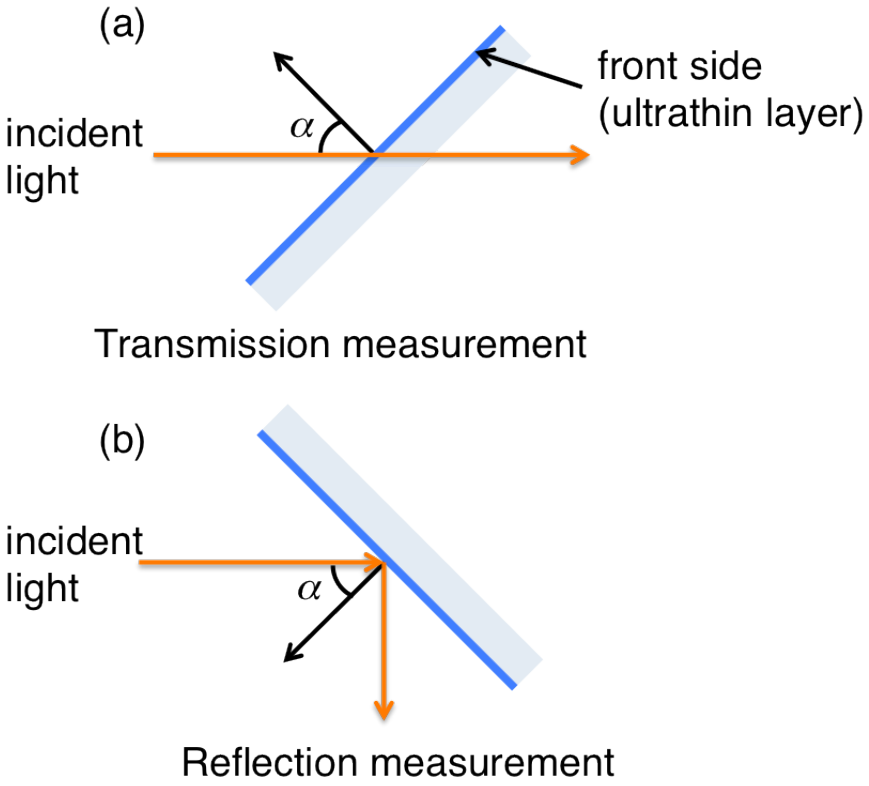

Figure 4.13 Schematic images of optical (a) transmission and (b) reflection measurement geometry.

In this study, I chose an ultrathinlayer on STO substrate as a target of this experiment because a high temperature annealed LAO substrate exhibited broadened absorption edge overlapping the visible Q-band of phthalocyanine. The sample was prepared by immersion of a both-side polished STO substrate annealed at 1050 °C into 0.8 mM pyridine solution of FePcCl.

Figure 4.14 shows transmission absorption ($-\log(1-\Delta T)$) and reflection absorption ($-\log(1-\Delta R)$) spectra. When ΔT and ΔR are enough small [84, 111], the LD ratio (Equation 4.1) is almost the same as the ratio between the left sides of Equation (4.2) for *p*- and *s*-polarized light, where the absorption band areas of Figure 4.14 are assigned to ΔT and ΔR instead.

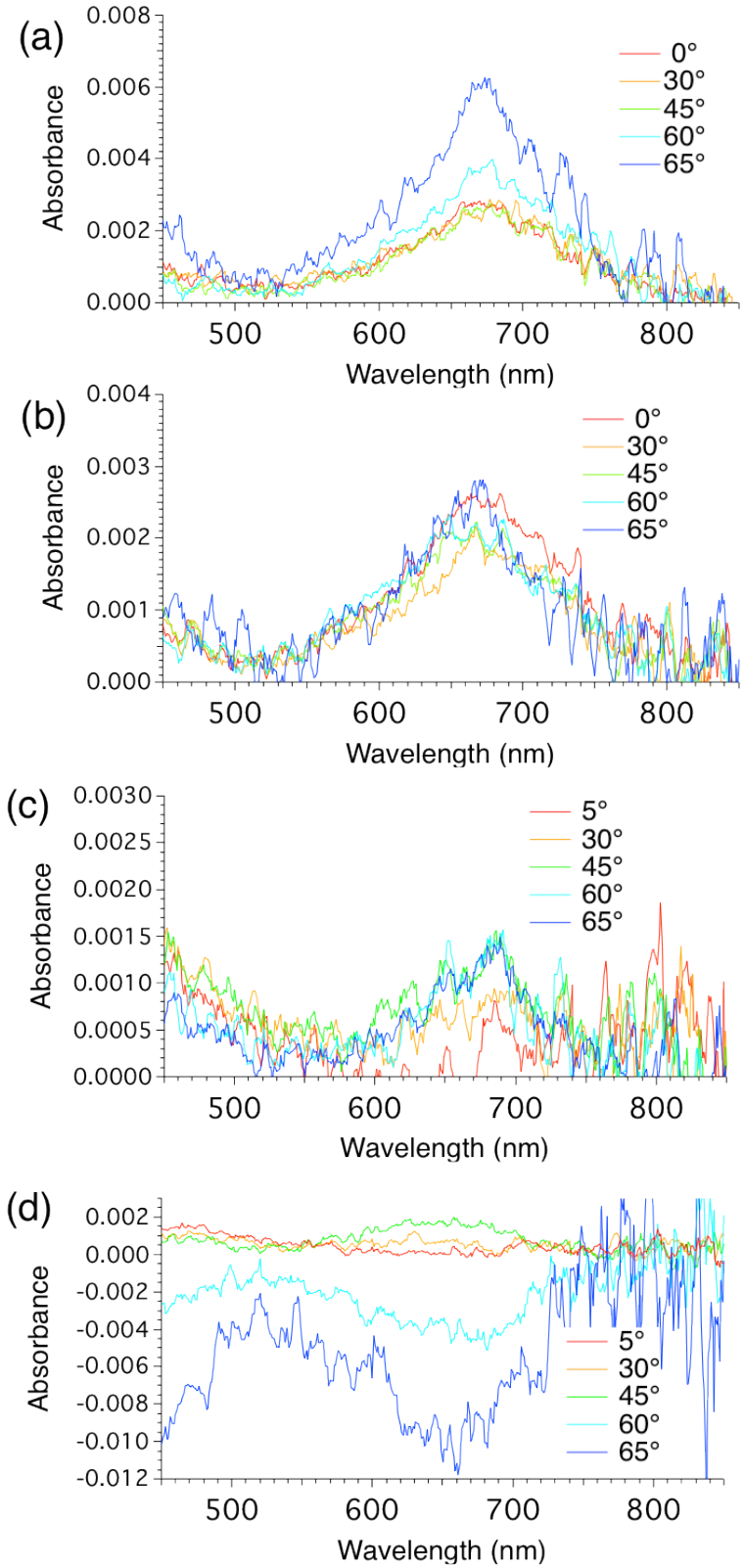

Figure 4.14 (a)(b) Transmission and (c)(d) reflection absorption spectra of FePcCl on STO substrate for (a)(c) *s*-polarized and (b)(d) *p*-polarized visible light at several incident angles.

From a theoretical aspect, assuming that an ultrathin layer is azimuthally isotropic, LD ratio can be expressed as [112];

$$\rho = \left(\cos^2 \alpha + \frac{2 \sin^2 \alpha \sin^2 \theta}{2 - \sin^2 \theta} \right)^{-1} , \tag{4.3}$$

using an incident angle α and an orientation angle θ, which is the angle between phthalocyanine plane normal and the substrate normal (Figure 4.15).

Figure 4.15 A schematic image for representing orientation angle θ. A green ellipse represents the phthalocyanine molecule.

Figure 4.16 shows LD ratio vs incident angle α plots including experimental data and theoretical curves for several orientation angles θ. Among the experimental plots, 6 points nearly fall on the curve assuming $\theta = 40^\circ$. Averaging the θ values estimated for these points provided $39 \pm 2^\circ$.

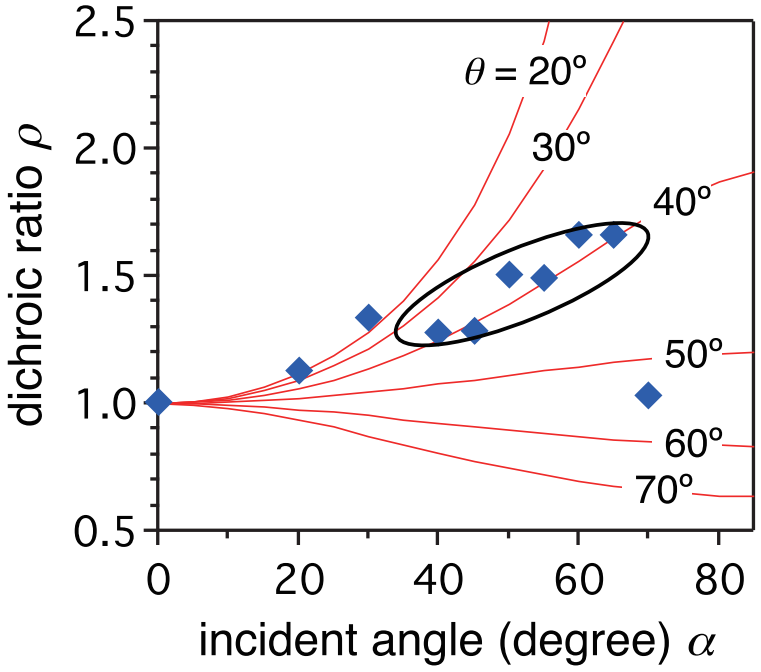

Figure 4.16 LD ratio as a function of incident angle for several θ. Experimental data (diamond) and theoretically simulated curve (solid curve).

Then, I compared the obtained value with information from AFM observation. Figure 4.17(a) shows an AFM image of the STO sample, from which I estimated height of the adsorbate to be about 7 Å. Besides, considering the size of the molecule (Figure 4.17(b), calculated in the subsequent section), the estimated inclination θ was about 21°, taking van der Waals radii into account. On the other hand, the height estimated from θ by LD ratio was about 10 Å. Such comparison seems to indicate overestimation of the LD ratio (or underestimation of the adsorbate height from AFM observation). However, consideration of these results suggests that molecular plane might be inclined towards surface plane, not in perfect horizontal geometry.

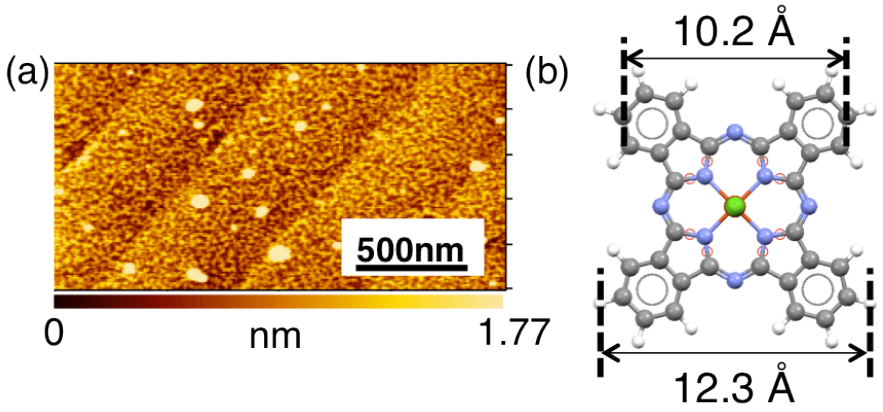

Figure 4.17 (a) AFM image of STO substrates after immersion in 0.8 mM FePcCl solutions for 6 h. (b) Optimized FePcCl model by DFT calculation (section 4.3.6) with molecular sizes.

4.3.5 Crystal truncation rod analysis

In this section, a result of crystal truncation rod (CTR) scattering measurement will be discussed. For this measurement, I prepared a LAO(100) sample immersed in 1.2 mM pyridine solution of FePcCl. Figure 4.18 shows the surface morphology of the sample.

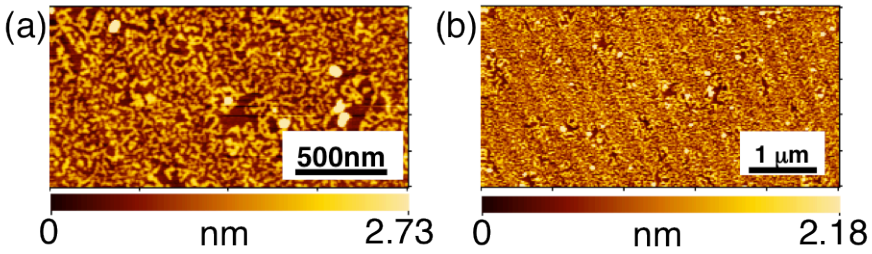

Figure 4.18 AFM images of LAO substrate used in CTR scattering measurement after immersion in 1.2 mM FePcCl solution for 6 h. (a) and (b) show different recorded scales.

The scattering measurement and subsequent analysis were performed based on crystal lattice of bulk LAO used as the substrate and along out-of-plane direction, that is, (00L) line in reciprocal space. The CTR scattering profile of a bare LAO sample along the (00L) line is shown in Figure 4.19.

At first, surface LAO structure was estimated so that the square of the structural

factor, $|F|^2$, calculated according to the equation in Chapter 2 could fit with the experimental profile (by collaborators). The calculated values derived from the surface structure along (00L) is also plotted in Figure 4.19.

The structural parameters such as out-of-plane displacement (dz) and occupancy of the surface atoms are summarized in Figure 4.20 and Figure 4.21, where it was assumed that the surface region corresponded to 4 unit cells. Assuming that the boundary at which occupancy goes across 0.5 is defined as the surface, LaO layer should be the surface layer of the LAO substrate.

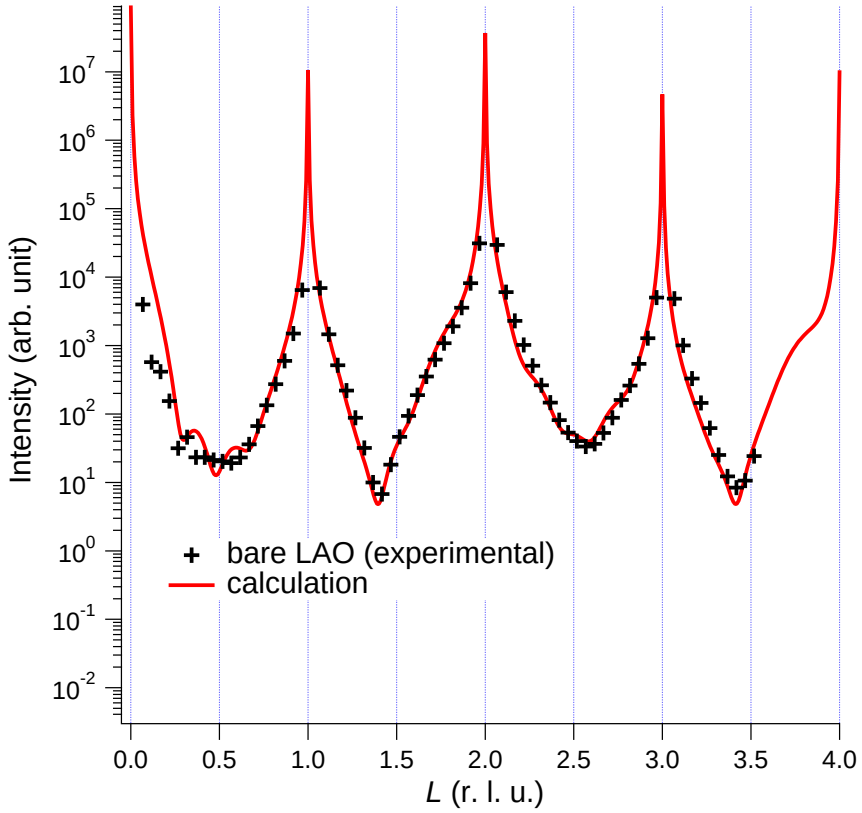

Figure 4.19 CTR scattering profile of a bare LAO sample (black cross) and $|F|^2$ calculated from optimized LAO surface structure model (Figure 4.20 and Figure 4.21) (red line) along the (00L) line. r.l.u. represents reciprocal lattice unit.

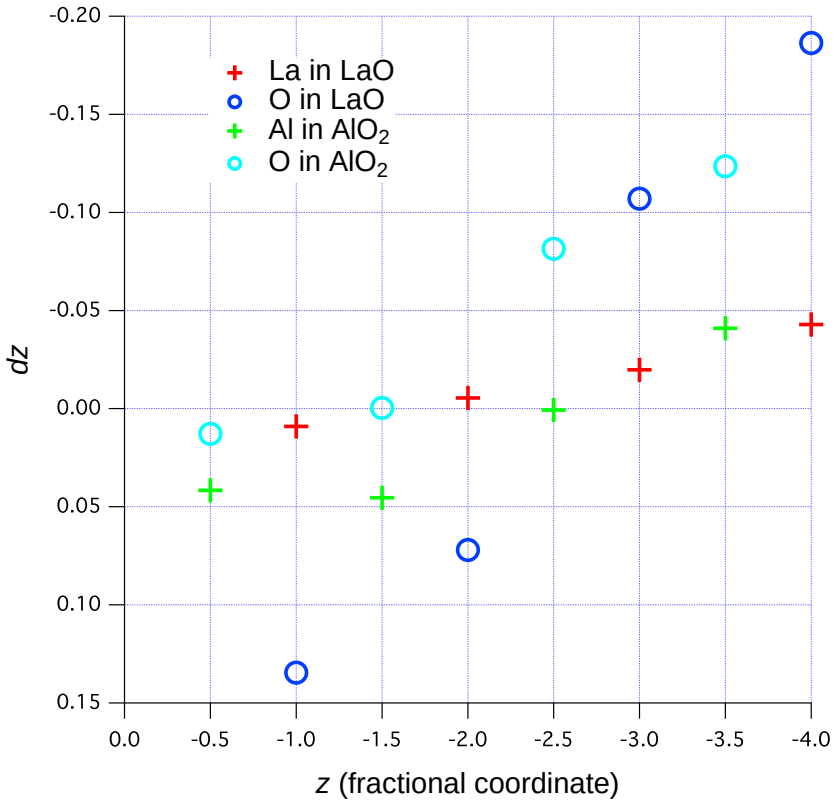

Figure 4.20 Displacement of atoms in LAO surface structure model optimized to fit with the experimental CTR scattering. The horizontal axis represents fractional coordinates of z direction which is perpendicular to the surface, where its unit equals to the lattice constant of bulk LAO (3.79 Å). Negative direction is pointing outwards from the surface. Assuming no displacement, each atom is at z represented by the value of horizontal axis. The vertical axis represents relative displacement dz from each z coordinate represented by horizontal axis.

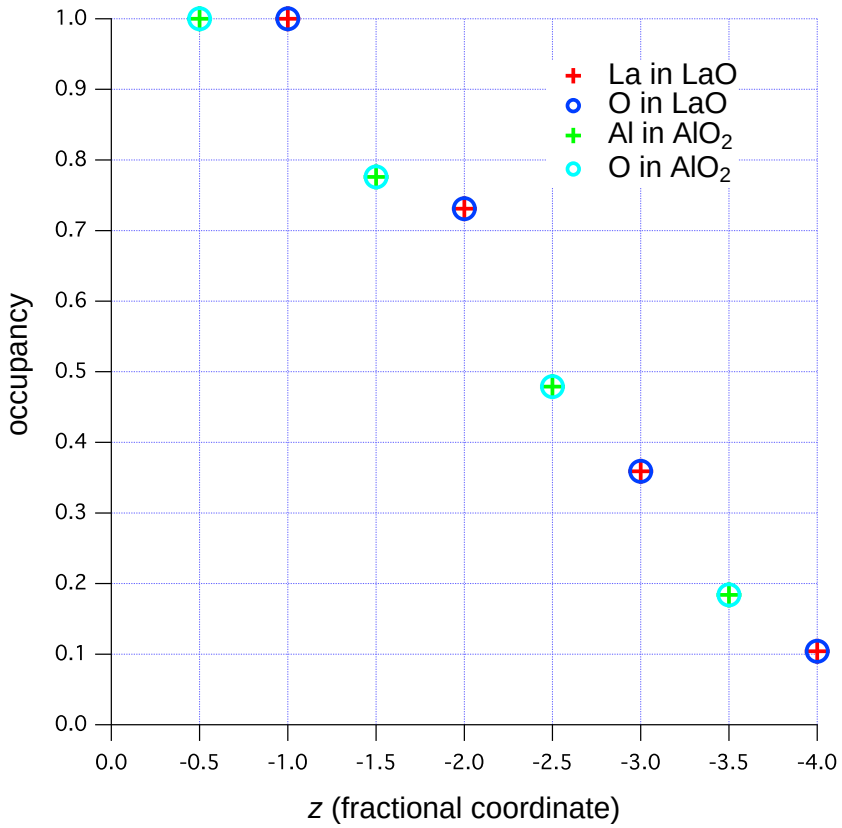

Figure 4.21 Occupancy of atoms in the LAO surface structure model shown in Figure 4.20, assuming that atoms at the same z when no displacement exists show the same occupancy.

To evaluate the phthalocyanine ultrathin layer on the LAO surface, normalization of the intensity from the sample by that from bare LAO would be one of the solutions to analyze a small change in the CTR scattering profiles originating from surface adsorption. Figure 4.22 shows normalized intensities. (CTR scattering measurements of the immersed LAO and bare LAO were performed twice, respectively, so that four normalized intensities are plotted, where each scattering intensity of the immersed LAO had been normalized by that of bare LAO.)

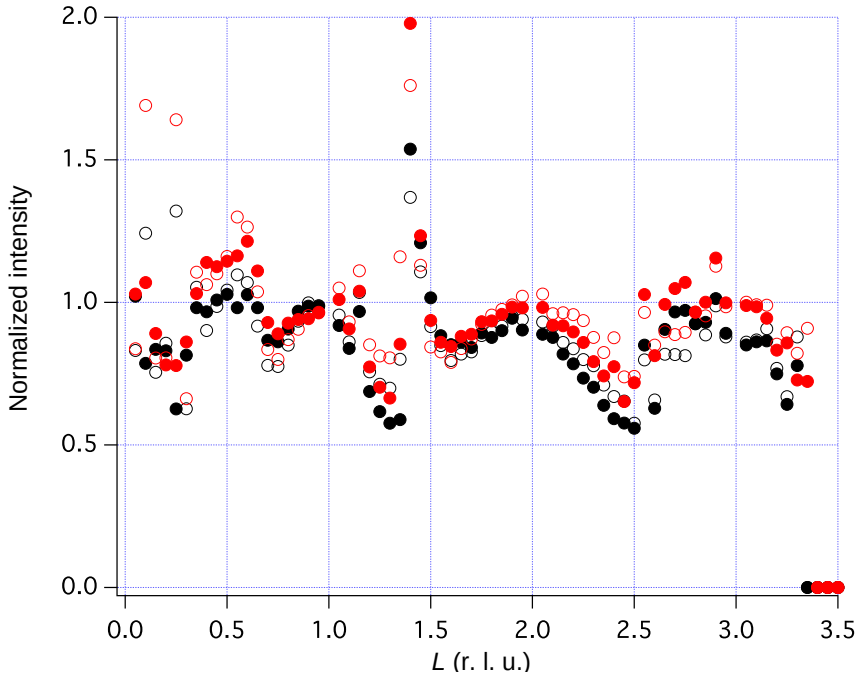

Figure 4.22 Normalized CTR scattering intensity of immersed LAO by that of bare LAO.

By comparing the above experimental normalized intensities with the calculated values from surface models with phthalocyanine on the LAO surface (in other words, the square of the structural factor, $|F|^2$, of the surface model with the adsorbed phthalocyanine normalized by that of the surface model without the phthalocyanine), the molecular orientation was estimated qualitatively.

At first, I show the normalized values calculated from the models using ideal flat surface, where LaO layer surface-terminated surface was assumed. A schematic image of the calculated model is shown in Figure 4.23 and calculated results are summarized in Figure 4.24. As the phthalocyanine molecular plane is tilting, the plots appears to be complicated, compared with experimental ones (Figure 4.22). By changing the distance between the surface and the molecule with the molecular plane parallel, I found that the calculated plot of the model assuming the distance of 3.6 Å well reproduces the experimental results.

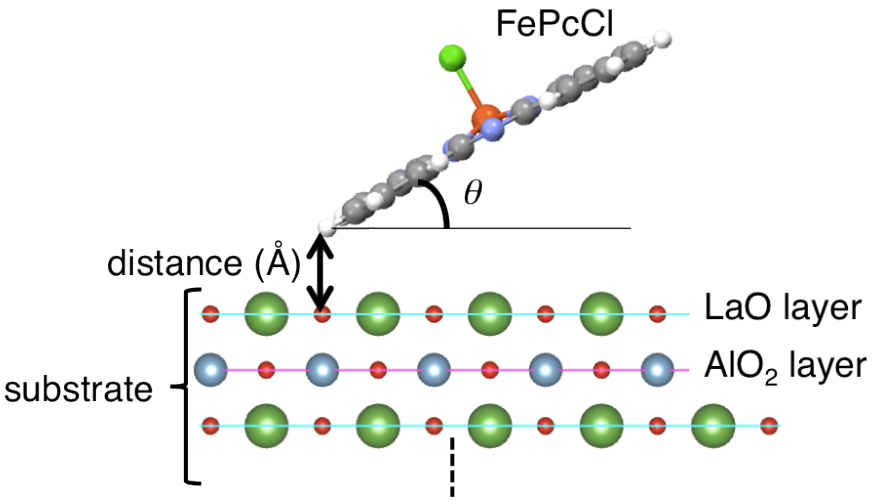

Figure 4.23 A schematic image of the surface and molecule model used for calculation of $|F|^2$ along the $(00L)$ line. Several angles θ and distance were tried for calculation.

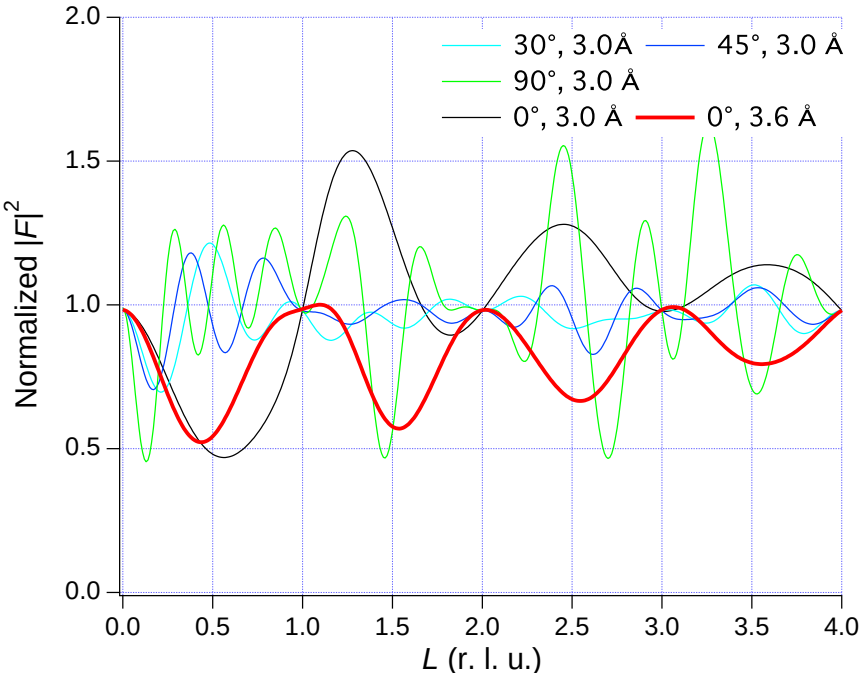

Figure 4.24 Normalized $|F|^2$ calculated from several models as shown in Figure 4.23 by that calculated from a model without the molecule.

Then, normalized $|F|^2$ of the models with the adsorbed phthalocyanine which takes into account the optimized LAO surface structure mentioned above were calculated and compared. In those models, occupancy of the phthalocyanine was adjusted to that of

LaO layer in the surface model (Figure 4.22). As shown in Figure 4.25, the normalized plot of the model in which the phthalocyanine in parallel geometry is away from LaO layer ($dz = 0$) by 3.6 Å seems consistent with the experimental plots to some extent. Another plot represents a model in which molecular occupancy is modified with the same arrangement of the molecule, showing much more similarity to the experimental plots. Normalized $|F|^2$ of other models with tilted phthalocyanine were also calculated. However, they were less consistent with the experimental plots as in the case of the ideal flat LAO surface.

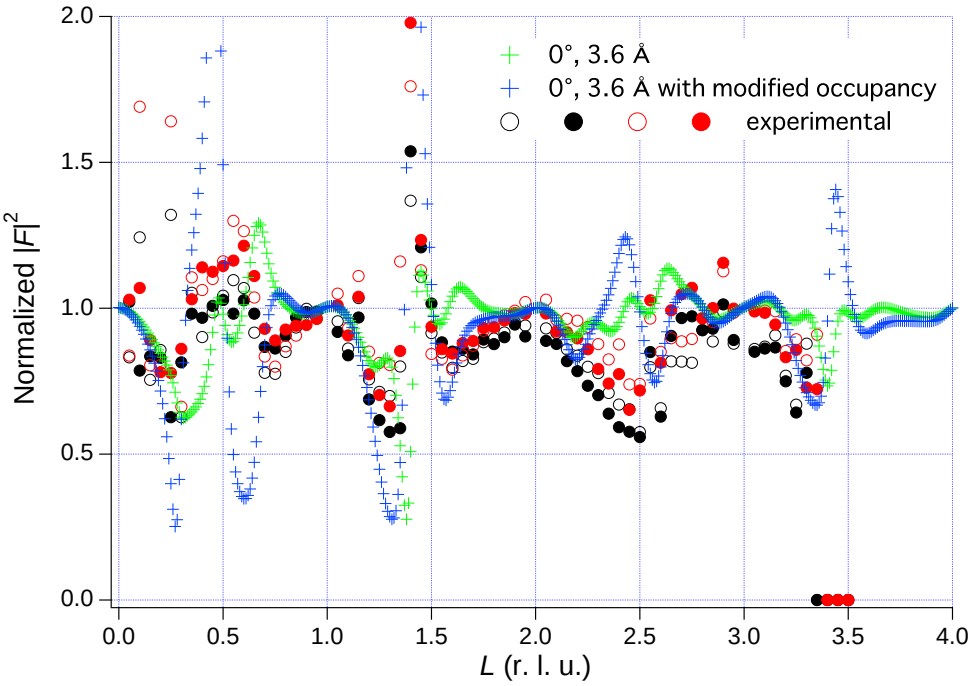

Figure 4.25 Normalized $|F|^2$ calculated from two models, where the flat lying molecule is on the optimized LAO surface structure. Normalized experimental plots are also shown together.

By comparing the experimental plots with those calculated from the several models, I found, even qualitatively, that orientation of the adsorbed phthalocyanine molecules on the LAO substrate seems close parallel to the surface.

4.3.6 Calculation of adsorption energy

Before DFT calculation, I will explain a possible reason for difference in adsorption behavior mentioned in the above subsection. For such purpose, surface structure of perovskite oxide substrate should be noted. Perovskite oxide ABO_3 with (100) plane is known to be regarded as alterate stacking of AO and BO_2 layers as shown in Figure 4.26, and thus there are two possibilities for surface termination, AO-termination or BO_2-termination. Turning to LAO and STO (100) which I used, it has been reported that LAO and STO show LaO (as AO) and TiO_2 (as BO_2) termination, respectively [113, 114]. Thus, I wondered if difference in surface termination would be a possible reason that FePcCl showed preferential adsorption on LAO substrates. To discuss and support this possibility, I conducted DFT calculation about this surface molecular adsorption model.

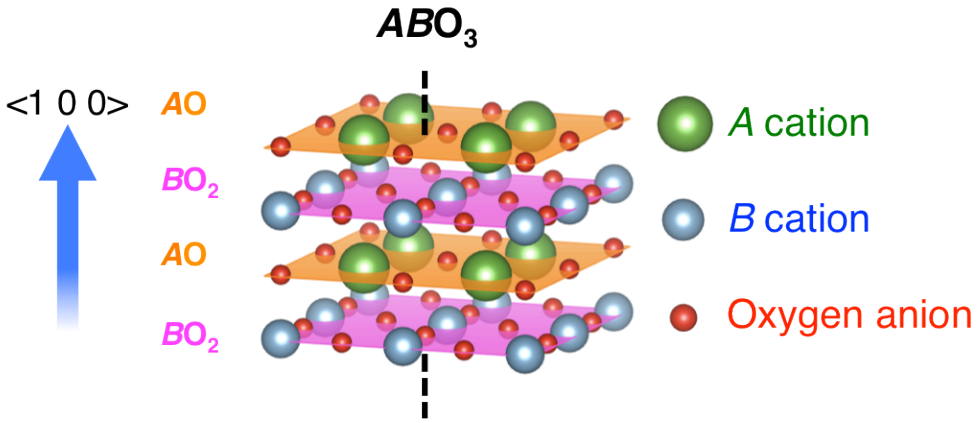

Figure 4.26 A schematic image of perovskite oxide ABO_3 crystal structure, which is regarded as repetitive AO and BO_2 layers along <100> direction.

At first, I attempted to construct and optimize surface structure of each perovskite oxide by DFT calculation using VASP package. LAO and STO in cubic structure were relaxed to obtain optimized lattice constant, where cell size was unfixed. The lattice constants of LAO and STO were converged to be 3.81 Å and 3.95 Å, respectively.

Then, to express perovskite oxide surface, freestanding LAO and STO (100) slabs

were considered (Figure 4.27). Thickness of the slabs corresponded to 5.5-unit-cell(u.c.)-thick having LaO (for LAO) and TiO_2 (for STO) surfaces at both sides of the slabs, respectively. These symmetric slabs were suitable when the structures were relaxed to be optimized because of inner dipole counter. The basis of slabs were constructed as follows; 6 u.c. were accumulated vertically with 5-Å-thick vacuum regions over both sides of the slab to be simulation cells, followed by elimination of outermost AlO_2 (for LAO slab) and SrO (for STO slab), respectively, resulting in symmetric 5.5-u.c.-thick slabs. As a result, the slabs could express LaO and TiO_2 surface. The cell size parallel to the surface was 1 x 1. These slab models were then relaxed with fixed simulation cell size to obtain surface structures used for molecular adsorption models.

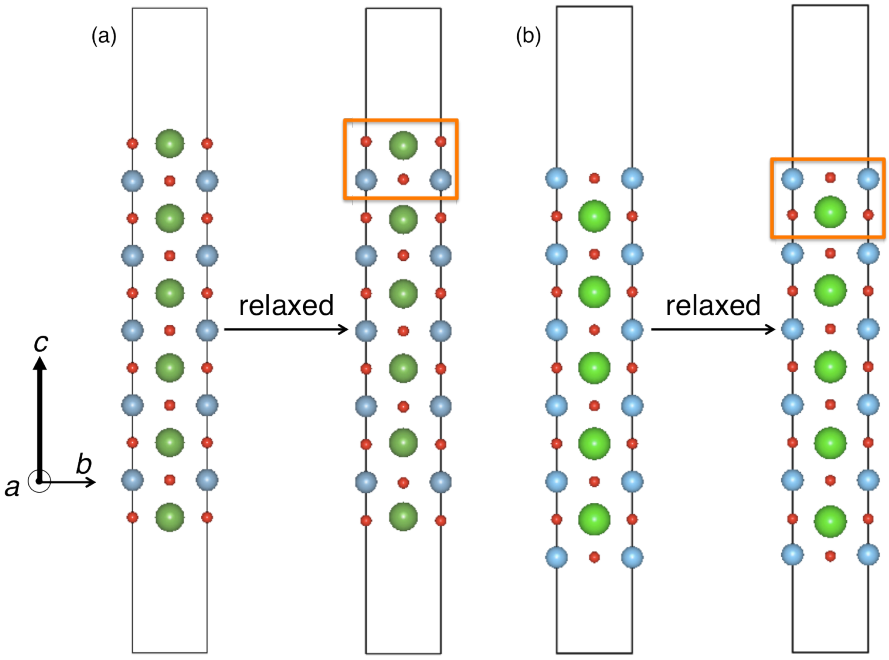

Figure 4.27 (a) LAO and (b) STO slab models before and after relaxation. The parts of the slabs surrounded by orange rectangles were picked and applied for adsorption model (Figure 4.28).

Due to limitation of calculation cost, I picked up outermost 1-u.c.-thick parts from calculated slabs as substrates for adsorption models (Figure 4.27). I expanded the 1-u.c.-thick slabs to 5 x 5 cell size for *ab* plane of simulation cell considering the size of the

FePcCl molecule. The individual FePcCl molecular structure was optimized in advance by Gaussian09 package (Chapter 2).

An adsorption model was constructed by arranging the FePcCl molecule on the 5 x 5 LaO or TiO_2 substrate with the molecular plane parallel to the surface, some distance (Å) away from the outer oxygen atoms (Figure 4.28).

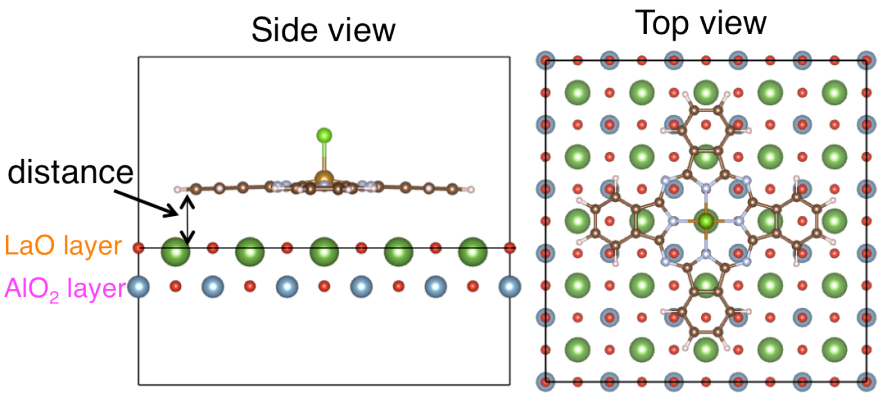

Figure 4.28 Side and top views of a representative adsorption model of FePcCl on LaO surface.

Total energy of each model was calculated by DFT-D2 method [98, 115] (experimental section, Chapter2) including van der Waals energy contribution, without relaxation of the structure. Adsorption energy E_{ads} was estimated using the following equation [116];

$$E_{ads} = E_{slab/FePcCl} - E_{slab} - E_{FePcCl} \quad , \tag{4.4}$$

where $E_{slab/FePcCl}$, E_{slab}, and E_{FePcCl} are the total energies of adsorption model, isolated substrate model, and isolated molecular model, respectively, which were calculated under the same condition.

To compare adsorption energies of LAO and STO models, I searched for the most stable positions of the FePcCl molecule. At first, fixing the molecule-substrate distance, several positions and rotation angles of the FePcCl against the substrate were tried. Con-

sidering both perovskite oxide (100) surface and FePcCl molecule have C_{4v} symmetry, position 1, 2, and 3, where Fe atom in FePcCl is over the positions, and 0° and 45° rotations were tried to estimate the adsorption energies here (Figure 4.29). As a result, position 1 with 45° rotation and position 1 with 0° were found to be the most stable arrangements for LAO and STO, respectively. Finally, the molecule-substrate distance was optimized.

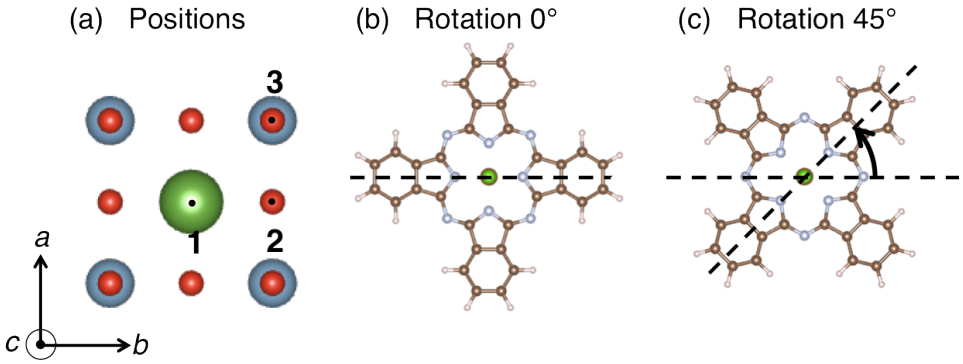

Figure 4.29 (a) Top view of a 1-u.c. part of the LAO slab with position 1, 2, and 3 mentioned in the text. (b)(c) Top views of FePcCls rotated by 0° and 45° with respect to the calculation cell.

The obtained adsorption energies were summarized in Table 4.1 with the molecule-substrate distance. In addition to the adsorption energies on LaO and TiO_2 surface, those on AlO_2 and SrO surface at the same molecular position were also calculated and listed. Comparing these adsorption energies with previously reported values of phthalocyanines on other inorganic surfaces, it can be said that they are reasonable, where -5.7 eV (without van der Waals, -0.9 eV) of ZnPc on ZnO [117] and -5.9 eV (without van der Waals, -0.32 eV) of MnPc on Cu [118] were calculated.

Looking at the total adsorption energies on LaO surface of LAO (100) and TiO_2 surface of STO (100) in Table 4.1, the former value was found to be larger than the latter value by about 3 eV, being consistent with experimental results.

For further discussion, I separated adsorption energy into two contributions, van der Waals interaction and others. Looking at the right columns of Table 4.1, it is found that the contribution of van der Waals interaction dominates E_{ads} in any case of the calculation. However, it is noted that such adsorption energy by DFT-D2 is likely to be overestimated [117]. This seems especially for the case of LaO surface because some parameters of La used for DFT-D2 were determined by myself (Chapter 2). Thus, the difference in E_{ads} should be attributed to the other dominant contribution. Actually, while E_{ads} without van der Waals contribution on LaO gives a negative value, that on TiO_2 shows a positive value. As for other surfaces, AlO_2 and SrO show positive and negative values, respectively. After all, considering such results summarized in Table 4.1, I expected that the difference in E_{ads} originates from surface termination, *i.e.*, whether the surface is AO layer or BO_2 layer, which may lead to different adsorption behavior as observed in my study.

Finally, I calculated the charge per molecule which belongs to adsorbed FePcCl after E_{ads} calculation by summing up charges of atoms in the molecule, which was assigned to each atom by Bader's charge analysis based on the charge density of the system [119]. As a result, I found clear difference between LaO and TiO_2 surface: FePcCl on LaO has a charge of -1.23/molecule and FePcCl on TiO_2 has -0.0833/molecule, which should be related to the difference in adsorption energy in this calculated system. Although such a strong charge transfer on LaO is not realistic, charge density distribution in a space between the surface and FePcCl should be significantly different. Thus, some electronic interactions between molecules and substrate surface may be expected to exist to some extent in practical cases, which might result in the preferable adsorption on LAO.

Table 4.1 Adsorption energies of FePcCl on different four surfaces

Surface (distance (Å))	E_{ads} (eV)	E_{ads} (w/o vdW) (eV)	E_{ads} (vdW) (eV)
LaO of LAO (2.8)	−5.68	−0.93	−4.75
AlO_2 of LAO (2.9)	−2.80	0.86	−3.66
SrO of STO (2.7)	−3.83	−0.19	−3.64
TiO_2 of STO (2.9)	−2.51	0.67	−3.18

4.4 Summary

In this chapter, I prepared phthalocyanine ultrathin layers on LAO(100) and STO(100) by immersion method. On formation of the ultrathin layers, it was found that FePcCl tended to show preferential adsorption on LAO to adsorption on STO especially in lower solution concentration, which was observed by AFM and XPS measurements. Moreover, a solvent effect on adsorption was confirmed that NMP and DMF suppressed the adsorption of the solute while THF and chloroform enhanced it too much. These results might come from the difference in solvent polarity.

The molecular orientation on the substrates was estimated by polarized absorption measurement and CTR scattering analysis. The former performed on the STO sample indicated an orientation angle of 39°. The latter using LAO sample manifested planar geometry of FePcCl with respect to the LAO substrate surface. These results suggested that the phthalocyanine molecules were adsorbed with the molecular plane inclined towards the surface and they are not in “edge-on” geometry.

Finally DFT calculations were performed for the adsorption energies to discuss the

possibility that difference in the perovskite oxide surface structures influences molecular adsorption. As a result of calculation, it was shown that adsorption energy on AO surface is larger than that on BO_2 surface, suggesting that difference in surface termination of perovskite oxides might contribute to the preferential adsorption.

Chapter 5

General conclusion

In this dissertation, phthalocyanine ultrathin layers were prepared by two wet processes; LB method in Chapter3 and immersion method in Chapter4. Then, discussion on molecular orientation in the ultrathin layers was noted.

In Chapter3 for LB method, LB monolayers of *M*OOPcs and CuTTBPc were fabricated at 3 or 20 mN/m surface pressure on glass substrates. The experimental results showed CuTTBPc with rigid structure had edge-on like orientation. On the other hand, *M*OOPcs took inclined orientation due to the alkyl chains. As for *M*OOPcs, effects of different central metals were also suggested. At the surface pressure of 3 mN/m, π-*A* curves shows larger area per molecule of ZnOOPc, indicating that its molecular plane was tilting towards the surface more than CuOOPc. At the higher surface pressure of 20 mN/m, in contrast, ZnOOPc showed further compression when the surface pressure was kept constant. Cu and Zn difference has also an effect on the vertical transfer of Langmuir monolayers. UV-vis spectra and XRR analyses supported and contributed to the estimation of transferred monolayers. The difference should be attributed to the hydrophilicity of the central metals.

In Chapter4 for immersion method, FePcCl ultrathin layers were prepared on LAO(100) and STO(100) substrates by immersing them into the phthalocyanine pyridine solutions.

From AFM and XPS measurements, it was shown that the molecules were likely to be adsorbed on LAO preferentially to STO. The possible reason of different adsorption behavior was discussed based on DFT calculation. As a result, it was revealed that difference in surface termination structure of perovskite oxide substrate (100) had an large influence on adsorption energy. Indeed, LaO surface of LAO(100) showed larger adsorption energy for FePcCl than TiO_2 on STO. Molecular orientation of FePcCl on the substrates was investigated by polarized absorption spectroscopy and CTR scattering analysis. The obtained results suggested that FePcCl on LAO and STO was close to flat geometry, at least, not close to perpendicular geometry.

In conclusion, phthalocyanine ultrathin layers were formed on inorganic solids by wet processes. Throughout this study, it was revealed that interaction between the molecules and the scaffold, which was herein water subphase or perovskite oxide substrate, can be a key factor for formation of the ultrathin layers by wet process.

This study would contribute to controllable formation of ultrathin organic layers on oxides such as perovskite materials [109]. Recent progress in oxide fabrication techniques enabled us to control surface termination [120]. Collaborated with such techniques, novel functionalities such as inorganic surface-molecule magnetic interaction [24] can be explored by using feasible wet process.

References

[1] D. J. Frank, R. H. Dennard, E. Nowak, P. M. Solomon, Y. Taur, H. S. P. Wong, *Proceedings of the IEEE* **89**, 259 (2001).

[2] A. Goetzberger, C. Hebling, H.-W. Schock, *Materials Science and Engineering: R: Reports* **40**, 1 (2003).

[3] S. Nakamura, M. Senoh, N. Iwasa, S. Nagahama, T. Yamada, T. Mukai, *Japanese Journal of Applied Physics* **34**, L1332 (1995).

[4] A. Dodabalapur, L. Torsi, H. E. Katz, *Science* **268**, 270 (1995).

[5] A. Facchetti, *Materials Today* **10**, 28 (2007).

[6] L. Hung, C. Chen, *Materials Science and Engineering: R: Reports* **39**, 143 (2002).

[7] B. W. D'Andrade, M. E. Thompson, S. R. Forrest, *Advanced Materials* **14**, 147 (2002).

[8] E. Bundgaard, F. C. Krebs, *Solar Energy Materials and Solar Cells* **91**, 954 (2007).

[9] B. A. Gregg, M. C. Hanna, *Journal of Applied Physics* **93**, 3605 (2003).

[10] Y. Matsuo, Y. Sato, T. Niinomi, I. Soga, H. Tanaka, E. Nakamura, *Journal of the American Chemical Society* **131**, 16048 (2009).

[11] T. Kuwabara, T. Nakayama, K. Uozumi, T. Yamaguchi, K. Takahashi, *Solar Energy Materials and Solar Cells* **92**, 1476 (2008).

[12] M. Nakano, T. Makino, A. Tsukazaki, K. Ueno, A. Ohtomo, T. Fukumura, H. Yuji, S. Akasaka, K. Tamura, K. Nakahara, T. Tanabe, A. Kamisawa, M. Kawasaki, *Applied Physics Letters* **93**, 1 (2008).

[13] J. Y. Lee, S. Roth, Y. W. Park, *Applied Physics Letters* **88**, 252106 (2006).

[14] K. Itaka, M. Yamashiro, J. Yamaguchi, M. Haemori, S. Yaginuma, Y. Matsumoto, M. Kondo, H. Koinuma, *Advanced Materials* **18**, 1713 (2006).

[15] S. Singha Roy, D. J. Bindl, M. S. Arnold, *The Journal of Physical Chemistry Letters* **3**, 873 (2012).

[16] B.-w. Park, Q. Shen, Y. Ogomi, S. S. Pandey, T. Toyoda, S. Hayase, *ECS Journal of Solid State Science and Technology* **2**, Q6 (2012).

[17] B. W. Park, T. Inoue, Y. Ogomi, A. Miyamoto, S. Fujita, S. S. Pandey, S. Hayase, *Applied Physics Express* **4**, 10 (2011).

[18] H. Imahori, T. Umeyama, K. Kurotobi, Y. Takano, *Chemical Communications* **48**, 4032 (2012).

[19] F. Matemadombo, T. Nyokong, *Electrochimica Acta* **52**, 6856 (2007).

[20] K. I. Ozoemena, T. Nyokong, *Electrochimica Acta* **51**, 2669 (2006).

[21] H. Wende, M. Bernien, J. Luo, C. Sorg, N. Ponpandian, J. Kurde, J. Miguel, M. Piantek, X. Xu, P. H. Eckhold, W. Kuch, K. Baberschke, P. M. Panchmatia, B. Sanyal, P. M. Oppeneer, O. Eriksson **6**, 2 (2007).

[22] C. Wäckerlin, D. Chylarecka, A. Kleibert, K. Müller, C. Iacovita, F. Nolting, T. A. Jung, N. Ballav, *Nature communications* **1**, 61 (2010).

[23] M. Gruber, *et al.*, *Nature Materials* **14**, 981 (2015).

[24] N. Ballav, C. Wackerlin, *The Journal of Physical Chemistry Letters* **4**, 2303 (2013).

[25] C. Wäckerlin, K. Tarafder, D. Siewert, J. Girovsky, T. Hählen, C. Iacovita, A. Kleibert, F. Nolting, T. A. Jung, P. M. Oppeneer, N. Ballav, *Chemical Science* **3**, 3154 (2012).

[26] H. Ishii, K. Sugiyama, E. Ito, K. Seki, B. H. Ishii, *Advanced Materials* **11**, 605 (1999).

[27] P. Wu, Q. Zeng, S. Xu, C. Wang, S. Yin, C. L. Bai, *Chemphyschem : a European journal of chemical physics and physical chemistry* **2**, 750 (2001).

[28] K. Suto, S. Yoshimoto, K. Itaya, *Journal of American Chemical Society* **125**, 14976 (2003).

[29] Y. Wei, S. W. Robey, J. E. Reutt-Robey, *Journal of Physical Chemistry C* **112**, 18537 (2008).

[30] C. M. Crudden, J. H. Horton, I. I. Ebralidze, O. V. Zenkina, A. B. McLean, B. Drevniok, Z. She, H.-B. Kraatz, N. J. Mosey, T. Seki, E. C. Keske, J. D. Leake, A. Rousina-Webb, G. Wu, *Nature chemistry* **6**, 409 (2014).

[31] D. Zhang, T. Yoshida, H. Minoura, *Advanced Materials* **15**, 814 (2003).

[32] H. Ohta, T. Kambayashi, K. Nomura, M. Hirano, K. Ishikawa, H. Takezoe, H. Hosono, *Advanced Materials* **16**, 312 (2004).

[33] Y. Furubayashi, T. Hitosugi, Y. Yamamoto, K. Inaba, G. Kinoda, Y. Hirose, T. Shimada, T. Hasegawa, *Applied Physics Letters* **86**, 252101 (2005).

[34] G. Arlt, D. Hennings, G. De With, *Journal of Applied Physics* **58**, 1619 (1985).

[35] T. Takaaki, ペロブスカイト関連化合物 機能の宝庫 (学会出版センター, 1997), chap. 強誘電性, pp. 84–94.

[36] J.-H. Park, E. Vescovo, H. Kim, C. Kwon, *Nature* **392**, 794 (1998).

[37] M. Bowen, M. Bibes, a. Barthélémy, J. P. Contour, a. Anane, Y. Lemaître, a. Fert, *Applied Physics Letters* **82**, 233 (2003).

[38] Z. H. Xiong, D. Wu, Z. V. Vardeny, J. Shi, *Nature* **427**, 821 (2004).

[39] S. Tatay, C. Barraud, M. Galbiati, P. Seneor, R. Mattana, K. Bouzehouane, C. Deranlot, E. Jacquet, A. Forment-Aliaga, P. Jegou, A. Fert, F. Petroff, *ACS Nano* **6**, 8753 (2012).

[40] T. D. Nguyen, E. Ehrenfreund, Z. V. Vardeny, *Science* **337**, 204 (2012).

[41] Y. G. Park, H. Y. Lee, H. Tanaka, H. Tabata, T. Kawai, *Applied Physics Letters* **81**, 1318 (2002).

[42] S. Forrest, *Chemical Reviews* **97**, 1793 (1997).

[43] F. Schreiber, *Physica Status Solidi (a)* **201**, 1037 (2004).

[44] G. Witte, C. Wöll, *Journal of Materials Research* **19**, 1889 (2004).

[45] L. Triguero, A. Fo, P. Va, M. Weinelt, L. G. M. Pettersson, Y. Luo, A. Hans, *Journal of the American Chemical Society* **122**, 12310 (2000).

[46] H. Ohta, T. Kambayashi, M. Hirano, H. Hoshi, K. Ishikawa, H. Takezoe, H. Hosono, *Advanced Materials* **15**, 1258 (2003).

[47] D. R. Talham, *Chem. Rev.* **104**, 5479 (2004).

[48] M. Chikazawa, K. Tajima, 界面化学 (丸善出版, 2001).

[49] S. G. Liu, Y. Q. Liu, Y. Xu, D. B. Zhu, A. C. Yu, X. S. Zhao, *Langmuir* **14**, 690 (1998).

[50] M. J. Cohen, A. J. Heeger, *Physical Revew B* **16**, 688 (1977).

[51] A. S. Dhindsa, M. R. Bryce, H. Ancelin, M. C. Petty, J. Yarwood, *Langmuir* **6**, 1680 (1990).

[52] C. L. Donley, R. Zangmeister, W. Xia, B. Minch, A. Drager, S. K. Cherian, L. LaRussa, B. Kippelen, B. Domercq, D. L. Mathine, D. F. O ’Brien, N. R. Armstrong, *Journal of Materials Research* **19**, 2087 (2004).

[53] D. Manno, R. Rella, L. Troisi, L. Valli **280**, 249 (1996).

[54] P. E. Smolenyak, E. J. Osburn, S.-Y. Chen, L.-K. Chau, D. F. O’Brien, N. R. Armstrong, *Langmuir* **13**, 6568 (1997).

[55] K. Iriyama, *LB* 膜の分子デザイン (共立出版, 1988).

[56] S. Palacin, *Advances in colloid and interface science* **87**, 165 (2000).

[57] Y. Matsuzawa, T. Seki, K. Ichimura, *Thin Solid Films* **301**, 162 (1997).

[58] S. Fouriaux, F. Armand, O. Araspin, A. Ruaudel-Teixier, E. M. Maya, P. Vazquez, T. Torres, *J. Phys. Chem.* **100**, 16984 (1996).

[59] T. Takeuchi, 吸着の化学 (産業図書, 1995).

[60] Z. Li, M. Lieberman, W. Hill, *Langmuir* **17**, 4887 (2001).

[61] I. Carmeli, G. Leitus, R. Naaman, S. Reich, Z. Vager, *Journal of Chemical Physics* **118**, 10372 (2003).

[62] C. Messerschmidt, D. K. Schwartz, *Langmuir* **17**, 462 (2001).

[63] C. E. Taylor, D. K. Schwartz, *Langmuir* **19**, 2665 (2003).

[64] M. S. Lim, K. Feng, X. Chen, N. Wu, A. Raman, J. Nightingale, E. S. Gawalt, D. Korakakis, L. A. Hornak, A. T. Timperman, *Langmuir* **23**, 2444 (2007).

[65] J. Israelachvili, T. J. Mccarthy, R. Murray, R. F. Pease, J. F. Rabolt, K. J. Wynne, H. Yu, *Langmuir* **68**, 932 (1987).

[66] H. Ma, O. Acton, D. O. Hutchins, N. Cernetic, A. K.-Y. Jen, *Physical Chemistry Chemical Physics* **14**, 14110 (2012).

[67] D. O. Hutchins, O. Acton, T. Weidner, N. Cernetic, J. E. Baio, G. Ting, D. G. Castner, H. Ma, A. K. Y. Jen, *Organic Electronics: physics, materials, applications* **13**, 464 (2012).

[68] D. Zacher, R. Schmid, C. Wöll, R. A. Fischer, *Angewandte Chemie - International Edition* **50**, 176 (2011).

[69] H.-L. Yip, S. K. Hau, N. S. Baek, H. Ma, A. K.-Y. Jen, *Advanced Materials* **20**, 2376 (2008).

[70] S. Wang, Y. Liu, X. Huang, G. Yu, D. Zhu, *Journal of Physical Chemistry B* **107**, 12639 (2003).

[71] H. Yamada, H. Imahori, Y. Nishimura, I. Yamazaki, T. K. Ahn, S. K. Kim, D. Kim, S. Fukuzumi, *Journal of the American Chemical Society* **125**, 9129 (2003).

[72] M. S. Boeckl, A. L. Bramblett, K. D. Hauch, T. Sasaki, B. D. Ratner, J. W. Rogers, *Langmuir* **16**, 5644 (2000).

[73] S. Yoshimoto, *Bulletin of the Chemical Society of Japan* **79**, 1167 (2006).

[74] P. Zubko, S. Gariglio, M. Gabay, P. Ghosez, J.-M. Triscone, *Annual Review of Condensed Matter Physics* **2**, 141 (2011).

[75] F. Roth, M. Huth, *Journal of Physics D: Applied Physics* **44**, 375102 (2011).

[76] H.-L. Lu, Z.-M. Liao, L. Zhang, W.-T. Yuan, Y. Wang, X.-M. Ma, D.-P. Yu, *Scientific reports* **3**, 2870 (2013).

[77] C. H. Cheng, J. Wang, G. T. Du, S. H. Shi, Z. J. Du, Z. Q. Fan, J. M. Bian, M. S. Wang, *Applied Physics Letters* **97**, 1 (2010).

[78] K. B. Blodgett, *Journal of the American Chemical Society* **57**, 1007 (1935).

[79] K. Hukui, 第５版 実験化学講座 *24* 表面・界面 (丸善株式会社, 2007), chap. 3.15 原子間力顕微鏡 (AFM), pp. 301–319.

[80] Hitachi High-Tech Science Corporation, http://www.hitachi-hightech.com/hhs/products/tech/em/spm/principle/b_3_dfm.html/.

[81] Hitachi High-Tech Science Corporation, http://www.hitachi-hightech.com/hhs/products/tech/em/spm/mode/12_activeQ.html/.

[82] B. Cappella, G. Dietler, *Surface Science Reports* **34**, 1 (1999).

[83] T. Kitamori, K. Miyamura, 分析化学 *II* (丸善株式会社, 2002).

[84] M. D. Elking, G. He, Z. Xu, *The Journal of Chemical Physics* **105**, 6565 (1996).

[85] E. D. Palik, *Handbook of optical constants of solids* (Academic Press, 1985).

[86] M. Yasaka, リガクジャーナル **40**, 1 (2009).

[87] H. Hujisawa, 第５版 実験化学講座 *24* 表面・界面 (丸善株式会社, 2007), chap. 3.2 光電子分光, pp. 106–120.

[88] I. K. Robinson, *Physical Review B* **33**, 3830 (1986).

[89] E. Vlieg. A concise rod manual (2001), http://www.esrf.eu/computing/scientific/joint_projects/ANA-ROD/binaries/rodmanual.pdf.

[90] R. Francis, S. Moss, A. Jacobson, *Physical Review B* **64**, 1 (2001).

[91] H. Morisaki, T. Koretsune, C. Hotta, J. Takeya, T. Kimura, Y. Wakabayashi, *Nature Communications* **5**, 5400 (2014).

[92] S. Ten-no, 第５版 実験化学講座 *12* 計算化学 (丸善株式会社, 2004), chap. 1.2 分子軌道計算の基礎, pp. 2–15.

[93] S. Hirata, 第５版 実験化学講座 *12* 計算化学 (丸善株式会社, 2004), chap. 1.5 密度汎関数法, pp. 34–48.

[94] P. Hohenberg, W. Kohn, *Physical Review* **136**, B864 (1964).

[95] W. Kohn, L. J. Sham, *Physical Review B* **140** (1965).

[96] K. Burke, L. O. Wagner, *International Journal of Quantum Chemistry* **113**, 96 (2013).

[97] G. Kresse, J. Furthmüller, *Physical Review B* **54**, 11169 (1996).

[98] S. Grimme, *Journal of Computational Chemistry* **27**, 1787 (2006).

[99] F. Zhang, J. D. Gale, B. P. Uberuaga, C. R. Stanek, N. a. Marks, *Physical Review B* **88**, 1 (2013).

[100] S. Hati, D. Datta, *The Journal of Physical Chemistry* **99**, 10742 (1995).

[101] J. Souto, J. de Saja, M. Gobernado-Mitre, M. Rodriguez, R. Aroca, *Sensors and Actuators B: Chemical* **16**, 306 (1993).

[102] A. Biadasz, B. Bursa, B. Barszcz, A. Bogucki, B. Laskowska, A. Graja, D. Wróbel, *Dyes and Pigments* **89**, 86 (2011).

[103] Y. L. Emelyanov, V. V. Khatko, A. A. Tomchenko, *Synthetic Metals* **79**, 173 (1996).

[104] T. Minari, M. Seto, T. Nemoto, S. Isoda, K. Tsukagoshi, Y. Aoyagi, *Applied Physics Letters* **91**, 2005 (2007).

[105] H. Jiang, J. Ye, P. Hu, F. Wei, K. Du, N. Wang, T. Ba, S. Feng, C. Kloc, *Scientific reports* **4**, 7573 (2014).

[106] G. A. Schick, I. C. Schreiman, R. W. Wagner, J. S. Lindsey, D. F. Bocian, *J. Am. Chem. Soc.* **111**, 1344 (1989).

[107] Y. Qiu, P. Chen, M. Liu, *Langmuir* **24**, 7200 (2008).

[108] K. Xiao, Y. Q. Liu, X. B. Huang, Y. Xu, G. Yu, D. B. Zhu, *Journal of Physical Chemistry B* **107**, 9226 (2003).

[109] M. Paradinas, L. Garzo´n, F. Sa´nchez, R. Bachelet, D. B. Amabilino, J. Fontcuberta, C. Ocal, *Physical Chemistry Chemical Physics* **12**, 4273 (2010).

[110] A. Ohtomo, H. Y. Hwang, *Nature* **427**, 423 (2004).

[111] Z. Xu, S. Lau, P. W. Bohn, *Surface Science* **296**, 57 (1993).

[112] M. A. Firestone, M. L. Shank, S. G. Sligar, P. W. Bohn, *Journal of the American Chemical Society* **118**, 9033 (1996).

[113] C. H. Lanier, J. M. Rondinelli, B. Deng, R. Kilaas, K. R. Poeppelmeier, L. D. Marks, *Physical Review Letters* **98**, 98 (2007).

[114] R. Gunnarsson, A. S. Kalabukhov, D. Winkler, *Surface Science* **603**, 151 (2009).

[115] T. Bucko, J. Hafner, S. Lebegue, J. G. Angyan, *J. Phys. Chem. A* **114**, 11814 (2010).

[116] Y. Zhang, S. Du, H.-J. Gao, *Physical Review B* **84**, 1 (2011).

[117] G. Mattioli, F. Filippone, P. Alippi, P. Giannozzi, A. A. Bonapasta, *J. Mater. Chem.* **22**, 440 (2012).

[118] S. Javaid, S. Lebègue, B. Detlefs, F. Ibrahim, F. Djeghloul, M. Bowen, S. Boukari, T. Miyamachi, J. Arabski, D. Spor, J. Zegenhagen, W. Wulfhekel, W. Weber, E. Beaurepaire, M. Alouani, *Physical Review B* **87**, 1 (2013).

[119] Code: Bader charge analysis. Henkelman Group, http://theory.cm.utexas.edu/henkelman/code/bader/.

[120] C. Ocal, R. Bachelet, L. Garzón, M. Stengel, F. Sánchez, J. Fontcuberta, *Chemistry of Materials* **24**, 4177 (2012).